ABSTRACT

Title of dissertation: EFFECT OF ELECTROSTATIC INTERACTIONS ON BIOMOLECULAR SELF-ASSEMBLY PROCESSES

Hongcheng Xu
Doctor of Philosophy, 2018

Dissertation directed by: Dr. Silvina Matysiak, Associate Professor
Fischell Department of Bioengineering
Biophysics Program

Molecular level self-assembly processes are not only ubiquitous in living cells, but also widely applied in industry to synthesize and fabricate a variety of nanoscale biomaterials. The emergence of ordered aggregates from disordered components typically requires driving forces from electrostatic interactions to hydrophobic-hydrophilic effects. This thesis aims to elucidate the effect of electrostatic interactions, and the intricate balance between electrostatic and hydrophobic interactions in dictating spontaneous self-assembly processes with three case studies covering various types of biomolecules.

For the first case study, we have examined the pH-induced polysaccharide hydrogel network formation. The polysaccharide molecule chitosan forms hydrogels composed of water-filled cross-linking polymer chains. The pH-responsive self-assembly behavior of chitosan hydrogel has been utilized in fabricating nanomaterials with a wide range of applications. To investigate the role of electrostatic

interactions in the chitosan hydrogel network formation, we have developed a novel coarse-grained (CG) chitosan polymer model that captures the pH-dependent self-assembly behavior. The structural, mechanical, and thermodynamical properties of chitosan polymer hydrogel have been characterized well in the simulations and agree very well with experimental observations.

For the second case study, the anticancer peptide folding induced by phospholipid membrane was investigated. Peptide folding in an aqueous environment is a self-assembly process that has been well studied over the years. However, the folding in a membranous environment is complicated by the heterogeneity in phospholipid distributions and membrane-peptide interactions. To provide information about the driving forces behind membrane peptide folding and the effect of lipid composition on folding behavior, my work has combined our recently developed Water-Explicit Polarizable Protein (WEPPRO) and Membrane (WEPMEM) model to explore the driving forces behind model anticancer peptide SVS-1 folding and how they can be affected by changing the membrane composition.

For the third case study, we have studied the formation of nanodomains in mixed lipid bilayers. Phospholipid membranes are essential components in animal cells. The heterogeneous distribution of phospholipids on the membrane bilayer plays an important role in cellular structure and function such as signal transduction and membrane fusion. Interactions between a mixture of lipids and different ligands give rise to interesting patterns that are yet to be understood. Model lipid bilayers with a content of anionic lipids have been shown experimentally to be sensitive to the presence of certain ions. Monovalent cation Li^+ induces membrane phase transition

similarly as Ca^{2+} and Mg^{2+}, while distinctive from other monovalent cations like Na^{+} and K^{+}. We have evaluated the role of electrostatics interactions in the size-dependent cation-induced lipid nanodomain formation with binary mixed bilayers composed of zwitterionic and anionic lipids.

EFFECT OF ELECTROSTATIC INTERACTIONS ON BIOMOLECULAR SELF-ASSEMBLY PROCESSES

by

Hongcheng Xu

Dissertation submitted to the Faculty of the Graduate School of the
University of Maryland, College Park in partial fulfillment
of the requirements for the degree of
Doctor of Philosophy
2018

Advisory Committee:
Dr. Silvina Matysiak, Chair/Advisor
Dr. Jeffery Klauda
Dr. Christopher Jarzynski
Dr. Gregory Payne
Dr. Pratyush Tiwary

Acknowledgments

This work would not have been possible without the support and guidance from my advisor, Dr. Silvina Matysiak, for she has taught me a great deal in every aspect of research life. She has been an excellent advisor, and I feel very lucky to have worked in her lab in last 5 years.

I am grateful to all those with whom I have had the pleasure to work with in research projects. I would like to thank all the thesis committee members, Dr. Jeffery Klauda, Dr. Pratyush Tiwary, Dr. Gregory Payne, and Dr. Christopher Jarzynski for taking the time to be in my committee. I would especially like to thank Dr. Christopher Jarzynski, and Dr. Gregory Payne for their talented insight on theory and experiment, from which I learnt a great deal on what are the means and ends of computational simulations.

Also, I would like to thank my fellow labmates, who have provided me with insightful discussion and continuous support over the years: Abhilash Sahoo, Greg Custer, Sai Ganesan, Riya Samanta, Christopher Look and many others. They have made graduate school enjoyable and provided countless insights and discussions on my projects.

Last but not the least, I would also like to thank my family and friends. It is a tough process to study and do research thousands of miles from my home. However, their continuous help and couragement have kept all the worries from me throughout the years.

Table of Contents

List of Tables

List of Figures

List of Abbreviations

MD	Molecular Dynamics
CG	Coarse Graining
FF	Force Field
NPT	Isothermal-Isobaric Ensemble
NVT	Canonical Ensemble
PMF	Potential Mean Force
WEPPROM	Water Explicit Polarizable PROtein Model
WEPMEM	Water Explicit Polarizable MEmbrane Model
H–bond	Hydrogen Bond
BB	Backbone
H	Hydrophobic CG Residue
P	Polar CG Residue
N	Neutral CG Residue
Q+	Positively Charged CG Residue
Q-	Negatively Charged CG Residue
LJ	Lennard-Jones Interactions
POPS	1-palmitoyl-2-oleoyl-*sn*-glycero-3-phospho-L-serine
POPC	1-palmitoyl-2-oleoyl-glycero-3-phosphocholine
ϵ	LJ strength
σ	Bead Size
μ	Dipole Moment
q	Charge
M_+	Monovalent Ion
Fr_{sheet}	Sheet Fraction
L_c	Peptide end to end distance

Chapter 1: Introduction

1.1 Objective

This thesis is focused on exploring how electrostatic interactions dictate the thermodynamics and kinetics of biomolecular self-assembly processes. Self-assembly is the process of the spontaneous formation of organized structure starting from disordered components driven by specific interactions. Molecular self-assembly processes are ubiquitous in biological systems. One of the most common self-assembly processes *in vivo* is the formation of ordered lipid nanodomains that are related to the "lipid raft" hypothesis in the cellular membrane [2–11]. Cellular membranes are not homogeneous in nature and are composed of various lipids and peptides. Ordered nanodomains can be induced through a multitude of interactions through ions, peptides, and cholesterol. In addition, biomolecular self-assembly processes are important *in vitro* with a wide range of applications. For example, a naturally-derived biomolecular polymer, chitosan, forms a hydrogel that can be used as an oil dispersant additive [12,13], to create artificial skins [14,15], and in biochip manufacturing [16] through self-assembly. For the above-mentioned self-assembly processes, electrostatic interactions in the form of hydrogen bonding and ion bridging are of the most critical driving forces. However, due to the microscopic nature of

biomolecular systems, it is still challenging to characterize at the molecular level the impact of changing electrostatic interactions in self-assembly processes with wet-lab experiments. Alternatively, computer simulations are increasingly popular nowadays because it captures the molecular interactions of biomolecular systems from a microscopic perspective, and improves the understanding of underlying molecular mechanisms behind biomolecular self-assembly processes. By utilizing molecular dynamics (MD) simulations, we were able to investigate quantitatively the effect of electrostatic interactions in influencing the free energy landscape and the dynamic pathways of different biomolecular self-assembly processes.

All-atom molecular dynamics (MD) simulations explicitly solve the velocities and positions of the atoms by integrating Newton's second law of motion, but often require a considerate amount of computational cost. Due to the enormous amount of atoms involved in most biomolecular self-assembly systems and the limitation in computational resources, it is usually not feasible to explore the whole landscape of self-assembly pathways in a biologically-relevant timescale for large systems. Consequently, coarse-grained (CG) models have been developed to reduce the computational cost significantly by treating multiple atoms as one group or bead, while keeping the topology of systems the same as atomistic models. CG models also smooth the free energy landscape of the self-assembly process, which allows better sampling of major molecular conformations. With CG models in MD simulations, explorations of molecular self-assembly processes in a broader time- and length-scale are possible.

The electrostatics interactions are not well approximated in many CG models.

Usually, only a single point charge is assigned to each CG bead to approximate the net charge of the corresponding group of atoms [17, 18]. If the net charge is zero for several atoms with partial charges, the electrostatic interactions will be treated as zero once they are coarse-grained into one bead. This significantly underestimates the polarization ability of molecules and makes it difficult to model interactions like hydrogen bonding. Even though there are models attempting to compensate the lack of electric polarization by incorporating point dipoles [19], the dipole moment is fixed and can hardly model the effect of induced polarization in the simulation. Nevertheless, electrostatic interactions, particularly hydrogen bonding or dipole-dipole interactions, are one of the main driving forces of many biomolecular self-assembly processes [20]. However, it remains an open question how the presence of electrostatic interactions affects nano-structure and molecular dynamics of many biomolecular self-assembly processes. Therefore, it is crucial to explore the role of electrostatic interactions in various self-assembly processes, and develop CG models for biomolecules that are able to characterize well electrostatic interactions, especially the dipole-dipole interactions.

Electrostatic interactions play a critical role in pH-dependent self-assembly of chitosan hydrogel network formation. It is an important *in vitro* self-assembly process that has a wide variety of applications in biofabrication of chitosan-based interfaces [21–25]. Chitosan is one of the most abundant polysaccharides in nature. It is a linear copolymer composed of β_{14} linked N-acetylglucosamine (GLcAc) units and glucosamine (GLcN) units. Recent experimental work has shown that chitosan hydrogel morphology and mechanical properties are closely connected to local pH

gradient and salt concentration [26]. However, there is still a lack of understanding regarding the mechanism of chitosan hydrogel formation and how solution conditions such as local pH and polymer concentration affect its self-assembly behavior. Molecular simulations have provided an effective way to understand the relationship between molecular interactions and macroscopic functional properties of materials [27,28]. Previous atomistic molecular dynamics (MD) work has yielded trajectories of molecular level chitosan structures in a timescale of nanoseconds [29, 30]. Early events in the self-assembly process of chitosan chains have also been studied atomistically by Morrow *et al.* [31]. However, these studies focused on few chitosan chains with a small number of monomers, mostly due to limitations of computational expenses in all-atom simulations. On the other hand, coarse-grained (CG) models allow for the characterization of larger systems over longer time scales than atomistic models. Recently, Hall and coworkers have developed a CG model of chitosan with implicit solvent [32, 33]. With this CG model, these authors were able to explore how the degree of acetylation and chitosan monomer sequence affect self-assembly behavior and porosity of chitosan networks. Nevertheless, since this model renormalizes water degrees of freedom into the definition of pairwise interaction potentials between chitosan CG beads, it does not model the solution medium dielectric properties. We have developed a water-explicit CG model of chitosan to explore the formation of chitosan networks at different pH and polymer concentrations. With this model, we are able to characterize the mechanism of chitosan gel formation by deacetylated chains and make a connection between molecular reorganization of chitosan chains with changes in mechanical properties obtained at

different pH conditions.

Another application of electrostatics-driven self-assembly process is the folding of membrane peptide on biological membrane surfaces. Membrane peptide folding is a unique self-assembly process different from its folding in aqueous environment. Membrane peptides usually undergo conformational transitions from the water-soluble state to the membrane-associated state before they perform their cellular functions [34, 35]. Antimicrobial peptides (AMPs) are a group of short peptides that can be used as models to study the energetics of interfacial folding [36, 37]. Similar to the antimicrobial mechanism of AMPs, an anticancer peptide (ACP) SVS-1 (KVKVKVKVDPLPTKVKVKVKNH2) was designed to target tumor cells instead of microbials. The SVS-1 peptide is intrinsically disordered in aqueous environment, and folds into a functional structure upon partitioning into membrane interface [38]. It is known to fold into β-sheet conformation when interacting with negatively charged vesicles [38]. The formation of secondary structure and intermolecular hydrogen bonds within SVS-1 peptides were proposed to reduce the energetic cost for partitioning into the membrane [20]. Also, the fractions of anionic lipids were found to play an important role in the folding of other peptides such as magainins on membrane surfaces [39, 40]. It is yet to be understood how the balance between water-soluble and membrane-associated states of these peptides affect their partitioning and folding into a membrane environment. Therefore, with the coarse-grained membrane and peptide model that capture well electrostatic interactions, we investigated the effect of lipid bilayer composition and membrane-peptide interactions on the folding of SVS-1 peptide on membrane surfaces.

The effect of ions in inducing lipid nanodomain formation also involves the self-assembly of phospholipids driven by electrostatic interactions. In the "lipid raft" hypothesis [2–11], certain regions of a plasma membrane are considered "denser" than other regions, and play a functional role in cellular signal transduction [2,4,7] and endocytosis [41]. Some nanodomains on lipid membranes can be formed through the aggregation of lipids [42,43], and they have been studied over the years. However, the specific interactions and the mechanisms of their formation are yet to be understood. The role of metal ions is vital in inducing similarly structured nanodomains. Ions affect the membrane structure, dynamics, and stability by interacting with polar lipid headgroups. Among monovalent metal ions (K^+, Na^+, Li^+), both K^+ and Na^+ only induce minor changes in bilayer structure in experiments [44]. However, Li^+ has an evident effect on the phase transition of a lipid bilayer by increasing the melting temperature of phosphatidylserine (PS) lipid [44–47]. Also, Li^+ is known to induce the formation of dehydrated ion-PS complexes and bind to the phosphate and carboxylate groups of dimyristoylphosphatidylserine (DMPS) lipid [48]. The distinction of Li^+ from other monovalent cations and its resemblance of Ca^+ in binding to anionic lipid bilayers draws wide attention among biochemists. It has been hypothesized that the binding modes and burial depth [49] of Li^+ and Ca^{2+} share similarities which might be a contributing factor for their similar effects on bilayers. For K^+ and Na^+, there exist discrepancies based on MD force fields upon their binding modes and affinities with lipids [50–54]. Therefore, the question remains how monovalent ion Li^+ plays a role in lipid bilayer phase transition, and how its interactions affect self-assembly dynamics and the formation of lipid domains.

This thesis investigates three case studies of self-assembly processes with different biomolecules. These processes are the phospholipid domain formation, membrane peptide folding, and the polysaccharide hydrogel network formation. The objective of this work is threefold:

To utilize the CG model for polysaccharide chitosan that characterizes the pH-dependent hydrogel network formation, and study the structural, mechanical, and thermodynamical properties of the self-assembled network

To explore how membrane dielectric environment and membrane-peptide interactions regulate the hairpin formation of model anticancer peptide SVS-1

To gain a better understanding of the electrostatic interactions in lipid bilayers, and the role of monovalent cation sizes in inducing lipid nanodomain formation in mixed lipid membranes

1.2 Outline of Thesis

In Chap. 2, we have constructed a pH-dependent self-assembly hydrogel network of chitosan polymers using a water-explicit CG model. With this model, we have discovered the role of physical crosslinking pattern on chitosan hydrogel mechanical properties. When the pH or the polymer concentrations in chitosan systems

increase, the elastic modulus also increases. Three states of crosslinking chains were identified corresponding to the states of stable parallel crosslink, on-pathway parallel crosslink, and perpendicular crosslink. The dominant crosslinking pattern in low polymer concentration was the parallel crosslinking, while the dominant crosslinking in high polymer concentration was the perpendicular crosslinking. The parallel crosslinking plays an important role in maintaining the high mechanical strength of the polymer hydrogel.

In Chap. 3, we proposed a coarse-grained water-explicit polarizable protein (WEPPRO) model that can be used to study the spontaneous formation of secondary structure without external bias. We also formulated a coarse-grained water-explicit polarizable membrane (WEPMEM) model that captures the dielectric gradient in membrane-water interfacial region. The anticancer peptide SVS-1 folding on the membrane surface was studied with the combination of both models. We have discovered the role of electrostatic interactions on model anticancer peptide SVS-1 hairpin formation. It was found that the presence of polarizability in CG particles gave rise to the formation of SVS-1 hairpin structure. Moreover, we found that the subtle balance between intra-peptide interaction and peptide-lipid bilayer interaction was key to induce the folding of hairpin conformation for SVS-1 peptide on a membrane surface.

In Chap. 4, we utilized the WEPMEM model and investigate the effect of monovalent cation sizes on lipid nanodomain formation. A window of coarse-grained monovalent cations sizes was observed to induce evident nanodomain formation on mixed zwitterionic/anionic membranes. The aggregation of anionic lipids was

bridged by cationic monovalent ions, which precipitated the membrane curvature. In addition, we found that the nanodomain formation was much less evident when the sizes of monovalent cations were too small or too large. There are two factors that contribute to the distinction between cations with different sizes: the partitioning of ions into the membrane, and the binding modes between ions and lipid headgroups. The observations from the simulation are reminiscent of the experimental findings that only monovalent cation Li^+ has a distinctive effect in inducing mixed lipid bilayer phase separation, while other monovalent cations such as Na^+ and K^+ do not have such effect.

Chapter 2: Effect of pH on Chitosan Hydrogel Polymer Network Structure

2.1 Overview

This chapter is based on the author's publication: Effect of pH on Chitosan Hydrogel Polymer Network Structure. Hongcheng Xu and Silvina Matysiak. Chemical Communication, 2017.

Chitosan is a molecule that can form water-filled 3D polymer networks with a wide range of applications. A new coarse-grained model for chitosan hydrogel was developed to explore its pH-dependent self-assembly behavior and mechanical properties. Our results indicate that the underlying polymer physical crosslinking pattern induced by solution pH have a significant effect on hydrogel elastic moduli. With this model, we obtain pH-dependent structural and mechanical property changes in agreement with experimental observations, and provide a molecular mechanism behind the changes in polymer crosslinking patterns.

2.2 Introduction

Chitosan is one of the most abundant polysaccharides in nature. It is a linear copolymer composed of β_{1-4} linked N-acetylglucosamine (GLcAc) units and glucosamine (GLcN) units. It is produced from exoskeleton of crustacean and mollusks. The deacetylated unit GLcN is shown in Figure 2.1. Due to the primary amine of GlcN, chitosan polymer is transformed in cationic polyelectrolyte at low pH when these amines are protonated, and forms insoluble hydrogel with deprotonated amines at high pH. This pH-responsiveness of chitosan self-assembly behavior is a critical property utilized in biofabrication of chitosan-based interfaces [21–25]. Also, chitosan is regarded as a green biomaterial and has been increasingly used for its biodegradable and biocompatible properties [55]. Extensive studies have been performed on chitosan-based applications such as drug delivery, gene therapy, wound healing and tissue engineering [56–59].

Chitosan forms hydrogels composed of water-filled cross-linking polymer chains. The linear backbone of chitosan molecules provides many interaction sites for nanoscale components to bind to, thus it is used as bio-friendly matrix [60] to immobilize biological molecules while preserving the bioactivity of these molecules. The advantage of using chitosan over other materials as the scaffold material in biological systems is due to its biodegradability, biocompatibility and non-toxicity [61], and chitosan-based polysaccharide hydrogels have been widely used as excellent tissue engineering biomaterials [59, 62–65].

The physical and chemical properties of the chitosan molecule and its analogs

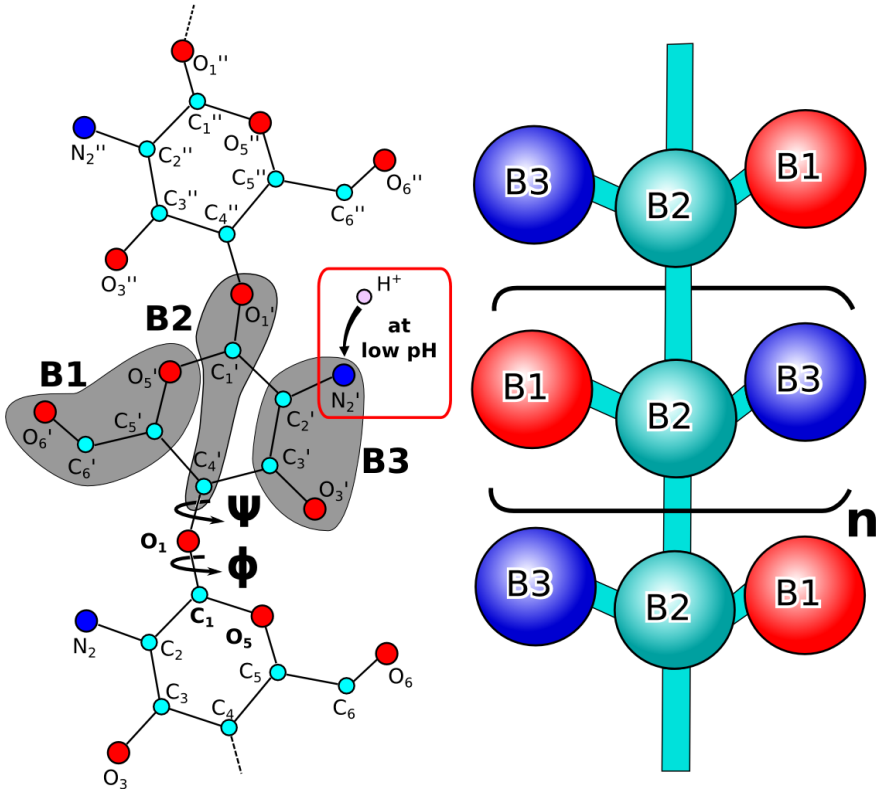

Figure 2.1: (a) CG mapping scheme of deacetylated chitosan molecule with three glucosamine (GLcN) units. Shaded areas mark atoms grouped into a single CG bead. Two dihedral angles (ψ, ϕ) are defined as intersecting planar angles formed by atoms O5-C1-O1-C4' and C1-O1-C4'-C3'. Red box indicates protonation site in an amine group. (b) Schematic representation of CG chitosan molecule.

have been studied extensively in experiments [66]. The radius of gyration of chitosan is reported to be between 10nm to 100 nm [67]. With a persistence length between 5-15 nm [68–71] the chitosan molecule behaves as a stiff worm-like chain. The residual bound water weight percentage in chitosan structure is represented by the degree of hydration, and the percentage of chitosan units which the amino group gets protonated is depicted as degree of protonation. These properties have an effect on

the conformational flexibility of chitosan molecules, as indicated by chitosan polymer crystal structure studies [72–76]. A number of conformers are observed in chitosan polymer crystal structures, of which type I structure is the one retained in most of chitosan-metal complex crystals [75]. Other 3 helical conformations, have also been reported by Ogawa et al. [72, 73, 76]. The conformational flexibility of chitosan is crucial in understanding its function in living organisms. In addition, the mechanical properties of chitosan hydrogel vary significantly depending on its degree of swelling (typically between 80%-95%), protonation as well as the copolymerization with other crosslinkers [77–80].

One of the most important properties of the chitosan hydrogel is the pH-responsive nano-scale self-assembly behavior [26, 67]. Chitosan is soluble in near-neutral acid solutions, and the solubility of chitosan is largely dependent on the polymer chain degree of protonation, which is directly affected by the solvent pH [81]. The pH-dependent self-assembly behavior is the critical property exploited in biofabrication of chitosan-based surfaces. The chitosan-based surfaces are widely used in devices such as biosensors, microarrays and microelectromechanical systems (MEMS) [21, 24, 25, 82]. By exploiting the pH-responsive self-assembly property, chitosan chains can be electrodeposited on the surface by applying an electric field to the chitosan solution [21]. The number of protons near the surface of a cathode is reduced by the applied voltage, leading to a localized pH gradient, and the chitosan molecules are deposited in the localized high-pH region near the cathode to form a controlled nano-scale structure [21]. This method allows programmable tuning of the chitosan deposition [25] through controlled electric field. The electrodeposited

thin films have a great potential in fabricating systems that integrate biology into devices [23].

Recent experimental work has shown that chitosan hydrogel morphology and mechanical properties are tightly connected to local pH gradient [26]. However, there is still a lack of understanding regarding the mechanism of chitosan hydrogel formation and how solution conditions such as local pH and polymer concentration affect its self-assembly behavior. Microscopic level of accurate computational modeling has been an effective way to understand the relation between molecular interactions and macroscopic functional properties [27, 28]. Recent molecular dynamics simulation work has yielded nano-seconds trajectories of atomic-level chitosan structures [29, 30]. MD studies suggest that intramolecular hydrogen bonds between chitosan molecules are affected by adjacent water molecule orientation [30], and it is also demonstrated that the electrostatic contribution to the solvation free energy of chitosan chains is dominant [29, 30, 83]. Atomistic MD simulations have also been conducted to study the self-assembly process of chitosan chains. Morrow *et al.* have simulated the early events in the self-assembly process of chitosan [31], and reveal the subtle balance between attractive and repulsive forces that is essential in the pH-dependent network phase transition. Liu *et al.* have characterized the free energy landscape of the wrapping process of a single chitosan chain and found two energetically favorable helical conformations [84].

Although constructive observations are made from all-atom MD simulations of chitosan molecules, the significant computational cost for the atomistic simulation limits the time and length scales of the system that can be investigated. On the other

hand, coarse-grained molecular models considerably reduces the computational cost by grouping several atoms into one bead, allowing the molecular processes of longer time scale and broader length scale to be investigated. Recently, Hall and coworkers have developed a CG model of chitosan with implicit solvent [32, 33]. With this CG model, these authors were able to explore how the degree of acetylation and chitosan monomer sequence affect self-assembly behavior and porosity of chitosan networks. Nevertheless, since this model renormalizes water degrees of freedom into the definition of pairwise interaction potentials between chitosan CG beads, it does not model the solution medium dielectric properties. Also, some state-of-the-art coarse-grained models for carbohydrates simulation have been proposed, such as the extension of MARTINI force field to carbohydrates [85]. A novel coarse-grained model of chitosan is needed to address the molecular details of the chitosan self-assembly behaviors. Meanwhile, many other polysaccharide molecules of similar structures to the chitosan molecule have already been characterized by CG models [86, 87] . Therefore, it is now technically viable and necessary to develop the CG model of the chitosan molecule.

In this chapter, we report a water-explicit CG model of chitosan to explore the formation of chitosan networks at different pH and polymer concentrations. The goal of this study is to characterize the mechanism of chitosan gel formation by chitosan chains and make a connection between molecular reorganization of chitosan chains with changes in mechanical properties obtained at different pH conditions. Although we are using a salt-free condition (only with counterions if needed) in simulations. The model has the potential to enable the exploration on how ionic

screening might affect the chitosan network formation. Simulations in this study were performed using the GROMACS and LAMMPS simulation packages [88, 89] with the MARTINI polarizable water model [90]. CG mapping scheme of the model is illustrated in Figure 2.1. The pH was modeled in the simulations by altering the degree of protonation of the chitosan chains according to the Henderson-Hasselbalch equation. For example, 50% of the chitosan B3 beads should be protonated at pH 6.5, and this was achieved by randomly protonating 50% of all B3 beads in the system (as opposed to 50% of the B3 beads on each chain). All self-assembly simulations start with a random distribution of chitosan polymers. Parametrization was done by matching bonded interaction distributions from atomistic simulations.

2.3 Methods

2.3.1 CG Model

In our mapping scheme, we approximately group 4 heavy atoms into a single coarse-grained bead. As shown in Figure 2.1, the B1 bead includes atoms from the hydroxyl side chain, the B2 bead includes most of the polymer backbone atoms, and the B3 bead maps the hydroxyl and amino groups opposite to the B1 side chain. All three beads have different levels of hydrophilicity, and the B3 bead can become protonated depending on the pH. The basic bead type used in our chitosan model is taken from the MARTINI carbohydrates coarse-grained force field parameter set [85], in which each building block is categorized as apolar, polar or charged. The polarity types of B1, B2 and B3 beads are in increasing order, and

B3 bead becomes positively charged in an acidic environment. The polarity is determined by comparing to oligosaccharides examples provided in the MARTINI CG model for carbohydrates [85]. Each chitosan chain is designed to have 10 monomers so that the total length is within the experimentally reported persistence length (5-15nm) [68–71].

$$U_{\text{total}} = U_{\text{bonded}} + U_{\text{non-bonded}}, \tag{2.1a}$$

$$U_{\text{bonded}} = U_{\text{bonds}} + U_{\text{angles}} + U_{\text{dihedrals}}, \tag{2.1b}$$

$$U_{\text{non-bonded}} = U_{\text{vdW}} + U_{\text{electrostatics}}, \tag{2.1c}$$

$$U_{\text{bonds}} = \sum_{bonds} \frac{1}{2} k_l (l - l_0)^2, \tag{2.1d}$$

$$U_{\text{angles}} = \sum_{angles} \frac{1}{2} k_\theta (\theta - \theta_0)^2, \tag{2.1e}$$

$$U_{\text{dihedral}} = \sum_{dihedrals} k_\phi (1 + \cos(n\phi - \phi_0)), \tag{2.1f}$$

$$U_{\text{vdW}} = \sum_{pairs(i \neq j)} 4\epsilon_{ij} \left[\left(\frac{\sigma}{r} \right)^{12} - \left(\frac{\sigma}{r} \right)^{6} \right], \tag{2.1g}$$

$$U_{\text{electrostatics}} = \sum_{pairs(i \neq j)} \frac{q_{\text{i}} q_{\text{j}}}{4\pi\epsilon_0 \epsilon_{\text{r}} r}, \tag{2.1h}$$

The force field (see Eq. 2.1) consists of bonded interactions (harmonic bonded, angular potential and proper dihedral, see Table 2.1) and non-bonded interactions (12-6 Lennard-Jones potential and Coulombic potential, see Table 2.2). The bonded interaction parameters are tuned from fitting the distributions of corresponding bonds, angles and dihedrals to atomistic simulation results using GRO-

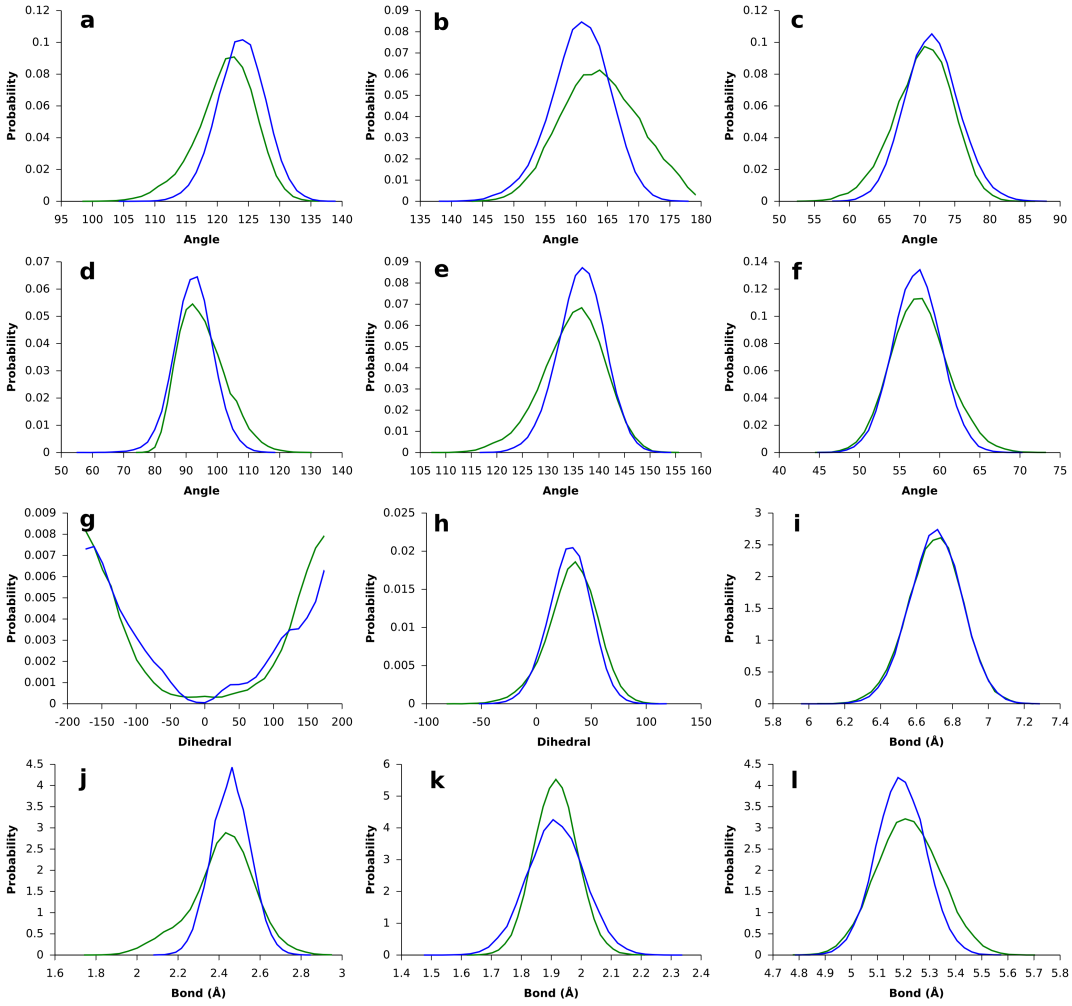

Figure 2.2: Bond and angle distribution comparison in atomistic (green) and CG simulations (blue). (a) B1-B2-B3 angle; (b) backbone angle formed by 3 consecutive backbone B2 beads (B2-B2'-B2"); (c) B2-B2'-B1' angle; (d) B1-B2-B2' angle; (e) B3-B2-B2' angle; (f) B2-B2'-B3' angle; (g) backbone dihedral angle formed by 4 consecutive backbone B2 beads (B2-B2'-B2"-B2"'); (h) B3-B2-B2'-B1' dihedral angle; (i) B3-B2' bond; (j) B1-B2 bond; (k) B2-B3 bond; (l) B2-B2' bond.

MOS 53A6GLYC force field [91]. CG bond and angle distributions match well with corresponding distributions in atomistic simulation as shown in Figure 2.2. Non-

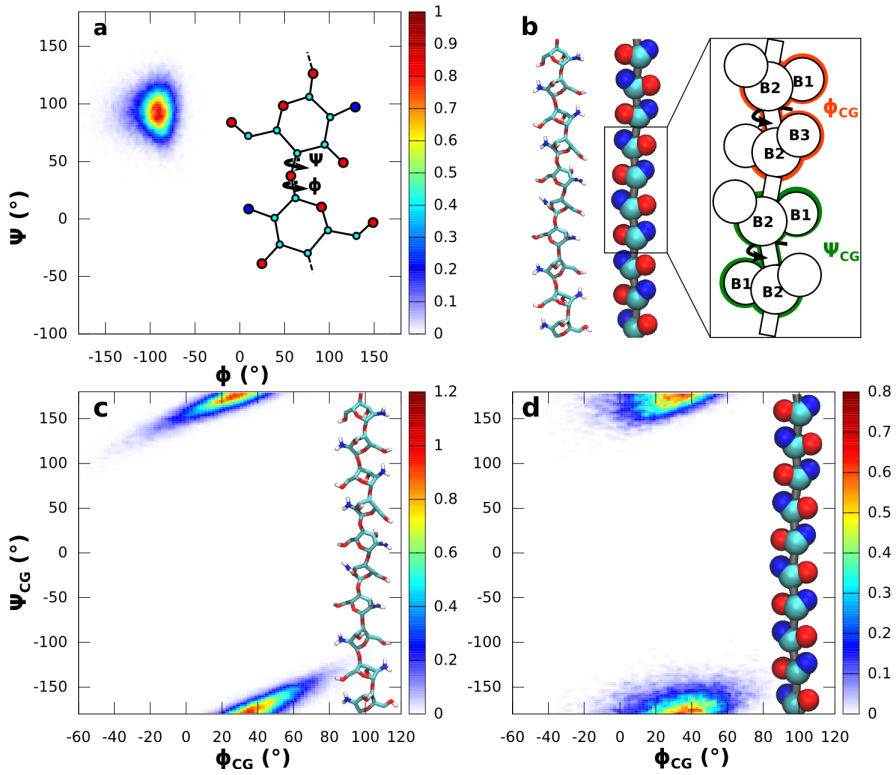

Figure 2.3: Extended 2-fold helix conformation of chitosan chains in atomistic and CG models. (a) ϕ and ψ torsional angle distribution map of a chitosan chain in atomistic simulation; (b) Chitosan chains with extended 2-fold helical conformations in atomistic model (left) and CG model (center). Chitosan CG model is zoomed in to show definitions of CG torsional angles ϕ_{CG} and ψ_{CG}; ϕ_{CG} is defined as the torsional angle formed by B1, B2 beads in one monomer and B2, B1 beads in the subsequent monomer, and ψ_{CG} is defined as the torsional angle formed by B3, B2 beads in one monomer and B2, B1 beads in the subsequent monomer; (c) Torsional angle distribution map of chitosan in atomistic model; (d) Torsional angle distribution map of chitosan in CG model.

bonded interactions are defined according to bead type definitions in the MARTINI CG force field (extension to carbohydrates) [85]. The most polar bead, B3, is defined as comparable to a building block of acetamide because of the presence of the amino group in the bead. The less polar B1 and B2 beads are defined as similar polarity as propanol and ethanol. The protonated B3 bead ($B3^+$) is defined similarly to protonated propylamine. In addition, the torsional angles ϕ_{CG}, ψ_{CG} (as defined in Figure 2.3b) distribution map of chitosan chains for atomistic (Figure 2.3c) and CG (Figure 2.3d) models sample similar configurations in both models. The atomistic model samples the 2-fold helical conformation since the values of ψ and ϕ are centered in the ψ and ϕ of 2-fold helix ($\phi \cong -98°$, $\psi \cong 92°$ in Figure 2.3a) [75]. Therefore, the conformation of CG chitosan polymers in the simulation resembles the 2-fold helix most commonly observed experimentally [72–74, 76]. In the atomistic simulation, the scale of the simulation box is limited (see simulation setup). Since the box size is limited for performance, to simulate an infinite chitosan chain, both ends of a single-chained chitosan polymer are connected through the periodic boundary box. With the exclusion 1-2, 1-3, 1-4 non-bonded interactions, the proper dihedrals are used to reproduce the secondary structure in the atomistic chitosan simulations. The MARTINI polarizable CG water [90] model is used as it is needed to achieve the right behavior of chitosan self-assembly under low pH. The usage of non-polarizable MARTINI CG water results in overbinding of anionic ions to protonated chitosan polymers, leading to chain condensation at low pH.

Table 2.1: Bond, angle and dihedral parameters.

bonds	R_{bond} (nm)	K_{bond} (kJ mol^{-1} nm^{-2})
B1-B2	0.2494	30000
B2-B3	0.1934	30000
B2-B2'	0.5211	30000
angles	$\theta_0(deg)$	K$_{angle}$ (kJ mol^{-1})
B1-B2-B3	123.76	450
B2-B2'-B2"	163.78	350
B2-B2'-B1'	70.94	450
B1-B2-B2'	90.88	100
B3-B2-B2'	135.94	300
B3'-B2'-B2	58.01	800
dihedrals	$\psi_{pd}(deg)$	K$_{pd}$ (kJ mol^{-1})
B1-B2-B2'-B1'	175.62	8
B1-B2-B2'-B3'	-28.59	10
B3-B2-B2'-B1'	36.57	18

Table 2.2: Non-bonded Lennard-Jones (LJ) interaction strengths. Unit of interaction strength (ϵ) is in kJ/mol. The radius (σ) of all LJ interactions is 4.7Å.

Beads	B1	B2	B3	$B3^+/Cl^-$	Water
B1	4.5	4.5	5.6	5.6	4.275
B2	4.5	4.5	5.6	5.6	4.275
B3	5.6	5.6	5.6	5.6	5.32
$B3^+/Cl^-$	5.6	5.6	5.6	3.5	5.0
Water	4.275	4.275	5.32	5.0	4.0

2.3.2 Simulation Parameters and Setup

2.3.2.1 Atomistic simulation

The atomistic simulation was set up with GROMOS53A6 force field [91]. In the simulation, a single 10-mer chitosan polymer chain was connected through the periodic boundary to create an infinite chain. The length of the polymer chain was set to around 5 nm, to capture the minimal persistence lengths reported in experiments [68,69]. In the simulation, 1445 SPC water molecules were used to solvate the chitosan chain. The timestep of atomistic simulation was 1 fs, and the simulation integration method was leapfrog [92]. The total length of the isothermal-isobaric (NPT) simulation was 100 ns, and the last 10 ns was used for analysis. Berendsen temperature and pressure coupling schemes [93] were used with a reference temperature of 300 K, and pressure of 1 atm. The relaxation time of the temperature

coupling was 0.1 ps and of the pressure coupling was 1.0 ps. Semi-isotropic pressure coupling was used in the simulation with a compressibility of $4.5 \times 10^{-5}\ bar^{-1}$. Coulombic interactions were treated with the generalized reaction field method [94] with $\epsilon = 66$. A 1.4 nm cutoff distance was used for the short-range electrostatics and van der Waals interactions.

2.3.2.2 CG simulations with GROMACS

Coarse-grained simulations were set up using our model. 50 ns isothermal-isobaric (NPT) simulations were run after 10 ns of randomization simulations. In the randomization process, all chitosan beads were set to slightly repel each other so that polymer chains can disperse and fill the entire simulation box. The last 10 ns of NPT data was used for analysis. The timestep of the CG simulations was 20 fs, and the simulation integrator was leapfrog [92]. Nose-Hoover temperature coupling [95, 96] and Parrinello-Rahman pressure coupling schemes [97] were used with a reference temperature of 300 K, and pressure of 1 atm. The relaxation time of the temperature coupling was 1 ps and of the pressure coupling was 10 ps. Isotropic pressure coupling was used in the simulation with a compressibility of $4.5 \times 10^{-6}\ bar^{-1}$. Coulombic interactions were treated with particle-mesh Ewald method [98, 99] with $\epsilon = 2.5$. A 1.6 nm cutoff distance was used for the short-range electrostatics and van der Waals interactions. The constraint algorithm LINCS was used to constrain the MARTINI polarizable water dummy bonds [100] (For details of MARTINI polarizable water model, see Ref [90]).

12 simulations were set up with different water contents and pH. Water content was modeled by changing concentrations of chitosan polymer chains in the simulation box. 20, 40, 60, and 80 chitosan 30-mer polymer chains were randomly put into the simulation box and solvated with around 37000 polarizable MARTINI water beads corresponding to water contents of 95.4%, 91.1%, 86.4%, and 82.3% respectively. Solution pH was modeled by changing the percentage of protonated chitosan B3 bead using the Henderson-Hasselbalch equation. 0%, 50%, and 100% of chitosan B3 side chain beads were randomly protonated corresponding to pH of >10.5 (<0.01% protonation), 6.5 (∼50% protonation, pKa≃ 6.5), and <2.5 (>99.99% protonation) respectively.

2.3.2.3 CG simulations with LAMMPS

We transferred the simulations from GROMACS to LAMMPS so that we could deform the box size in the simulation to measure the elastic moduli of chitosan hydrogels. The same sets of water contents and pH combinations were used as in the GROMACS NPT simulations. LAMMPS CG simulations were set up using our model. The initial conformation was taken from the last frame of 50 ns GROMACS NPT runs. The timestep of the CG simulation was 20 fs, and the simulation integrator was velocity-Verlet [101]. Nose-Hoover temperature coupling [95, 96] and Parrinello-Rahman pressure coupling schemes [97] were used with a reference temperature of 300 K, and pressure of 1 atm. The damping parameter of temperature and pressure coupling was 2 ps. An isotropic pressure coupling was used in the simu-

lation during equilibration steps. 2.5 ns canonical ensemble (NVT) simulations and 2.5 ns isothermal-isobaric (NPT) simulations were run as an equilibration step, and 10 ns box deformation simulations were performed after the equilibration step. In box deformation simulations, the LAMMPS command "fix deform" was used with the "erate" option to change the dimension of the box at a constant rate every step in order to set the overall box deformation in X axis to be 2 times of the original size in 10 ns of deformation simulations. During the box deformation step, Y, Z directions were coupled with 1 atm Parrinello-Rahman barostat with a damping parameter of 2 ps. In both equilibration and deformation steps, Coulombic interactions were treated with particle-particle particle-mesh (PPPM) method [102] with $\epsilon = 2.5$. A 1.6 nm cutoff distance was used for the short-range electrostatics and van der Waals interactions. The constraint algorithm SHAKE was used to constrain the MARTINI polarizable water dummy bonds [103, 104] (For details of MARTINI polarizable water model, see Ref [90]). To account for the 1-3 exclusions inside the MARTINI polarizable water bead, we modified the "special_bonds" command in LAMMPS so that interactions that were excluded in our model are not calculated, instead of being multiplied by a factor of zero, which would cause a division by zero if the dummy particles inside the CG polarizable water overlaps.

2.3.3 Analysis Methods

2.3.3.1 Static structure factor

The static structure factor quantifies the spatial correlation of chitosan beads in the polymer network structure over a distance (2π/q). The peak in low-q regime of the static structure factor marks the long range order of the polymer assembly in the system. The static structure factor is related to the radial distribution function g(r) by a Fourier transformation, given by

$$S(q) = 1 + \rho \int_V d\mathbf{r} e^{-i\mathbf{qr}}(g(r) - 1) \tag{2.2}$$

where g(r) is the radial distribution function from all chitosan beads to all chitosan beads.

2.3.3.2 Elastic modulus analysis

Elastic moduli of chitosan hydrogel systems were measured by fitting the stress-strain curves during box deformation. Standard error of the fitted elastic modulus is computed from the covariance matrix obtained when fitting the stress-strain curves. In LAMMPS, the "fix deform" command was used to deform the simulation box with a constant strain rate. The measured stress-strain curves were then fitted with a linear function at the zero strain point to calculate the elastic modulus as the slope of the stress-strain curve.

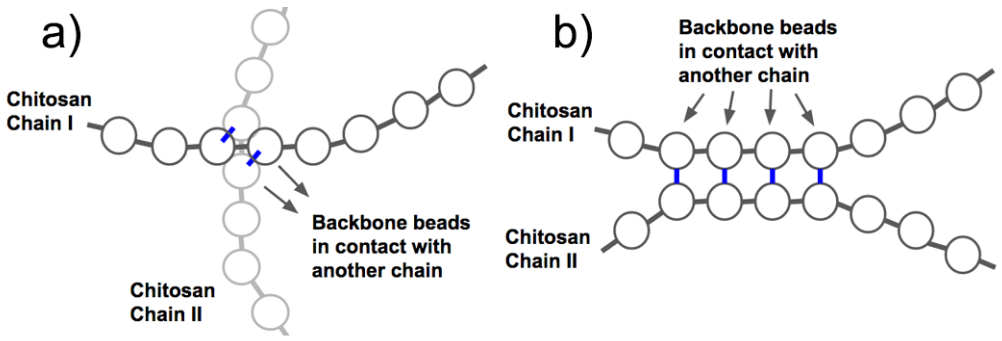

Figure 2.4: Physical crosslinking pattern schematic illustrations. (a) Perpendicular crosslinking between two chitosan polymer chains; (b) Parallel crosslinking between two chitosan polymer chains.

2.3.3.3 Percolation analysis

Percolation analysis was performed to quantify the connectivity of the chitosan hydrogel network structure through the simulation box. Any two chitosan CG beads within 5.5Å (which includes the first RDF peak from all chitosan beads to all chitosan beads) were considered connected, and connected polymer chains were defined as percolated if they met both the following conditions: 1) the polymer chains must span the entire box; 2) the polymer chains must connect to themselves through the periodic boundary in all directions. The percolation probability is calculated by sampling the fraction of percolated time every 1ns. The percolation lifetime was calculated by fitting the time series of percolation probability with a sigmoidal curve marking the transition between percolated and un-percolated states.

2.3.3.4 Crosslinking Pattern Analysis

To characterize the crosslinking pattern of a chitosan hydrogel network as shown in Figure 2.4, we calculated the polymer chain crosslinking angle cosine ($\cos(\theta)$). The $\cos(\theta)$ ranges from 0 to 1, where 0 means completely perpendicular and 1 means completely parallel. The crosslinking orientation between chitosan polymer chains was calculated from adjacent crosslinking chitosan monomers. The cutoff distance between chitosan monomers is 7.5Å, which includes the first peak of the B2-B2 (backbone bead to backbone bead) radial distribution function. We defined all chitosan monomers within a distance of B2-B2 beads of 7.5Å to be in contact, and a pair of monomers in contact with a crosslinking angle $\cos(\theta)$ over 0.8 was counted as parallel contacts. We then summed up all parallel contacts within the chitosan polymer network to quantify the amount of parallel crosslinking in the system.

2.3.3.5 Crosslinking Energy Definition

Crosslinking energy is defined as the sum of interaction potentials between two adjacent chitosan monomer units. For each chitosan monomer, we find all chitosan beads in other chains within its 7.5Å (including first peak of radial distribution function from all B2 beads to all B2 beads) and calculate the sum of all non-bonded interactions between the chitosan monomer and all other chitosan beads.

2.3.3.6 Pore Size Distribution

Pore size distribution (PSD) histograms are calculated with Zeo++ software [105]. The software uses a number of Monte Carlo samples per unit cell to probe the distribution of pore sizes. The command "network" was used with both *chan_radius* and *probe_radius* set to 1.0 Å, where *chan_radius* is the radius of a probe used to determine accessibility of the pore. *probe_radius* is the radius of a probe used in Monte Carlo sampling. The number of Monte Carlo sampling per atom is set to 5000. To display PSD histograms and compare with static structure factor, we have converted the PSD histogram X axis to be $2\pi/D$, where D is the pore diameter.

2.4 Results and Discussions

The characteristic percolation time is listed in Table 2.3 and is defined as the half-life time required for the hydrogel network to transition from unpercolated to percolated state. As shown in Table 2.3, under basic conditions (pH$>$ 10.5), all chitosan networks percolate within 20($\pm$0.03)ns starting from a random spatial distribution of polymers. At a pH of 6.5, the chitosan hydrogel network percolate at a much slower rate but still percolate. When the solution is acidic (pH$<$6.5), chitosan polymers stay unpercolated all the time. In experiments, percolation is an indicator of gelation in chitosan polymers. The pH-dependent percolation results are in agreement with experimental observations that chitosan films are usually made at a pH over 5 [60].

Typical conformations of a chitosan hydrogel networks with different pH and

Table 2.3: Characteristic percolation time (nanosecond in CG timescale) in chitosan hydrogel systems with different pH and polymer molar concentrations. Note here the coarse-grained simulation time is not directly scaled to real time.

Concentration (%)	pH > 10.5	pH 6.5	pH < 2.5
4.6	14.8±0.03	> 50	Not Percolated
8.9	3.4±0.04	18.3±0.04	Not Percolated
13.6	0.70±0.001	4.0±0.006	Not Percolated
17.7	0.03±0.001	2.0±0.005	Not Percolated

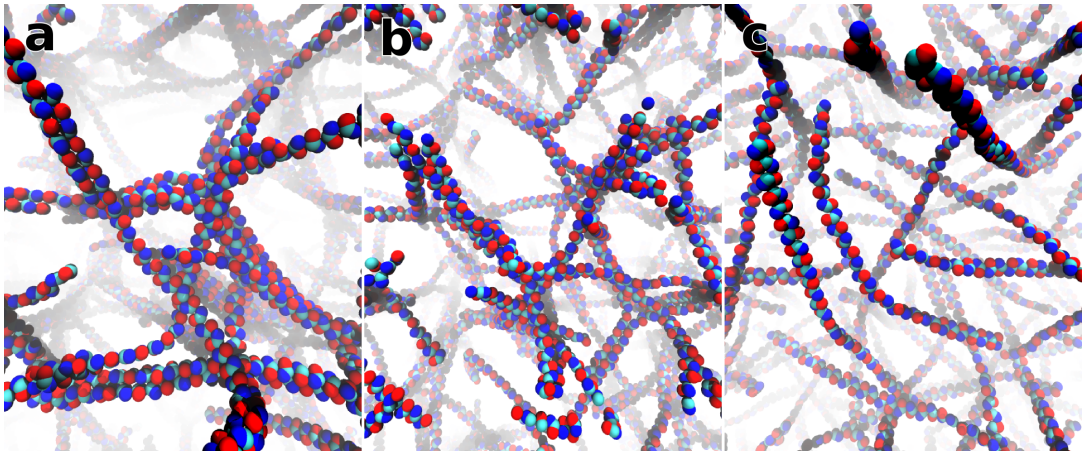

Figure 2.5: Typical conformations with a polymer concentration of 8.9%, and pH of (a) >10.5, (b) 6.5, (c) <2.5. Red, cyan, and blue beads correspond to chitosan B1, B2, and B3 beads, respectively.

a polymer concentration of 8.9% are shown in Figure 2.5. Chitosan polymer chains self-assemble into a physically crosslinking network when solution pH is higher than 6.5 (Figure 2.5c-d), and this network can not be formed when pH is low (Figure 2.5e). This pH-dependent self-assembly behavior has been reported in many experi-

ments and is critical for manufacturing bio-based film [24, 26, 67, 106]. The observed persistence length of chitosan chains in the simulations is around 8.3nm, which is in agreement with reports from experimental measurements ranging from 5 to 15nm [68–71]. With X-ray diffraction experiments [73, 75], chitosan polymers have been found to mostly adopt an extended 2-fold helix conformation [72, 75], which indicates a zig-zag structure. The extended 2-fold helix typically has dihedral angle ψ, ϕ values (as defined by atoms O5-C1-O1-C4' and C1-O1-C4'-C3' respectively, see Figure 2.5 for dihedral angle definitions) around -98° and 92° [75]. The dihedral angle distribution map of the CG model agrees well with atomistic simulation results [29] capturing correctly the preference over a 2-fold helix. Therefore, our CG chitosan model captures comparable pH-dependent self-assembly behavior and persistence length as in experiments, and is able to reproduce the most common secondary conformation observed in crystal structures and atomistic simulations.

The gelation of a hydrogel network at medium to high pH in our simulations can be characterized by the long-range order in the packing of chitosan polymers. This long-range order is characterized by the static structure factor ($S(q)$) shown in Figure 2.6. A peak at S(q) peak in the low frequency regime indicates long-range order in the network. Figure 2.6 shows that there is a clear distinction of long-range order (as in peaks at $q < 1$) for different pH at all polymer concentrations. At a pH over 10.5, the long-range order in the network is significantly higher than a pH of 6.5. While at low pH, no clear long-range order is observed. The pore size distribution, shown in Figure 2.6 insets, was performed using the Zeo++ software [105]. We found that a small peak in the blue curve (pH>10.5) near q = 2-3 nm^{-1} in Figure

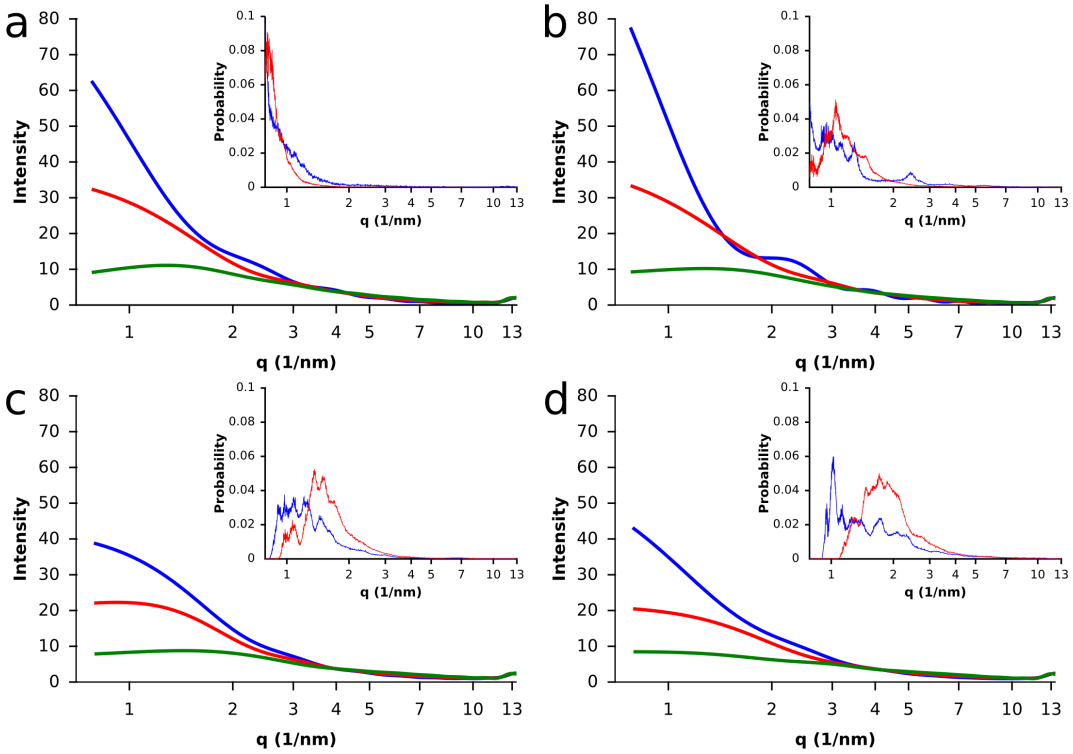

Figure 2.6: Static structure factor ($S(q)$) of chitosan polymer networks at different pH (blue: > 10.5; red: 6.5; green: < 2.5) and polymer concentrations (a: 4.6%, b: 8.9%, c: 13.6%, d: 17.7%). Insets are pore size distributions of chitosan polymer networks with the X axis converted to frequency q, defined as $2\pi/D$, where D is the diameter of pores in nanometer. Green curves are not shown in the insets because solvated chitosan chains do not form a network structure.

2.6b was associated with a peak in the pore size distribution at the same location. Also, high peaks at q <1 observed in blue and red curves in Figure 2.6a,b could be associated with pores formed around similar sizes.

To investigate how pH alters the mechanical properties of chitosan networks, the elastic modulus is computed. Box deformation simulations were performed

Table 2.4: Mechanical property of chitosan hydrogel. Elastic moduli (in MPa) with different pH and polymer concentrations are shown. Errors indicate the standard error of the calculated elastic modulus.

Concentration (%)	pH>10.5	pH 6.5	pH<2.5
4.6	14.0±0.2	6.5 ±0.2	5.0±0.2
8.9	21.3±0.2	15.3±0.2	9.1±0.2
13.6	38.9±0.3	32.3±0.3	15.9±0.3
17.7	66.0±0.5	57.2±0.5	39.6±0.5

along an axis, and the elastic moduli was computed from the induced stress-strain curve. Table 2.4 demonstrates the elastic modulus of chitosan hydrogel systems with different pH and polymer concentrations. Elastic moduli of chitosan hydrogel networks are positively correlated with polymer concentration and pH. The increase of elastic modulus with polymer concentration and pH agrees with many experiments in chitosan-based materials [107–111]. In addition, the scale of elastic moduli (10-60 MPa) is within the same order of magnitude as experimental observation (around 12 MPa by Kitagawa *et al.* [78]).

Furthermore, to understand how pH alters structural and mechanical properties of chitosan hydrogels from a molecular perspective, physical crosslinking patterns in chitosan polymer network are analyzed. The crosslinking reorientation can be characterized by the ensemble average of crosslinking angle cosine ($\langle\cos(\theta)\rangle$) between adjacent chitosan monomer units as in Figure 2.7. The crosslinking angle cosine ($\cos(\theta)$) ranges from 0 to 1, where 0 is completely perpendicular and 1 is

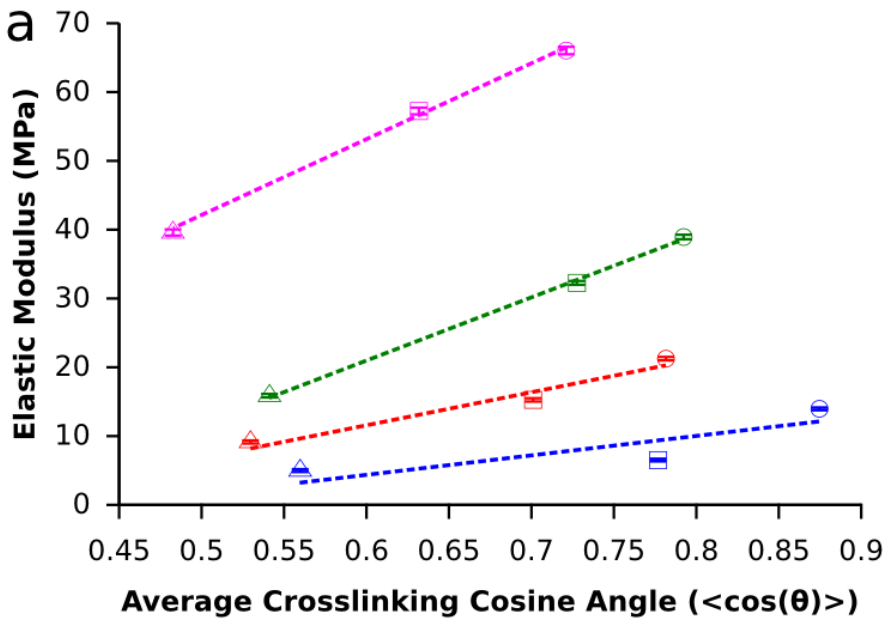

Figure 2.7: Analysis of chitosan polymer network crosslinking pattern. (a) Average pairwise crosslinking angle cosine between crosslinking chitosan polymer chains versus network elastic modulus; Different polymer concentrations are represented in blue (4.6%), red (8.9%), green (13.6%), and magenta (17.7%). Different pH of chitosan systems is represented as empty triangles (pH$<$ 2.5), squares (pH 6.5), and circles (pH$>$ 10.5). Error bars indicate the standard error of the calculated elastic modulus.

completely parallel. Figure 2.7 depicts the elastic modulus against $\langle\cos(\theta)\rangle$. For systems with same concentrations of chitosan polymer, the $\langle\cos(\theta)\rangle$ increases with the increase of hydrogel elastic modulus and solution pH (Figure 2.7a). In that sense, the increase of solution pH leads to a preference for polymer chains to crosslink in parallel, and consequently increases the mechanical strength of the hydrogel. Also, the magenta curve with polymer concentration of 17.7% shifts toward lower $\langle\cos(\theta)\rangle$

near 0.5. There is no preference toward either parallel or perpendicular crosslinking when $\langle\cos(\theta)\rangle$ has a value of 0.5. Therefore, this suggests that the overall polymer crosslinkings become more isotropic and both perpendicular and parallel crosslinkings play an important role at higher polymer concentration.

To reveal the underlying molecular mechanism affecting the different crosslinking patterns at a molecular level, we have characterized the potential of mean forces of the chitosan systems as a function of two reaction coordinates. We used the $\cos(\theta)$ as one reaction coordinate and defined the crosslinking energy as another reaction coordinate. Crosslinking energy is the sum of interactions between one chitosan monomer unit to all monomer units adjacent to it in other chitosan chains. In Figure 2.8a (pH 6.5, 17.7% polymer concentration), 3 crosslinking states are observed in the potential of mean force (PMF) plot (referred to as type I_a, I_b, and II). Both type I_a and I_b have a crosslinking $\cos(\theta)$ of 1, while type II has a $\cos(\theta)$ less than 0.2. Type I is a stable parallel crosslinking with the energy around -140kJ/mol, and for type I_b and type II the crosslinking energy is around -60kJ/mol. Type I_a corresponds to a typical unit of one chitosan chain crosslinking with two or more other chains (Figure 2.8e), while type I_b is crosslinking with only one other chain. The crosslinking unit of type II is two chitosan chains crosslinking in perpendicular. Both type I_a and I_b are very favorable states (PMF(I_a)= 3.2 kT, PMF(I_b)=2.2 kT), and become more favorable as pH increases (Figure 2.8b, pH>10.5, 17.7%, PMF(I_a)= 2.2 kT, PMF(I_b)=0.7 kT). This explains why the average $\cos(\theta)$ shifts toward 1 as pH increases for all polymer concentrations (Figure 2.7). The transition between these two states has a low energy barrier (PMF(I_a, I_b)=1.6 kT). State type

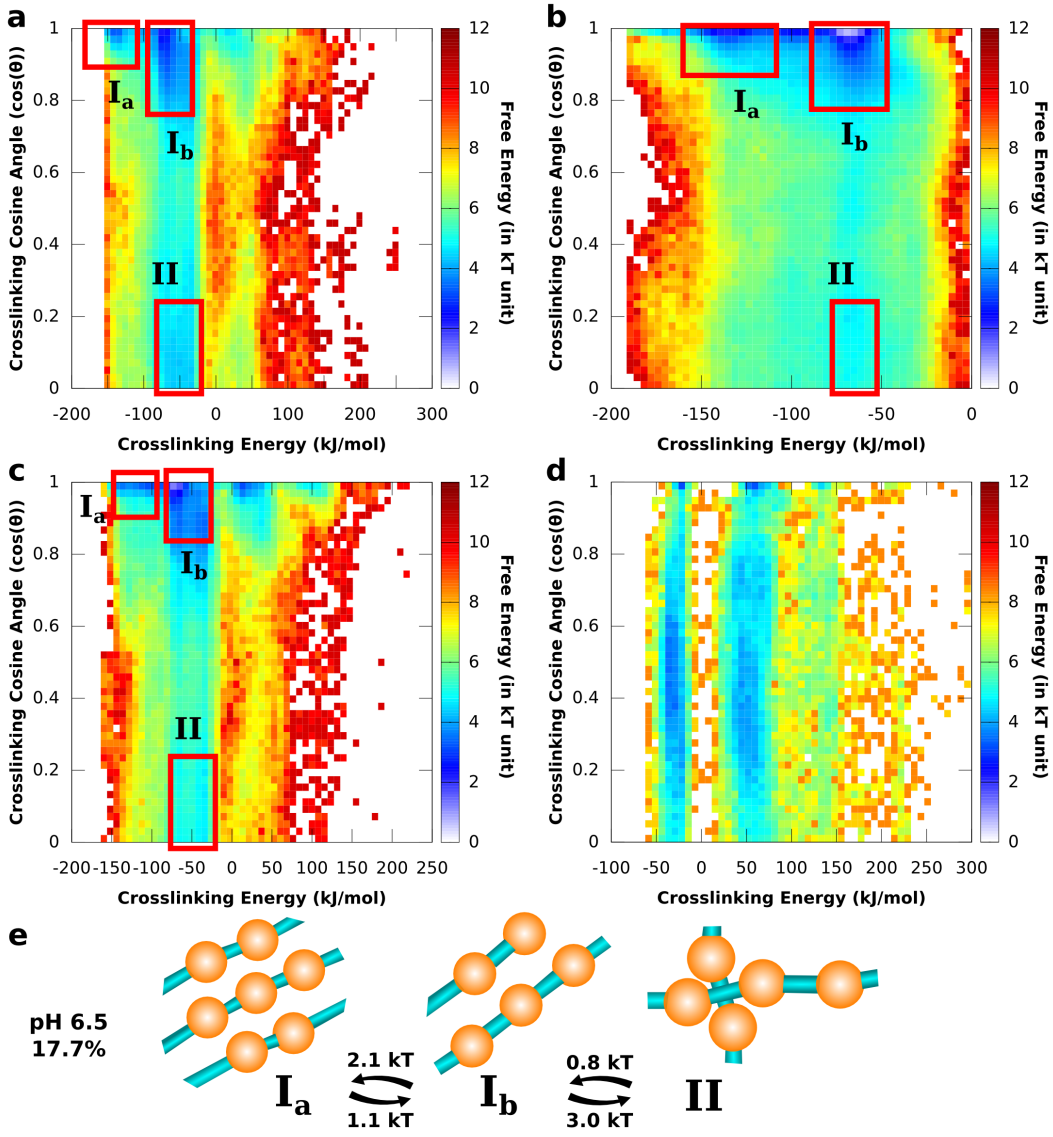

Figure 2.8: Potential of mean force with reaction coordinates of crosslinking energy (in kJ/mol) and cos(θ). Chitosan systems are shown as polymer concentration and pH of (a) 17.7% and 6.5; (b) 17.7% and pH>10.5; (c) 8.9% and 6.5; (d) 8.9% and <2.5; (e) Basic unit of each crosslinking state and the energy barriers in kT units between states. A typical crosslinking conformation could be a combination of such units. For example, a conformation of one chitosan chain crosslinking with two parallel chains in perpendicular is a combination of both state type I_b and type II).

II (Figure 2.8a, pH 6.5, 17.7%, PMF(II)=4.4 kT) is not as favorable as type I_a and I_b states. The PMF of state type II is even less favorable in both high pH (Figure 2.8b, pH>10.5, 17.7%, PMF(II)=4.7 kT) and low polymer concentration (Figure 2.8c, pH 6.5, 13.6%, PMF(II)=4.8 kT) systems. This is in agreement with Figure 2.7, where $\langle\cos(\theta)\rangle$ shifts toward lower value with low pH or high polymer concentration. The transition between type I_b and type II has a relatively lower energy barrier (PMF(I_b, II)=1.9 kT) than the transition directly from type I_a to type II (PMF(I_a, II)=2.7 kT). Therefore, the type I_b (parallel crosslinking between only two chains) works as an on-pathway state between type I_a and II, which suggests three or more chitosan chains crosslinking in parallel usually break up into two before they further switch to a perpendicular crosslinking. When the solution pH is below 2.5 (Figure 2.8d, pH<2.5, 17.7%), almost all three types of crosslinking states disappear. Only a small percentage of state I_b still remains. $\cos(\theta)$ distributes almost symmetrically about 0.5, indicating a preference for isotropic orientation of chitosan chains at low pH.

2.5 Conclusion

In this chapter, a pH-dependent self-assembly hydrogel network of chitosan polymers was successfully constructed using a water-explicit CG model. We have found that physical crosslinking patterns have a significant impact on chitosan hydrogel mechanical properties. Increasing the pH or polymer concentrations leads to an increase of elastic modulus in chitosan systems through the change of crosslinking

patterns. Parallel crosslinking is dominant when the polymer concentration is low, while at higher polymer concentrations both crosslinkings in parallel and perpendicular play an important role in the hydrogel mechanical strength. Three states of crosslinking chains are identified corresponding to a stable parallel crosslink (type I_a), on-pathway parallel crosslink (type I_b), and perpendicular crosslink (type II). The state type I_b acts as an on-pathway state between states type I_a and type II.

Chapter 3: Effect of Lipid Head Group Interactions in Membrane Properties and Membrane-Induced Cationic β-Hairpin Folding

3.1 Overview

This chapter is based on the author's publication: Effect of Lipid Head Group Interactions in Membrane Properties and Membrane-Induced Cationic β-Hairpin Folding. Sai J. Ganesan, Hongcheng Xu* and Silvina Matysiak. Physical Chemistry Chemical Physics, 2016. (* co-author)*

Membrane interfaces (mIFs) are ubiquitous components of living cells and are host to many essential biological processes. One key characteristic of mIFs is the dielectric gradient and subsequently, electrostatic potential that arises from dipolar interactions in the head group region. In this chapter, we present a coarse-grained (CG) model for anionic and zwitterionic lipids that accounts for dipolar intricacies in the head group region. Prior work on adding dipolar interactions in a coarse grained (CG) model for peptides enabled us to achieve α/β secondary structure content *de novo*, without any added bias. We have now extended this

idea to lipids. To mimic dipolar interactions, two dummy particles with opposite charges are added to CG polar beads. These two dummy charges represent a fluctuating dipole that introduces structural polarization into the head group region. We have used POPC (1-palmitoyl-2-oleoyl-*sn*-glycero-3-phosphocholine) and POPS (1-palmitoyl-2-oleoyl-*sn*-glycero-3-phospho-L-serine) as our model lipids. We characterize structural, dynamic, and dielectric properties of our CG bilayer, along with the effect of monovalent ions. We observe head group dipoles to play a significant role in membrane dielectric gradient and lipid clustering induced by dipole-dipole interactions in POPS lipids. In addition, we have studied membrane-induced peptide folding of a cationic antimicrobial peptide with anticancer activity, SVS-1. We find that membrane-induced peptide folding is driven by both (a) cooperativity in peptide self interaction and (b) cooperativity in membrane-peptide interaction. In particular, dipolar interactions between peptide backbone and lipid head groups contribute to stabilizing folded conformations.

3.2 Introduction

Zwitterionic phospholipid phosphatidylcholine (PC), and anionic phospholipid phosphatidylserine (PS) comprise 40-55% and 3-10% respectively, of total mammalian cell membrane phospholipids [112]. Their structural and dynamical properties have been found to play important roles in a number of biological processes. Electrostatic interactions between lipid head groups have an effect on a membrane's internal electrical dipole potential, which varies from 100 mV to 400 mV, depending

on the composition of lipids [113]. This dipole potential has also been shown to dramatically impact ion channel permeability in biological membranes [114].

Biological membrane interfaces (mIF) provide a unique dielectric environment in which proteins undergo conformational transitions from a water-soluble to a membrane associated state [115,116]. Short model peptides, especially antimicrobial peptides (AMPs), have been extremely useful in characterizing energetics of interfacial folding [36,37]. AMPs are cationic peptides with a significant level of hydrophobicity. Anticancer peptides (ACP) are AMPs designed to target tumor cells, one such *de novo* designed ACP is SVS-1 ($KVKVKVKV^DP^LPTKVKVKVK-NH2$) [38]. SVS-1, like AMPs, are disordered in the aqueous phase (bioinactive), but is fully structured upon partitioning onto an interface (bioactive) [38]. This ACP is known to fold into a β-sheet on interaction with negatively charged vesicles [38]. The literature on experimental and computational characterization of biophysical properties of AMPs is vast [117–120]. It has been proposed that the energetic cost of partitioning unfolded peptides into mIFs is reduced by secondary structure formation or intermolecular hydrogen bonds [20]. Membrane lipid composition is known to play a crucial role as well; for example, differences in the amount of acidic membrane phospholipids and cholesterol are known to play a critical role in specificity of magainins [39,40]. However, the balance of driving forces between the two states (water soluble and membrane bound) remains to be understood. Coarse-grained membrane models that capture the right dielectric gradient, and peptide models that can capture protein secondary structures should have essential ingredients to decode such a process.

Molecular simulations are being increasingly used to improve our knowledge of microscopic phenomena [121,122]. Atomistic simulations have contributed to the understanding of many membrane processes [123–127], including the existence of anionic lipid clusters, mediated by ion-dipole or hydrogen bond (a type of dipole-dipole interaction) networks in both monocomponent and mixed bilayers [128–130]. It has been hypothesized that these clusters could be intermediate structures on pathway to experimentally observed lipid phase separation in mixed PC/PS bilayers on longer time scales. [131]

Unlike atomistic simulations, coarse-grained (CG) models aid in both exploring larger length and time scale molecular phenomena, and in narrowing down the key interactions responsible for significant system characteristics. CG simulations of lipid systems have largely proven to be efficient in giving us a thorough and coherent picture of membrane structure and have been used in the past to explore lipid domain formation in mixed bilayers for systems that do not have anionic lipids [132–134]. There exist a large number of CG models that have yielded significant results and extended our understanding of membrane molecular processes [1, 135–139]. Among them, a transferable model called MARTINI force field [1,139], built on thermodynamic data of oil/water partitioning coefficient, achieves a broader range of applications without the need for re-parametrization.

In this chapter, we present a CG lipid model that can be used to explore the role of head group dipoles in membrane structure and interfacial peptide folding. This model has roots in the MARTINI force field, and is combined with a new Water-Explicit Polarizable PROtein Model (WEPPROM) developed by some of us [140]

and Yesylevskyy's polarizable water model [90]. By modeling a protein backbone bead as a flexible dipole, we were able to achieve *de novo* helix and sheet content without any biases. In WEPPROM, the dipolar interactions can be considered as pseudo hydrogen bonds, which contribute to cooperativity in folding secondary and supersecondary structures. An analog to our model is the multipole CG model developed by Ren *et al.* [141–143]

We have chosen a zwitterionic lipid POPC, and an anionic lipid POPS, as model lipids. The choice of the above two lipids is governed by the use of POPC/POPS mixed systems as common models in the study of plasma membranes [144, 145]. In this chapter, we explore (a) the role of head group dipole interactions in membrane structure and dynamics, (b) the effect of monovalent ions on lipid dipole interactions and bilayer properties, and (c) membrane-induced folding of SVS-1.

3.3 Methods

3.3.1 Lipid Model

A mapping scheme consistent with the MARTINI model for POPC and POPS lipids is used, and is shown in Figure 3.1a. A phospholipid molecule is mapped onto a structure consisting of 13 CG sites made of 3 different bead types. The bead types used are: charged *(C)*, polarizable *(Pol)*, and hydrophobic *(H)*. We also use a set of bead subtypes similar to the MARTINI force field, with distinct modifications in the Lennard-Jones (LJ) parameters, to account for all the CG sites. *C0*, *C+* and *C-* are charged bead subtypes, where *C+* is a representative hydrogen bond donor, *C-*

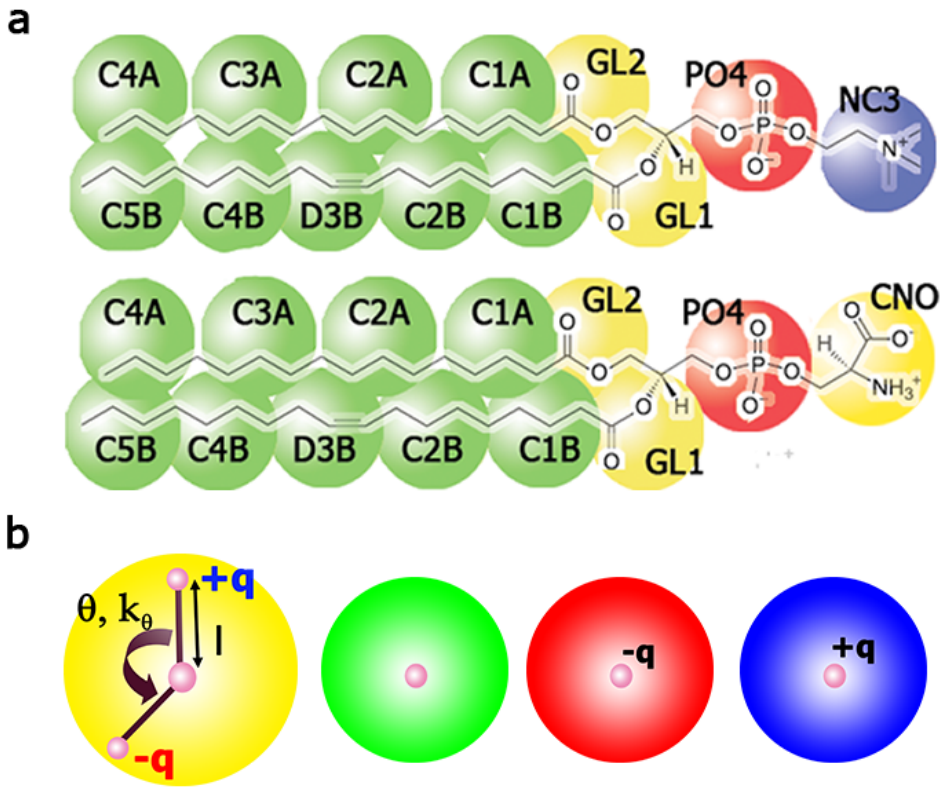

Figure 3.1: (a) Mapping scheme for POPC and POPS coarse-grained lipids; colors: green, hydrophobic bead; yellow, polarizable beads ; red, negatively charged bead; blue, positively charged bead. (b) Bead types: yellow represents polarizable beads (example : CNO, GL1, GL2), van der Waals radius of the bead encloses positively (+q/P) and negatively (-q/M) charged dummy particles (example:, CNP and CNM, G1P and G1M, G2P and G2M respectively) . The tunable parameters (l, q, θ, k_θ) are depicted. Blue bead represents a positively charged bead, red bead represents negatively charged bead, and green represents hydrophobic bead.

acceptor, and *C0* is neither. *Pol1* and *Pol2* are subtypes of the polarizable bead, sorted in order of decreasing polarity. *H1* and *H2* are subtypes of the hydrophobic

bead, in decreasing order of hydrophobicity. As depicted in Figure 3.1a, the PC head group region consists of two hydrophilic groups: choline (NC3) and phosphate (PO4) with *C0* and *C-* bead types respectively. The PS head group region also consists of two hydrophilic groups: serine (CNO) with oppositely charged dummy particles (CNM and CNP), as shown in Figure 1b, and phosphate (PO4), with *Pol1* and *C-* bead subtypes respectively. For both lipids, two sites of intermediate hydrophilicity (bead subtype *Pol2*) are used to represent the glycerol ester groups (GL1 and GL2), each with oppositely charged dummy particles (G1M, G1P and G2M, G2P), as shown in Figure 3.1b. The oleoyl tail is modeled with 5 beads, 4 of *H1* subtype and a central bead of *H2* subtype (a less hydrophobic bead to model the double bond). The palmitoyl tail is modeled with 4 beads of subtype *H1*. All ions used are modeled as hydrated ions with a point charge, using charged bead subtypes *C+* or *C-*

The CG phospholipid model is combined with the polarizable coarse-grained (pCG) water model developed by Yesylevskyy et al. [90]. The pCG bead of our lipid model consists of three interaction sites, of which one is the center of mass site and the other two are dummy particles with opposite charges, as depicted in Figure 3.1b. The dummies are added into the polarizable bead only to create a flexible dipole which interacts with other particles via electrostatic interactions. The Lennard-Jones pairwise interactions are defined between the main CG sites. A constraint with a distance (l) is defined between dummies and the main site, and all the three interaction sites are bound by a cosine squared angle potential (equilibrium angle θ and angular force constant k_θ) to control the rotation of dummy particles.

To avoid overpolarization, a small repulsive core is added to dummy particles, as commonly done in polarizable all-atom force fields [146]. All 1-2 non-bonded interactions are excluded between the main CG sites and their corresponding embedded dipole particles. In addition, the non-bonded interactions between dummy particles inside a polarizable bead are excluded as well. The mass of a CG bead (72 a.m.u) is distributed equally among the three particles (24 a.m.u. each) in polarizable beads.

3.3.2 Lipid Force Field Parameters

Our force field consists of bonded (harmonic bond and angular potential for lipid and peptide) and non-bonded terms (Lennard-Jones and Coulombic potentials). All non-dipolar bonded interactions are based on the MARTINI force field [1, 139], and are fine-tuned using MARTINI's LJ parameter scale as a baseline. The bonded distance between two adjacent head group beads is 0.37 nm and between adjacent tail beads is 0.47 nm, both with a bond strength of of 298.8 kcal/mol. The only angle defined among head groups are between the phosphate and ester beads (PO4-GL1-GL2), which is set to 120°. Angles involving tail groups are set to 180°. The interaction strength of both the angles are set to 6.0 kcal/mol. There is an exception for the double bond in the carbon tail, which is set to 120° with an interaction strength of 10.8 kcal/mol.

The parametrization of non-bonded terms is done in two stages to account for (a) thermodynamic parameters or free energy values of partitioning, hydration, and vaporization of each bead type, and (b) dipole moments of polarizable beads. The

Table 3.1: Table of vaporization, hydration and partition free energy in kcal/mol. The partition free energy is evaluated for water/hexadecane interface. $\Delta G^{\mathbf{M}}$ is the free energy calculated using the MARTINI model [1], $\Delta G^{\mathbf{P}}$, with our water-explicit polarizable coarse-grained model, and $\Delta G^{\mathbf{E}}$ is the free energy from experiment [1].

Bead	Chemistry	Examples	$\Delta G^{\mathbf{M}}_{vap}$	$\Delta G^{\mathbf{P}}_{vap}$	$\Delta G^{\mathbf{E}}_{vap}$	$\Delta G^{\mathbf{M}}_{hyd}$	$\Delta G^{\mathbf{P}}_{hyd}$	$\Delta G^{\mathbf{E}}_{hyd}$	$\Delta G^{\mathbf{M}}_{part}$	$\Delta G^{\mathbf{P}}_{part}$	$\Delta G^{\mathbf{E}}_{part}$
C0	C_3N^+	choline	-	-	-	-6.0	-6.0	-	<-7.2	<-7.2	-
C+	H_3N^+-C_3	1-propylamine	-	-	-	-6.0	-6.0	-	<-7.2	<-7.2	-
C-	PO_4^-	phosphate	-	-	-	-6.0	-6.0	-	<-7.2	<-7.2	-
Pol1	H_2N-C_2=O	acetamide	sol	sol	sol	-6.7	-6.9	-9.6	-6.7	-6.9	-6.5
Pol2	C-O-C=O	methylformate	-3.1	-2.2	-3.8∼-5.5	-2.2	-2.4	-2.9∼-3.8	-1.7	-1.9	-1.0∼-1.4
H1	C_4	butane	-2.4	-2.4	-2.6	3.3	4.5	2.2∼2.4	4.3	5.0	4.3
H2	C_2=C_2	2-butene	-2.4	-2.4	-3.8	1.2	3.8	-0.2∼-0.5	3.1	4.1	2.9

dipole moment of polarizable beads is initially parameterized to match that of the corresponding chemical group in atomistic detail from all-atom simulations. There are four parameters for the polarizable CG bead that can be tuned to obtain the desired average dipole moment (l, q, θ, k_θ). Since the polarization of the bead inevitably adds extra electrostatic interactions to the system, the lipid dipole moment and Lennard-Jones (LJ) interactions of polarizable beads are carefully tuned down as a compensation to match, as close as possible, the free energy of partitioning, hydration and vaporization, as depicted in Table 3.1, using the method outlined by Marrink et al. [1]. The final dipole parameters for the CNO bead, with an average dipole moment of 8.76 Debye, is l=0.20 nm, q=0.4557, θ=180°, k_θ=4.78 kcal/mol. For GL1/GL2 bead, with an average dipole moment of 1.35 Debye, is l=0.14 nm,

Table 3.2: Interaction strength ϵ for LJ interactions (kcal/mol)

Bead (Type)	C0	C+	C-	P1	Pol1	Pol2	W	H1	H2
C0	IV	VII	VII	III	O*	V	II	VII	VI
C+	VII	IV	III	III	O*	II	I	VII	VI
C-	VII	III	IV	III	O*	IV	I	VII	VI
P1	III	III	III	I	I	III*	I	VIII	VI
Pol1	O*	O*	O*	I	I*	I*	I*	VIII	VI
Pol2	V	II	IV	III*	I*	V	IV*	VI	VI
W	II	I	I	I	I*	IV*	III	VIII**	VI**
H1	VII	VII	VII	VIII	VIII	VI	VIII*	IV	IV
H2	VI	VI	VI	VI	VI	VI	VI**	IV	IV

(O: ϵ=1.35 kcal/mol, I: ϵ=1.20 kcal/mol, II: ϵ=1.10 kcal/mol, III: ϵ=0.95 kcal/mol, IV: ϵ=0.85 kcal/mol, V: ϵ=0.75 kcal/mol, VI: ϵ=0.65 kcal/mol, VII: ϵ=0.55 kcal/mol, VIII: ϵ=0.50 kcal/mol)

* 95% of the interaction strength is used to counterbalance the polarization

** 10% of the interaction strength is used to make this model compatible with our protein model [140] in hydrophobicity

q=0.175, θ=70°, k_θ=8.40 kcal/mol. The LJ parameters tuned down from the MARTINI model values corresponding to different chemical species are presented in Table 3.2. The LJ interaction strengths are divided into nine levels as follows: O) ϵ=1.35

kcal/mol, I) ϵ=1.20 kcal/mol, II) ϵ=1.10 kcal/mol, III) ϵ=0.95 kcal/mol, IV) ϵ=0.85 kcal/mol, V) ϵ=0.75 kcal/mol, VI) ϵ=0.65 kcal/mol, VII) ϵ=0.55 kcal/mol, VIII) ϵ=0.50 kcal/mol. In addition, two hydrophobic interactions, H1-W and H2-W, are also scaled down to 10% to make the lipid model compatible with our protein model [140]. The peptide model and the lipid model use the same hydrophobic scale. An effective size of σ=0.47 nm is used for all main CG interaction pairs in the LJ potential.

3.3.3 Peptide Model

The peptide model parameters were taken from our previous work [140], where we capture secondary and super-secondary structure, based on several primary sequences, in peptide folding without any added bias. The bead types of the protein model is largely consistent with the current lipid model, with an addition of a non-polarizable polar side-chain bead type *P*. SVS-1 sequence is mapped to our CG model [140] using an hydrophobicity scale [116]. Residues are mapped into polar *(P)*, hydrophobic *(H)* and charged *(C)* . Valines and prolines are modeled as hydrophobic residues *(H)*, with one polarizable backbone bead *(Pol1)*, and one hydrophobic side chain bead *(H1)*. Lysines are modeled with three beads, a polarizable backbone bead *(Pol1)*, a hydrophobic side chain bead *(H1)*, and a positively charged second side chain bead *(C+)*. Threonine is modeled as a polar residue *(P1)* with one polarizable backbone bead *(Pol1)* and one non-polarizable polar side chain bead *(P1)*. Like the polarizable beads in the lipid model, the backbone coarse-grained

bead consists of three interaction sites, the center bead BB and two dipole particles, BBm and BBp. The main site, the center of the BB bead, interacts with other CG beads through a pairwise Lennard-Jones (LJ) potential. Dipole particles BBm and BBp are harmonically bound to the central particle BB (equilibrium distance l, force constant k_l), and carry a positive and negative charge of equal magnitude (q) respectively, as depicted in Figure 3.1b. These dipole particles interact with other particles via electrostatic interactions. A cosine squared angle potential (equilibrium angle (θ) and angular force constant (k_θ)) was used to control the rotation of BBm and BBp particles. For solvation, the polarizable CG water model was used [90]. Since the locations of the dipole particles were not fixed, the model is polarizable. That is, changes in dielectric medium or local environment result in induced backbone dipoles and hence structural changes. Details on parameterization methods and force field parameters are provided in Ganesan et al. [140]. Our model currently does not account for chirality of residues. The peptide model is used with a double well α dihedral potential between backbone beads (force constant of 1.2 kcal/mol) to remove background noise [147]

$$U_{dih}(\gamma_{ijkl}) = cos(3\gamma_{ijkl}) + cos(\gamma_{ijkl} + 60) \tag{3.1}$$

$U_{dih}(\gamma_{ijkl})$ has three minima, 60° (right helix) and 180° (sheet) of equal well depth, and -60° (left helix) of a lower depth, and γ_{ijkl} is the dihedral between 4 consecutive backbone beads.

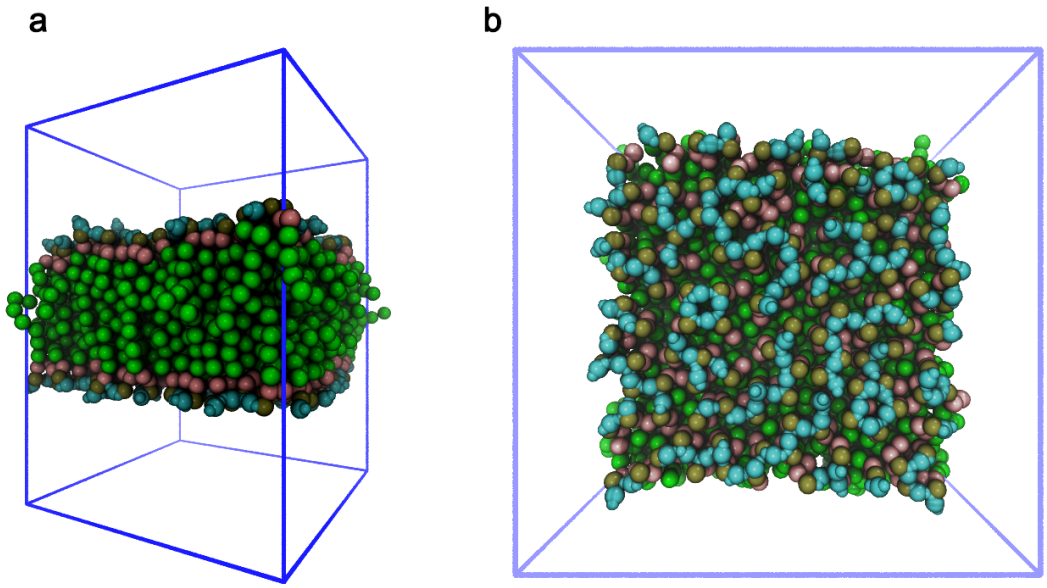

Figure 3.2: (a) Side view of POPS bilayer showing the lateral structure of the membrane. (b) Top view of POPS bilayer. Colors: serine (cyan), phosphate (tan), ester (pink), alkyl (green).

3.3.4 Simulation Parameters

All simulations are carried out using the GROMACS package version 4.5.4 [88] and visualized using VMD 1.9.1 [148]. The bilayer system is energetically minimized before an isothermal-isobaric (NPT) run, simulation data is collected for 200 ns, of which the last 100 ns is analyzed. Every membrane system studied (atomistic, MARTINI CG or pCG) is made of 240 lipids, 120 on each leaflet. A side view snapshot of POPS bilayer is illustrated in Figure 3.2a.

In CG bilayer simulations, the Nosé-Hoover [95, 96] thermostat with a time

constant of 1 ps is used to maintain a temperature of 300K, and the Parinello-Rahman [97] barostat with a time constant of 1 ps and an isothermal compressibility of $7.17\times10^{-6}(kcal{\cdot}mol^{-1}nm^{-3})^{-1}$ is used to keep the semi-isotropic pressure at 1 bar in the z direction and 1 bar in the x, y plane. The time step is 5 fs and the neighbor list is updated every 10 steps, for the CG simulations. The long-range electrostatic interactions with periodic boundary conditions (in x, y, z directions) are evaluated using the Particle Mesh Ewald (PME) method [98] with a global dielectric constant of 2.5. We use the Shift scheme beginning from 0.9 nm and switch the Lennard-Jones interaction to zero at 1.2 nm. The LINCS algorithm [100] is used for constraining dummy bonds inside polarizable beads.

Simulations with 1M NaCl are performed for both POPS and POPC systems. To make comparisons with MARTINI force field, all 4 systems (POPC without NaCl, POPS without NaCl, POPC with 1M NaCl, and POPS with 1M NaCl) are simulated using both our pCG model as well as the MARTINI force field. The simulation setups used for pCG and MARTINI simulations are mostly identical. The only difference is the increase in time step with MARTINI force field (20 fs). This was done to maintain consistency. Explicit MARTINI polarizable water model is used for both pCG and MARTINI simulations [1,90]. We also compared simulation performance between MARTINI force field and pCG, with polarizable water and POPC lipids (240 POPC lipids and 7757 water particles). For this comparison analysis, MARTINI parameters were borrowed directly from their study [1,90], while parameters detailed above were used for pCG. We found MARTINI simulations to be twice as fast as our model.

Simulations with the peptide are performed with 240 lipids of polarizable POPS, polarizable POPC, POPS without dipoles, and in water. For systems with the peptide and the bilayer, a random conformation of the peptide is introduced 5nm away from a self assembled bilayer. Counterions are added to neutralize the system. The peptide is constrained and a 10 ns NPT simulation is performed to allow the counterions to equilibrate. Constrains are removed to collect 300 ns NPT data, all of which are analyzed. For better sampling, we run 9 randomly constructed simulations of each pCG POPS system, and 6 runs for pCG POPC, POPS without dipoles (POPSnd), and in water.

Atomistic POPS and POPC bilayer simulations are performed with GROMOS 53A6 lipid force field [149]. The thermostat coupling method, velocity rescaling with a stochastic term (v-rescale), with a time constant of 0.1 ps is used to maintain a temperature of 300K. The Parinello-Rahman barostat with a time constant of 5.0 ps and isothermal compressibility $1.08\times10^{-5}(kcal\cdot mol^{-1}\cdot nm^{-3})^{-1}$ are used to maintain semi-isotropic pressure at 1 bar in the z direction and 1 bar in the x, y plane. The time step for dynamics is 2 fs and the neighbor list is updated every 5 steps. Long-range electrostatic interactions with periodic boundary conditions (in x, y, z directions) are evaluated using the PME method.

3.3.5 Analysis Methods

3.3.5.1 Calculation of Standard Errors

The estimation of the standard error for the average of the property X, is calculated by block average. Namely, the whole trajectory is divided into N blocks, each with M frames. The average of X for each block, and standard deviation from block averages is calculated. The standard error is the standard deviation over $\sqrt{N}$. To ensure the property X is independent in each M-sized block, we calculate the normalized time correlation function of the fluctuations for X,

$$C(t) = \frac{\langle \delta X(0) \delta X(t) \rangle}{\langle \delta X(0) \delta X(0) \rangle} = \frac{\langle \delta X(0) \delta X(t) \rangle}{\delta X^2} \tag{3.2}$$

where $\delta X(t) = X(t) - \langle X \rangle$, and $\langle \delta X^2 \rangle$ is the mean squared fluctuation. The size M is set to equal twice the correlation time $\tau_X = \int_0^\infty C(t)dt$. The standard error in X can also be directly obtained from:

$$se[X] = \sqrt{\frac{2\tau_X}{T_{run}}} < \delta X^2 >^{1/2} \tag{3.3}$$

All standard error calculated in this paper use the block average method.

3.3.5.2 Density Distribution

In the CG bilayer system, the density distribution for each bead in the lipid is plotted

along the bilayer normal direction. In atomistic simulations, instead of using the position of each atom, center of mass of several atoms corresponding to each CG bead is evaluated for better and more direct comparison to CG data. The scheme for atoms mapped to beads is shown in Figure 3.1a.

3.3.5.3 Susceptibility Profile

The bilayer is divided into several slabs of 5Å, in the axial direction, starting from the center of mass of the bilayer. Then the susceptibility or specific dielectric constant of each slab in a direction parallel to the membrane interface is calculated using the following equation based on linear response theory [150],

$$\chi_{//}\epsilon_0 = \beta \frac{\langle |\Delta \mathbf{M}_{//}|^2 \rangle}{\langle V \rangle} = \beta \langle |\Delta \mathbf{P}_{//}|^2 \rangle \langle V \rangle \tag{3.4}$$

where $\mathbf{M}_{//}$ and $\mathbf{P}_{//}$ are the total dipole moment and polarization density in the direction parallel to the bilayer, and the Δ indicates the difference between the value in each sample and the time-averaged one. ϵ_0 is the dielectric constant of vacuum, V is the slab volume and $\beta = 1/k_B T$. Ergodicity is assumed for time averages in the equation. To investigate the effect of polarization on bilayer dielectric profile, only polarizable beads, including serine, ester groups and water molecules in CG simulation, and their corresponding atom groups in atomistic simulation are taken into consideration. The dipole moment of the polarizable CG beads is assigned to their central main site and the dipole moment of atom group is assigned to their

center of mass.

3.3.5.4 Line Tension

Line tension of POPC and POPS bilayer is computed from a ribbon structure in the z direction. Ribbon structure is simulated using a $NP_{xy}L_zT$ ensemble and evaluated using Eq.(3.5) [151].

$$\Lambda = \frac{1}{2}\left\langle L_x L_y \left[\frac{P_{xx} + P_{yy}}{2} - P_{zz}\right]\right\rangle \tag{3.5}$$

where L_x, L_y are the sizes of the simulation box in x and y axis, and P_{xx}, P_{yy} and P_{zz} are the diagonal elements of pressure tensors along x, y, z axis.

3.3.5.5 Bilayer Potential

Electrostatic potential of the bilayer across the box is calculated using the `g_potential` program in the GROMACS 4.5 package [88]. It is computed by evaluating the double integral of the charge density ($\rho(z)$):

$$\psi(z) = -\frac{1}{\epsilon_0}\int_{-\infty}^{z} dz' \int_{-\infty}^{z'} \rho(z'')dz'' - \frac{z}{\epsilon_0 L}\int_0^L \rho(z')z'dz' \tag{3.6}$$

where ψ is the electrostatic potential and ϵ_0 is the dielectric constant of vacuum. L is the length of simulation box in the bilayer normal direction. Periodic

boundary condition is assumed in the second term, *i.e.* $\psi(0) = \psi(\mathrm{L})$.

3.3.5.6 Cluster Analysis

To characterize the clustering of head groups in lipid bilayers, a distance-based clustering method is adopted. For the pCG model, neighboring lipids that have dummy particles with opposite charges residing within a cutoff distance are considered connected, and all lipids that are connected through dipolar connections are classified as a cluster. Dipolar connections are defined based on contact distance between a positively charged and a negatively charged dummy particle in close contact with each other. The cutoff distance used to determine a dipolar connection is based on pairwise radial distribution functions (RDF) between lipid beads with opposite dummy charges. The position of the RDF first peak, from positively charged CNO dummy beads to all negatively charged particles (CNM, PO4, G1M, G2M) is used to define the cutoff distances. These distances are 3.0Å for CNP-CNM pair (serine-serine), 4.2Å for CNP-PO4 pair (serine-phosphate), 3.5Å for CNP-G1M pair (serine-ester), and 4.5Å for CNP-G2M pair (serine-ester). If either of these distances are satisfied between two lipids, they are considered to be interacting lipids forming a dipolar connection.

The original MARTINI CG model does not have dipolar particles, therefore an additional distance, based on main CG bead sites, are defined to compare pCG and MARTINI model directly. From the defined interacting lipids, pairwise distance

cutoffs of 6.1Å for CNO-CNO pair and 5.5Å for CNO-PO4 pair are defined. These are obtained by including the first peak of respective radial distribution functions (results not shown). Between any two lipids, if both cutoff distances are satisfied, they are considered to be adjacent to each other. An adjacency matrix with $N \times N$ elements, where N is the number of lipids in the system, is introduced to characterize the dipolar connectivity between all lipid pairs, in the following form:

$$\underline{\underline{\mathbf{A}}} = \{a_{ij}\} = \begin{cases} 1 & \text{if } \mathbf{r}_i^{\mathbf{CNO}} - \mathbf{r}_j^{\mathbf{CNO}} \leqslant 6.1\mathring{A} \\ 1 & \text{else if } \mathbf{r}_i^{\mathbf{CNO}} - \mathbf{r}_j^{\mathbf{PO4}} \leqslant 5.5\mathring{A} \\ 0 & \text{otherwise} \end{cases} \tag{3.7}$$

where the superscript for the position vector $\mathbf{r}$ denotes the bead type concerned, the subscript is the lipid index, which is a number assigned from 1 to N. With this matrix, the classification of physically neighboring lipid clusters is transformed to a connected-components labeling problem. The `NetworkX` 1.6 module in `Python` 2.7 is used to perform a connected-components labeling analysis and classify connected lipids in the bilayer as clusters [152].

As for atomistic simulations a cutoff distance of 3.5Å between hydrogen and oxygen atoms is used, which is the typical hydrogen bonding distance [153]. The adjacency matrix for the all-atom data is defined below:

$$\underline{\underline{\mathbf{A}}} = \{a_{ij}\} = \begin{cases} 1 & \text{if } min\{\left\|\mathbf{r}_i^{\mathbf{H}} - \mathbf{r}_j^{\mathbf{O}}\right\|\} \leqslant 3.5\mathring{A} \\ 0 & \text{otherwise} \end{cases} \tag{3.8}$$

The superscript for the position vector $\mathbf{r}$ in Eq.3.8 denotes the atom type (H

for hydrogen and O for oxygen) and the subscript denotes the lipid index. Whenever there is at least one pairwise distance between oxygen and hydrogen in two different lipids that is within 3.5$\mathring{A}$, a hydrogen bond is considered formed between the two.

3.3.5.7 Ion Bridge Connectivity

The first peak of the RDFs between a positively charged ion (Na^+) and other negatively charged beads in a lipid is used to define cutoffs for ion-bead interactions (CNM: 4.4Å, PO4: 6.1Å and G1M/G2M: 5.1Å). In other words, an ion is bound to a lipid if the distance between the positively charged ion and the negatively charged lipid particle is less than the cutoff distance. An ion bridge is formed when one lipid connects to another lipid via an ion-lipid connection.

3.4 Results and Discussion

3.4.1 Structural and Dynamic Membrane Properties

Bilayer Self-Assembly: Snapshots of the bilayer self-assembly process are shown in Figure 3.3 for POPS, and Figure 3.4 for POPC. In both systems, the lipids begin aggregating in less than one nanosecond and form a single disordered aggregate. As system evolves, the aggregate rearranges to form a defect-free bilayer in less than 12 ns.

Area per Lipid and Bilayer Thickness: The bilayer area per lipid at different NaCl concentrations is shown in Figure 3.5. The area per lipid of POPS

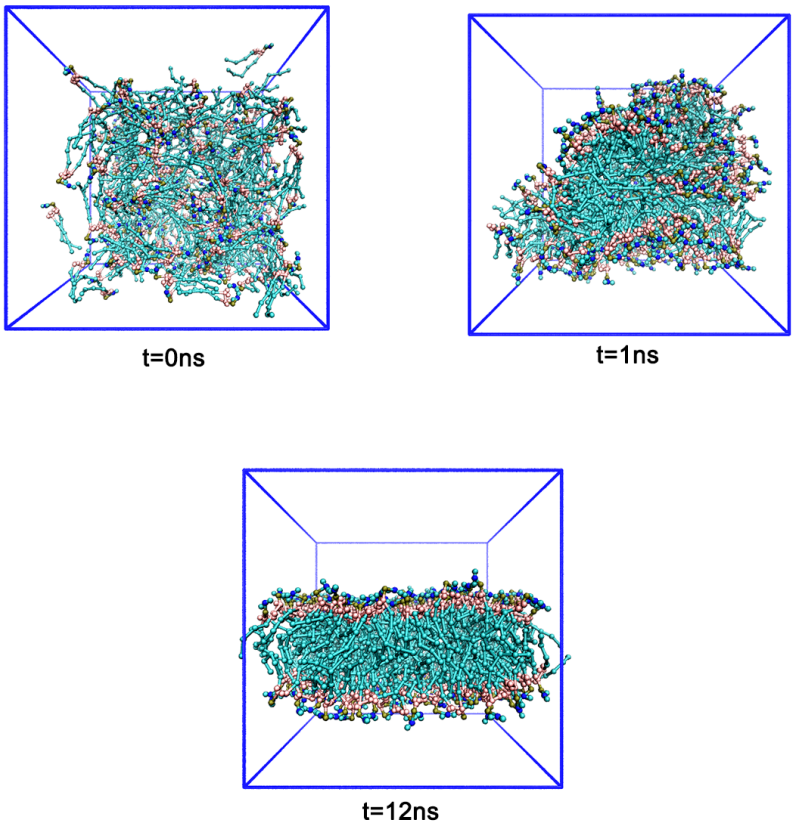

Figure 3.3: Time evolution of bilayer self assembly using pCG (polarizable coarse-grained) POPS. Phosphates are represented in brown, ester groups in pink, serine groups in blue, other groups in cyan.

and POPC at 0M ion concentrations (i.e. with only counterions) is 65Å^2, for both systems with MARTINI force field [1], and 62Å^2 and 60Å^2 respectively with our polarizable model.The standard errors, determined from block averages, are within 10^{-3}nm^2 for all the four systems. One major distinction in our results compared to the MARTINI force field is the ability of our model to capture a difference between the area per lipid of POPC and POPS. Due to the absence of any dipolar inter-

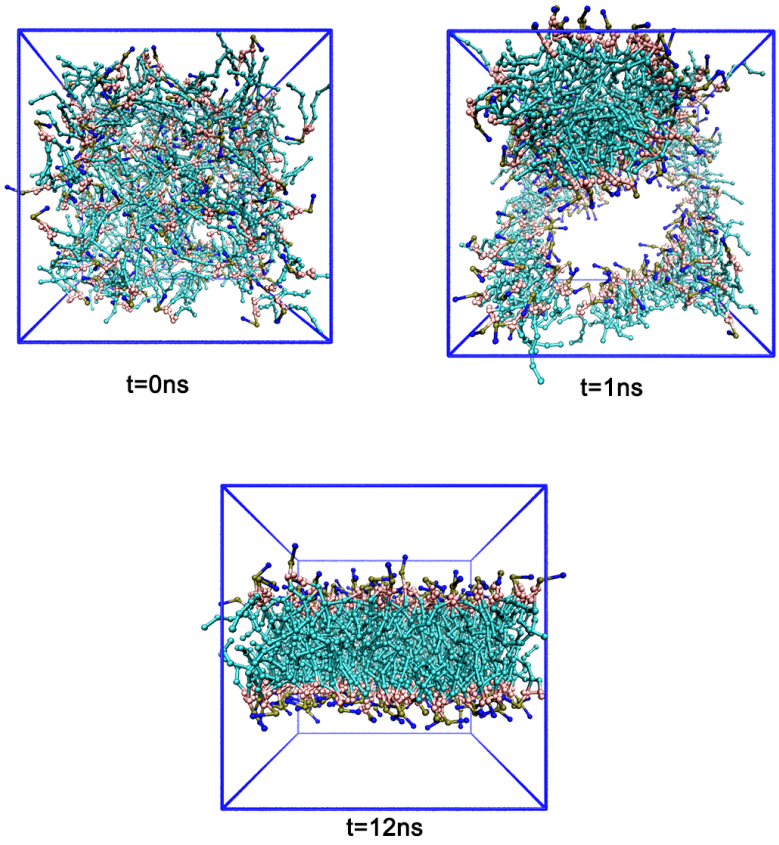

Figure 3.4: Time evolution of bilayer self assembly using pCG POPC. Phosphate beads are represented in brown, ester groups in pink, choline groups are in blue, other groups in POPC in cyan.

actions, the area per lipid values of POPC and POPS bilayer are nearly identical in MARTINI. A condensation effect is observed in pCG POPS bilayer induced by strong dipolar interactions between the serine headgroups. In experiment, the area per lipid of POPS has been reported by different groups to be 45-55Å^2 [154, 155] whereas for POPC it is around 62-68Å^2 [156–159]. Even though our POPC area per lipid (62Å^2) is about 3Å^2 lower than that of MARTINI POPC (65Å^2), both coarse

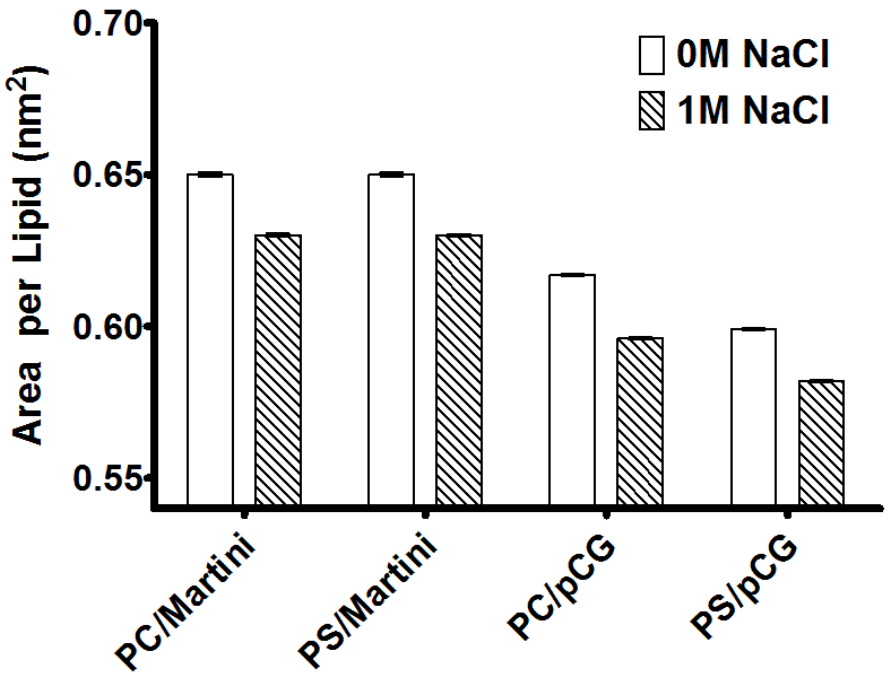

Figure 3.5: Area per lipid change induced by the addition of 1M NaCl. The standard error of mean is within 10^{-3}nm^2.

grained values are within reasonable range, in comparison to both experiments and all-atom simulations [160].

In both MARTINI and our pCG model, the decrease in area per lipid induced by the addition of 1M NaCl is in agreement with previous all-atom simulations [123], and experimental measurements [161] using various lipid bilayers. All-atom study by Pandit et al. characterizing the effect of NaCl on DPPC bilayers, showed that the area per lipid of the bilayer decreases with the presence of ions [127]. The reduction in area per lipid is due to a condensation effect induced by Na^+ ions. On the other hand, Tieleman's study on atomistic POPS with GROMOS, in the presence of ions does not show a marked effect on area per lipid [129]. Our model,

along with MARTINI shows a 3-4% decrease in area per lipid with the presence of monovalent ions, in both POPC and POPS systems.

Table 3.3: Bilayer thickness in different systems evaluated over last 100 ns data

System	Bilayer thickness (Å)	Standard error
POPC (MARTINI)	42.7	0.04
POPC + 1M NaCl (MARTINI)	43.7	0.03
POPS (MARTINI)	41.6	0.04
POPS + 1M NaCl (MARTINI)	43.1	0.03
POPC (pCG)	44.2	0.03
POPC + 1M NaCl (pCG)	44.9	0.03
POPS (pCG)	43.7	0.03
POPS + 1M NaCl (pCG)	44.4	0.03

The average bilayer thickness is listed in Table 3.3 . Bilayer thickness is measured as the distance between vertical positions (z-axis) of phosphate groups on either leaflet. The bilayer thickness of pCG POPS is smaller than that of pCG POPC by ∼0.5Å. In all-atom and experimental studies, the bilayer thickness of POPS is reported to be 38.2 Å and for POPC it is 39.1 Å [125, 156], which shows the same trend. In addition, with the presence of ions, all-atom simulation data with POPC, and POPC-POPS mixed systems, show an increase in bilayer thickness, which is in agreement with our bilayer thickness increase of 0.7Å [50, 161]. The change in

bilayer thickness is attributed to an increase in head group interaction with ions and the decrease of area per lipid.

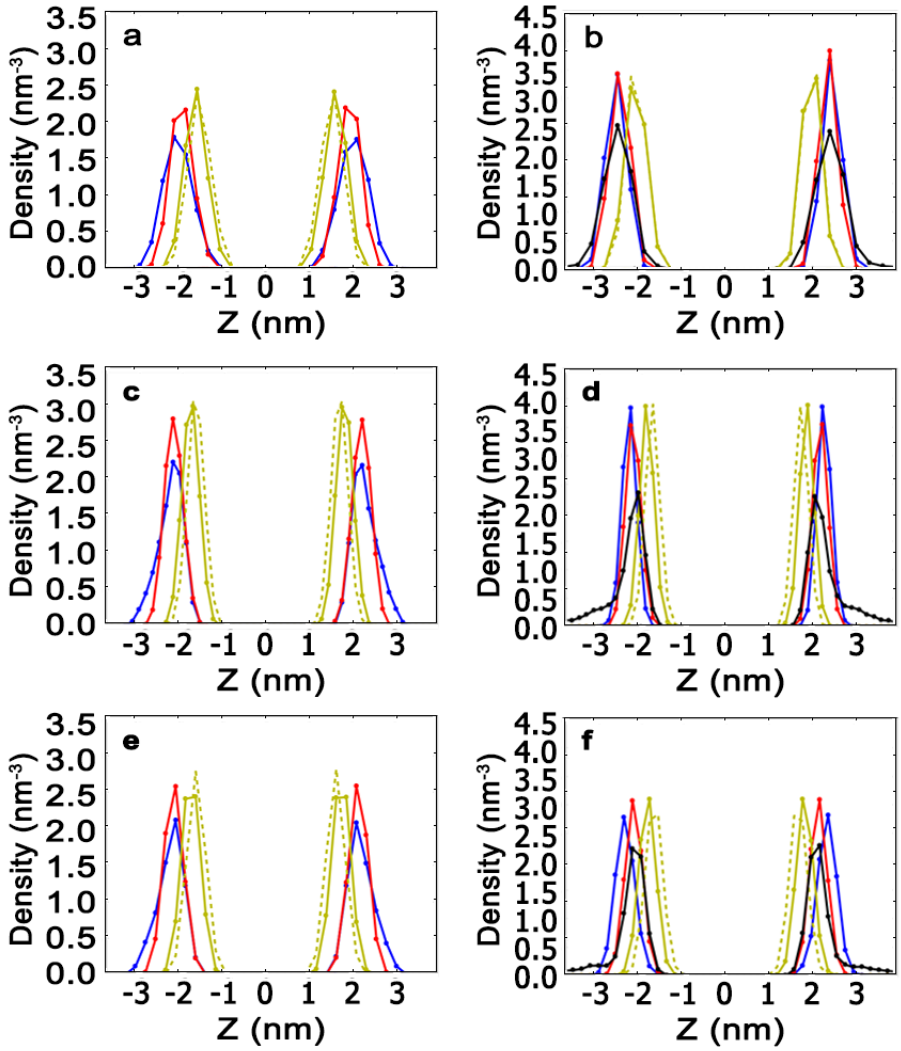

Figure 3.6: Density distribution of (a) POPC from all-atom data, (b) POPS from all-atom data, (c) POPC from pCG data, (d) POPS from pCG data, (e) POPC from MARTINI data, (f) POPS from MARTINI data. Solid yellow: GL1; dashed yellow: GL2; red: PO4; blue: NC3/CNO; black: Na^+.

Density Distribution: Density distributions (see Figure 3.6) of different head groups of POPC and POPS were evaluated to estimate the effect of added

dipolar particles. As shown in Figure 3.6b and Figure 3.6d, the regions occupied by phosphate (PO4) and serine groups (CNO) in POPS overlap in space for our model and all-atom data. This effect is primarily due to the electrostatic interactions among the serine and phosphate groups, between lipids and within lipids, that causes the phosphates to lie in the same vertical position (z-axis) as the serine groups. That is, with the addition of head group dipoles, both the phosphate and serine groups lie on the same plane. However, with the MARTINI force field the serine head group bead is located above the phosphate bead, as seen by the outward shift of the PO4 and CNO distribution peaks (Figure 3.6f). This is due to a lack of any dipole-dipole or electrostatic interactions between CNO-CNO beads and CNO-PO4 beads in MARTINI leading to an increase in conformational freedom of CNO-PO4 beads.

For the 1M NaCl system, both pCG POPS and pCG POPC exhibit Na^+ ion penetration as observed by the increase of the Na^+ density distribution near the head group region (black curve in Figure 3.7a and Figure 3.7b). There is a clear distinction between pCG POPC and pCG POPS, a deeper ion penetration in the PS system is observed. Due to this effect, some of the charges on phosphate beads are satisfied, and the serine bead is seen to interact less with the phosphate group, and more with ions and water. This can be better understood by comparing serine and phosphate positions in Figure 3.7b and Figure 3.6d. By the addition of NaCl the CNO peak shifts outwards, towards the solvent. The ion density curves with both our model and MARTINI (black curve in Figure 3.7a and Figure 3.7b) is similar in location to the Na^+ ion peak with old CHARMM parameters, where Na^+ over

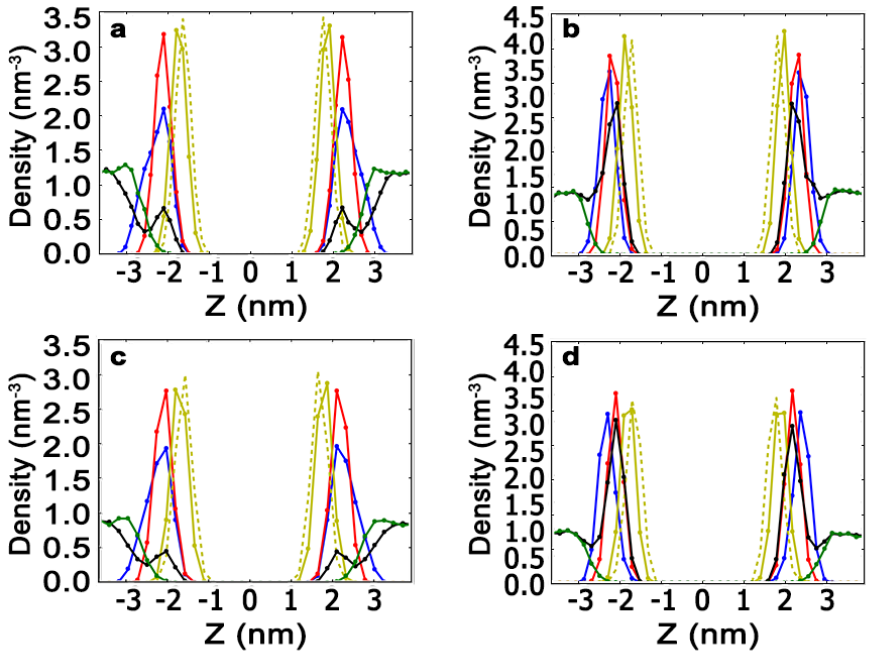

Figure 3.7: Density profiles of lipid bilayer systems with 1M NaCl. Solid brown: GL1; dashed brown: GL2; red: PO4; blue: NC3/CNO; black: Na^+; green: Cl^-. Density distribution of (a) POPC with 1M NaCl from pCG data, (b) POPS from with 1M NaCl from pCG data, (c) POPC with 1M NaCl from MARTINI data, (d) POPS with 1M NaCl from MARTINI data.

binding was observed [162].

Susceptibility Profile and Dielectric Potential: Susceptibility (χ) is a measure of dipole moment sensitivity to changes in external electric field. Both water molecules and head group beads contribute to this dipole moment, and hence χ. Dielectric susceptibility of a bilayer-water system with atomistic force field GROMOS (red curves), our polarizable CG model (black curves) and the MARTINI force field (gray curves) for POPC and POPS is depicted in Figure 3.8a and 3.8b

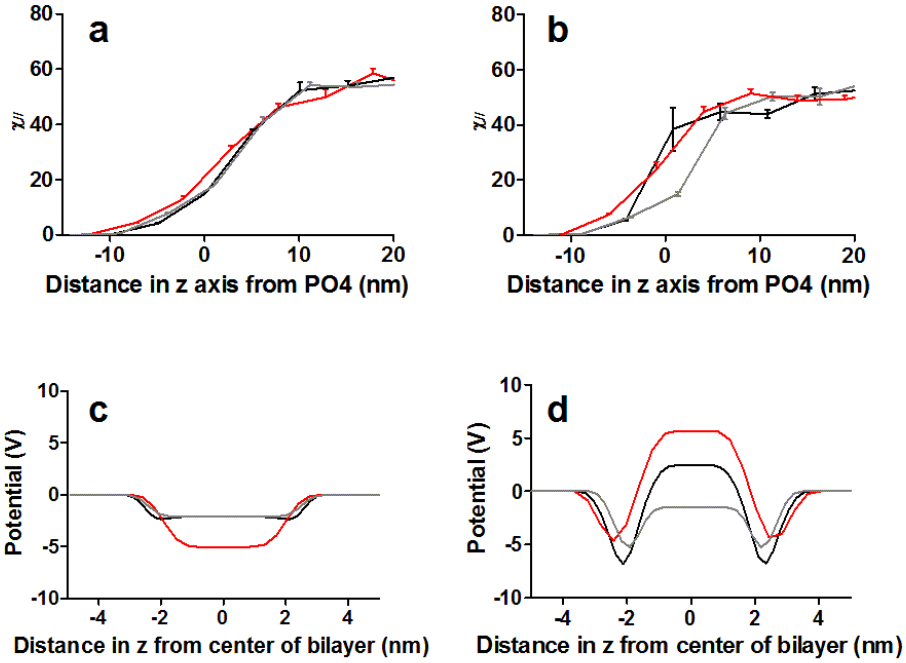

Figure 3.8: Susceptibility profile of (a) POPC and (b) POPS bilayers. Potential profile of (c) POPC and (d) POPS bilayer. Atomistic profile is represented in red, MARTINI in gray and pCG in black.

respectively.

In the case of POPC (Figure 3.8a) there is a gradual gradient in χ from the center of the bilayer (x axis <0) to bulk water (x axis >0). This trend is consistent in all three systems. However, in the case of POPS (Figure 3.8b), the regions near the head groups (interfacial region) have a high dielectric contribution in both all atom simulations (red curve) as well as with pCG (black curve). This effect is not captured in MARTINI (gray curve) largely due to the lack of head group bead polarizability. A CARS (Coherent Anti-Stokes Raman scattering) microscopy experiment used by Cheng et al. show that interfacial water molecules near POPS multilamellar vesicle

is more polarized than those near POPC multilamellar vesicle [163], which can be interpreted as being consistent with our finding that PS interfacial dipoles are more prone to the change of external electric field .

To investigate the effect of bead polarization on membrane electrostatics, we computed transmembrane electrical dipole potential (V) that arises solely from POPC and POPS lipid bilayers, excluding water molecules and ions. Transmembrane potential for POPC and POPS bilayer systems with atomistic force field GROMOS (red curves), our polarizable CG model (black curves) and the MARTINI force field (gray curves) is depicted in Figure 3.8c and 3.8d respectively. This potential largely arises from the alignment of lipid dipole head groups. For the POPC bilayer, the dipole potential evaluated using pCG and MARTINI is nearly indistinguishable, with the exception of a marginal decrease in potential is observed at the interfacial region with pCG, owing to the presence of polarizable ester groups. This result is in disagreement with the observations from Orsi et al., which found that ester groups of PC membranes play a more significant role in electrostatic potential [19].

In the case of POPS, there is a more significant gradient in dipole potential change from the interfacial region to the hydrocarbon core (see Figure 5d, from x=0 to |x|=2), with pCG and all atom bilayers. Although the absolute value of the dipole potential at the center of the bilayer is around +2.5V with pCG, and +5V with the atomistic model, we are able to capture the right trend. That is, MARTINI yields a negative potential at the center of the bilayer, whereas, pCG and atomistic yield a positive potential.

PS Cluster: The presence of lipid clusters in PS and mixed PC/PS bilayers

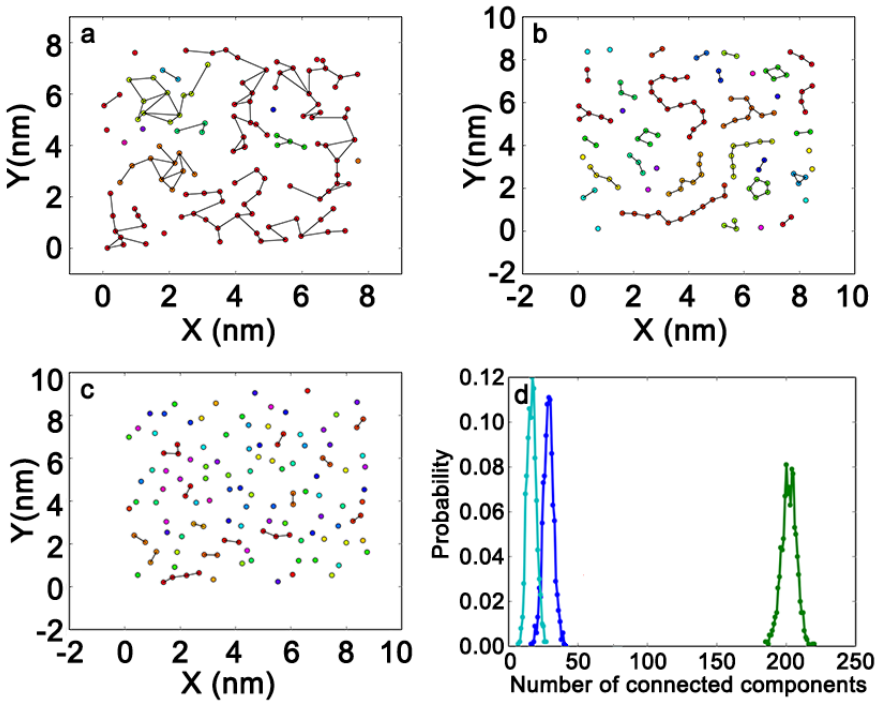

Figure 3.9: Top view of head group clusters for a leaflet (each point represents a phosphate atom, and lines represents lipid connectivity) in (a) all-atom POPS bilayer, (b) pCG POPS bilayer, and (c) MARTINI POPS bilayer. Distinct colors are used to distinguish individual clusters. (d) Probability distribution of number of clusters in POPS bilayer in all-atom (cyan), pCG (blue), and MARTINI (green) systems.

has been observed in the atomistic simulations [50, 129]. Since the head group of POPS in our model is capable of forming dipole-dipole interactions, dynamic clusters are observed on the membrane surface see Figure 3.9b and Figure 3.2b). That is, there are dipolar interactions connecting oppositely charged dummy particles of neighboring lipids. As shown in Figure 6d, on average, there are around 30 clusters in our polarizable lipid CG model, and around 20 clusters in POPS all-atom model. The clusters in our CG model are mostly linear whereas in all-atom simulations they have more branches. This is because, the serine group in the all-atom system can form multiple hydrogen bonds between lipids, while the serine CG bead can only form two dipolar connections. All clusters observed in the simulations are dynamic in nature, they emerge and disappear. Therefore, these dipolar interactions observed in our CG model mimic the hydrogen bonding network observed in all atom bilayers [164] (Figure 3.9a). These clusters are not present in the MARTINI POPS system (Figure 3.9d), due to the inability of the model to capture dipolar interactions. Clearly, pCG is capable of reproducing the essence of cluster formation, which is a distinct property of POPS lipids. The dipoles in polar beads, act as pseudo hydrogen bonds and assist in the interactions between head groups. These head group interactions lead to the formation of clusters. To confirm that our clusters are dynamic, and often break and re-form, we performed a cluster life time analysis (see Supplementary material, section: Dipolar Cluster Half-Life). From our analysis it is clear that the clusters are dynamic, and often exchange lipids.

Line tension: Our model predicts a line tension of 37.3±4 pN for POPC bilayer. This value is within the range of that predicted for similar lipids like DOPC

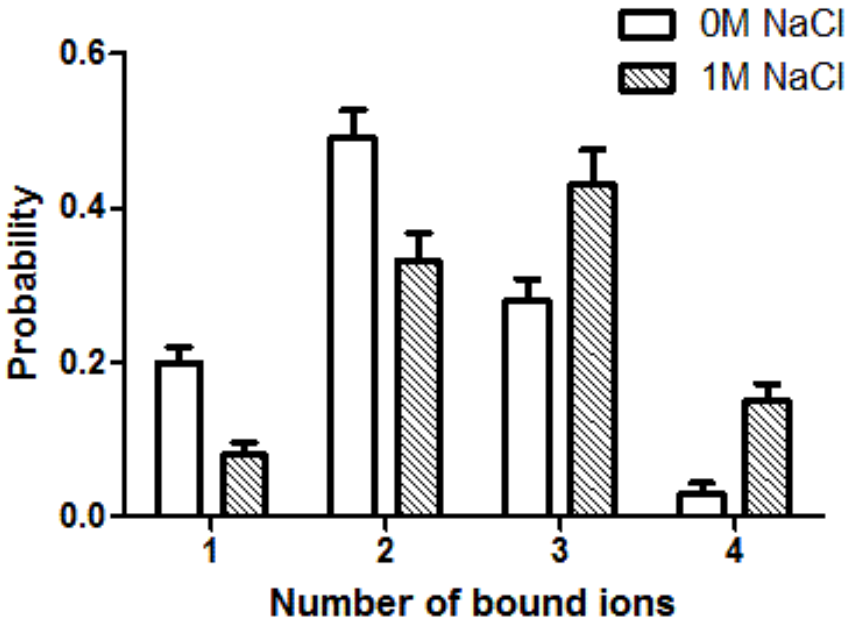

Figure 3.10: Probability of 1,2,3 and 4 ion bridges bound to a POPS lipid at different ion concentrations.

and SOPC (6∼25pN) [151, 165, 166]. Thus the model can capture the right barrier in pore formation of POPC bilayers, and the presence of dipolar particles does not significantly increase this energetic penalty or the barrier for pore formation.The line tension for pCG POPS is 51.7±5 pN. The time scale for edge reconstruction with pCG POPS was significantly higher than that with pCG POPC. The higher line tension with pCG POPS indicates a higher energy barrier for pore formation in lipid bilayers, which is expected due to stronger head group interactions between lipids.

Ion Bridges: To better characterize ion bound-lipids, we classified lipids bound to ions via ion bridges, where an ion bridge is defined as an ion connecting

two lipid molecules based on cut-off distances (see Methods section). For the POPS bilayer system with 0M NaCl (i.e. with counterions), 20% of lipids are bound to only one ion bridge, 49% to two ion bridges, 28% to three ion bridges and almost none of the lipids are bound to four ion bridges (Figure 3.10). However, when 1M NaCl is added to the system, the number of 3 and 4 ion bridges bound to a lipid increases significantly to, 43% and 15% respectively. This suggests that the addition of extra ions to the system connects more lipids, forming larger ion-mediated lipid regions. This result is consistent with many all-atom studies on anionic bilayers [123,129,161].

3.4.2 Membrane-Induced SVS-1 Folding

The presence of dipole particles in lipids (POPS) and peptide (SVS-1) enabled us to better investigate the role of electrostatic interactions. Figure 3.11 includes 4 snapshots of one representative run of SVS-1 peptide with pCG POPS bilayer. Within the first 10 ns, lysine side chains of the peptide (brown) are attracted to the anionic bilayer. Once the side chain charges are satisfied, the dipoles of the backbone beads interact with each other, which aid in formation of a β-hairpin within 30 ns in most trials. The peptide is dynamic on the surface of the bilayer and explores different registers.

This is consistent with experimental behavior of SVS-1, which has been shown to preferentially adopt a β-sheet conformation both in the presence of anionic membranes and tumor cells [38, 144]. To characterize the lateral position of the peptide, we looked at z distance between side chain beads of each of the β strand residue,

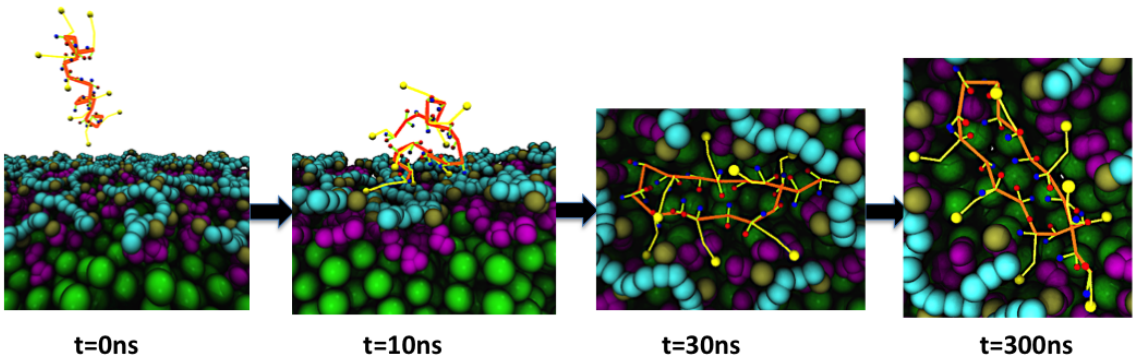

Figure 3.11: Stages in SVS-1 sheet formation: peptide is randomly placed above the bilayer at t=0ns; lysine side chains interact with anionic POPS within a few ns. With lysine side chains buried in the bilayer, the backbone dummies interact to form sheets, which are formed as early as 30 ns in some runs. The peptide is dynamic on the surface of the bilayer and largely retains sheet content by the end of 300 ns. Colors: lipid hydrophobic core (green), peptide backbone (orange), positive and negative dummies in blue and red, phosphates in tan, esters in purple, CNO in cyan and lysines in crimson.

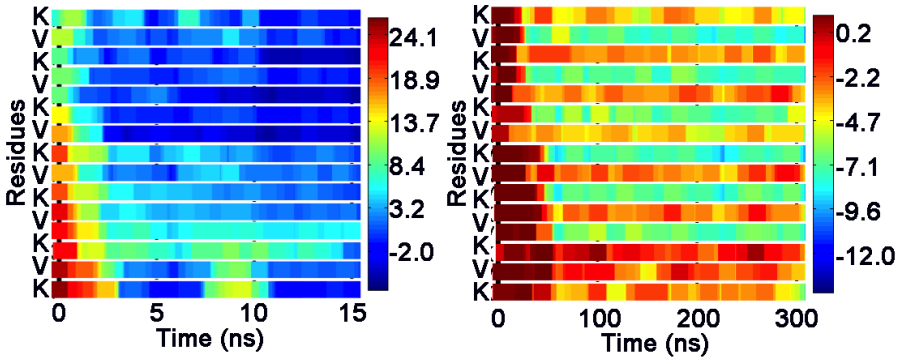

Figure 3.12: Lateral z distance of each side chain bead of SVS-1 strands (residue name on y-axis), from the center of mass of pCG POPS PO4 beads, with time. Color bar represents distance in Å, where negative values indicate deeper side chain penetration, below the com of PO4 layer. (a) and (b) represent different time periods.

and phosphate layer, with time. Figure 3.12 represents this z distance (scale on the color bar) for one representative trial that folds into a β-hairpin. Initially, the lysine distances from the phosphate layer are lower than the valines (dark blue in Figure 3.12a, <2Å), however, with time the valine distances from the phosphate layer become more negative (green and blue, -4 to -7Å). Negative distances in Figure 3.12 denote deeper penetration beneath the phosphate layer . That is, with time the valines face the hydrophobic phase to interact with the alkyl beads, while the lysines continue to interact with the head group region (PO4 and CNO). This leads to a more negative distance for valines than lysines in Figure 3.12.

A total of 9 trials were performed to validate the significance of our results. Details of 3 random trials are shown in Figure 3.13. Figures 3.13a-c depicts in-

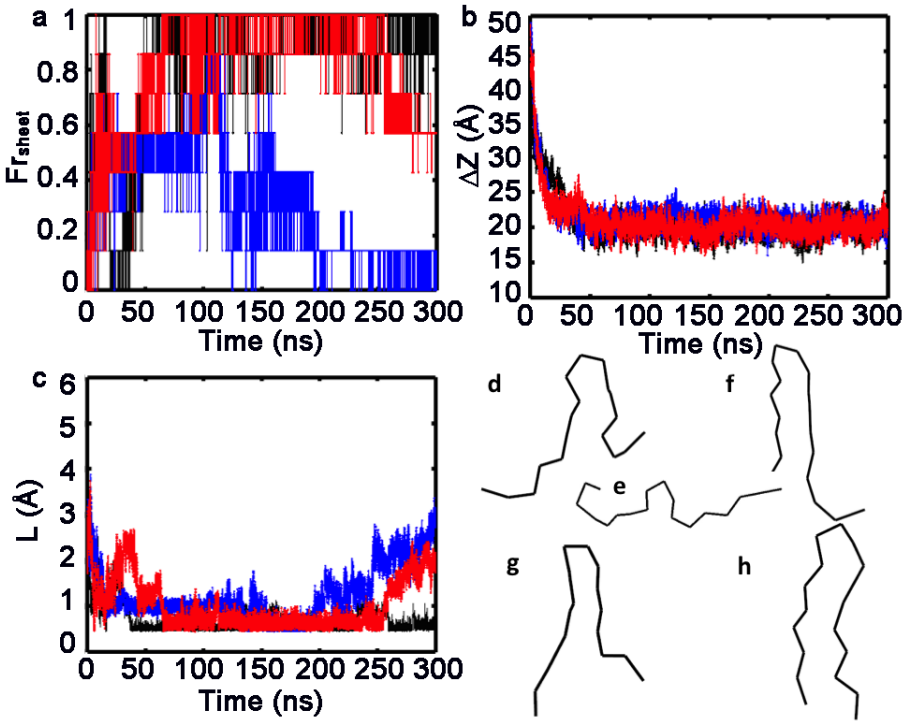

Figure 3.13: Time evolution of (a) sheet pair fraction (Fr_{sheet}) of the peptide; (b) center of mass (com) distance of the peptide from the phosphate beads on the bilayer (Δz); (c) end to end distance (L_c) of the peptide, evaluated between the first and the last backbone bead. Each color represents a single run. Representative snapshots of conformations explored, each with a in-register sheet fraction of (d) 0.28, (e) 0.14, (f) 0.71, (g) 0.57 and (h) 1.0. All data from our polarizable coarse-grained models.

register sheet fraction (Fr_{sheet}) [140], center of mass distance (com) of the peptide from the bilayer (Δz), and end to end distance of the peptide (L_c), respectively. Different colors represent different trials. Another 6 random trials are shown in Figure 3.14. In total, 5 out of 9 runs folded into stable, sheet-like conformations. From Figure 3.13a and 3.13b, as the peptide reaches the bilayer (denoted by 20Å on the y axis), the in-register sheet fraction gradually increases, suggesting the

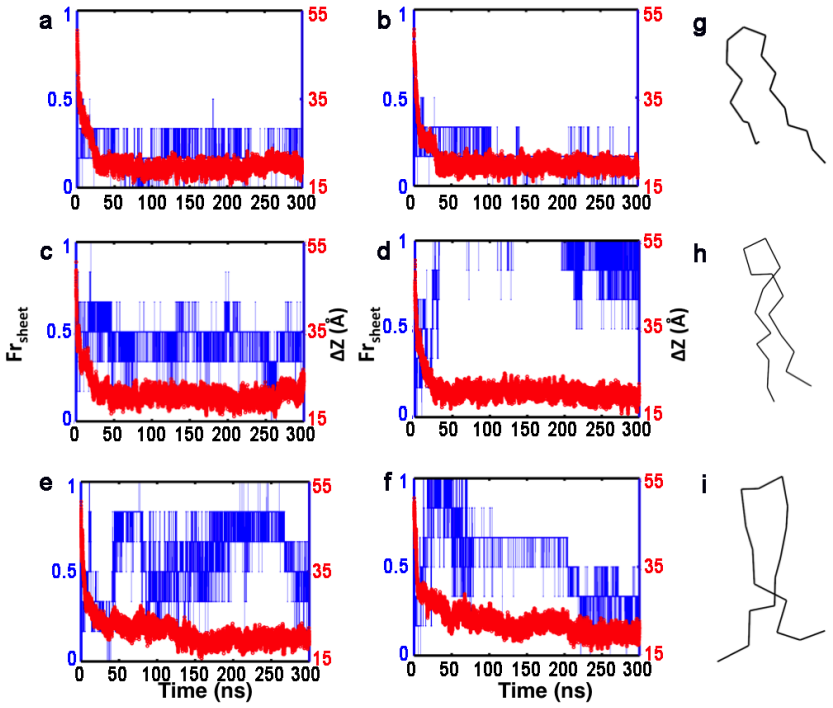

Figure 3.14: Time evolution of sheet pair fraction of the peptide (Fr_{sheet}) in blue and center of mass (com) distance of the peptide from the bilayer in red, for system with pCG POPS. a-f represents individual trials, and g, h and i are final conformations of trials depicted in c, d and e, respectively.

involvement of the bilayer in driving peptide folding. It is important to note that the peptide is dynamic on the bilayer, which can be seen by fluctuations in in-register sheet fraction, which is a strict measurement of sheet contacts. In addition to β-hairpin, off-register conformations are observed, as depicted by the representative peptide conformations with in-register sheet fraction between 0-0.2, 0.2-0.4, 0.4-0.6, 0.6-0.8 and 0.8 to 1 in Figures 3.13e, 3.13d, 3.13g, 3.13f and 3.13h respectively. Conformations with Fr_{sheet} >0.5 are largely sheet-like. Time evolution of L_c of the peptide is shown in Figure 3.13c, a decrease in L_c as the peptide reaches the bilayer and adopts a sheet-like conformation is observed. The trend in L_c correlates with the pair fraction (Figure 3.13a). That is, with an increase in Fr_{sheet} there is a decrease in L_c.

However, not all trials lead to sheet-like conformations (blue curves in Figure 3.13). The peptide is dynamic and folds and unfolds on the surface of the bilayer. For example, in Figure 3.14e there are 27 transitions from folded (Fr_{sheet} >0.7) to the unfolded state (Fr_{sheet} <0.3) in 300ns.

Figure 3.14a-f depict Δz, and Fr_{sheet} of multiple trials. Even though a small double well dihedral bias for both helical and sheet conformations is added to the force field, no helicity was observed for the SVS-1 peptide with pCG POPS at the interface. This is not surprising as the peptide has a distinct sheet pattern of alternating cationic and hydrophobic residues, along with a designated turn region [167].

As control systems, simulations of (a) pCG SVS-1 and pCG POPC bilayer, (b) pCG SVS-1 and POPS bilayer without polarizable particles (POPSnd *i.e.* POPS no-

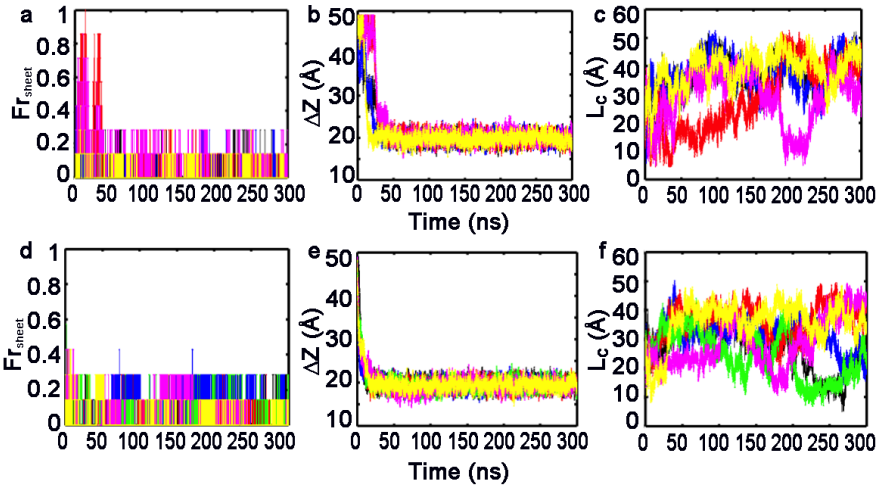

Figure 3.15: Time evolution of (a and d) sheet pair fraction of the peptide (Fr_{sheet}); (b and e) center of mass (com) distance of the peptide from the phosphate beads on the bilayer; (c and f) end to end distance (L_c) of the peptide, evaluated between the first and the last backbone bead. Each color represents a single run. (a), (b) and (c) are data from our polarizable coarse-grained model for POPC bilayer (d), (e) and (f) are data using our peptide model with dipoles and a POPS bilayer without dipole particles (POPSnd).

dipole), and (c) pCG SVS-1 in water were analyzed. Figures 3.12a and 3.12d, 3.12b and 3.12e and 3.12c and 3.12f, depict Fr_{sheet}, Δz, and L_c of runs with pCG SVS-1 and pCG POPC, and pCG SVS-1 and POPSnd (or POPS no dipole), respectively. Each color in the Figures represents an individual trial, a total of 6 distinct runs are represented. Fr_{sheet} explored by these systems is largely below 0.3 and L_c, above 20Å. Therefore, there is a lack of secondary structure content in these systems, and a preference for more extended conformations with L_c ranging from 20 to 50Å (see Figure 3.15c and 3.15f). Any sheet-like conformation explored in the case of

pCG POPC (red and magenta lines in Figure 3.15a) are structures explored by the peptide in water. This is supported by the Δz plot (Figure 3.15b), which shows that the distance between the peptide and the com of the bilayer is greater than 35Å until 30-40 ns. A time-lag in peptide-pCG POPC bilayer binding is observed by comparing the time evolution of Δz in Figures 3.12b, 3.12e, and 3.13b. That is, there is a noticeable time difference of about 10ns between peptide interaction with pCG POPC, in comparison with POPS with and without dipoles. Therefore, the serine dipoles might not play a significant role in attracting the peptide to the bilayer surface.

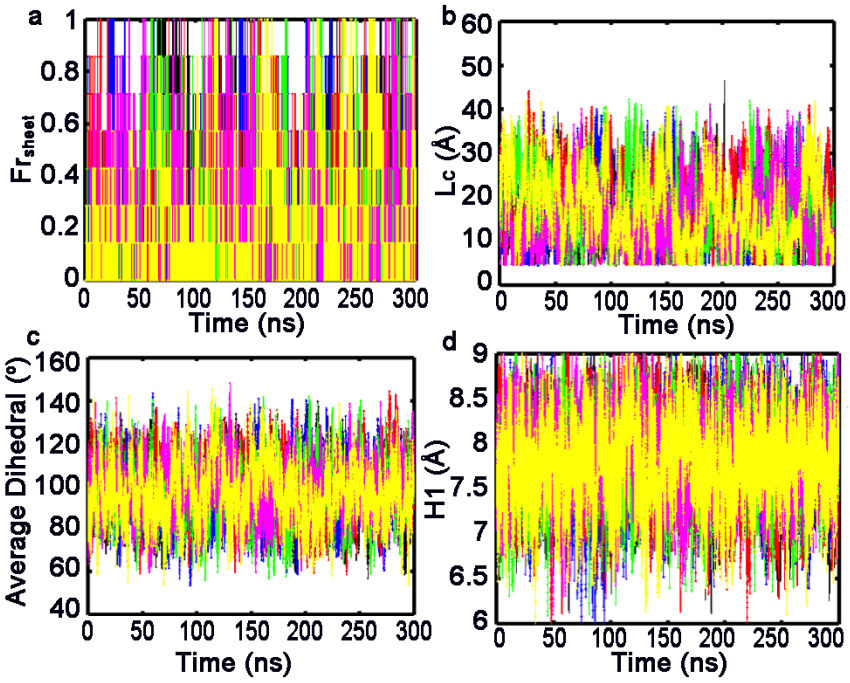

Figure 3.16: Time evolution of (a) sheet fraction (Fr_{sheet}) of the peptide in water, (b) end to end distance (L_c), (c) average dihedral angle per frame and (d) average 1-4 backbone distances (H1). Each color represents a single run.

Time evolution of sheet content, end to end distance, average peptide dihedral,

and H1 distance (i to $i+4$ backbone distance) [140] of pCG SVS-1 in water are shown in Figure 3.16a-d respectively. SVS-1 explores unfolded, helical (average dihedral angle of 40-60° and H1 distance of 5-7Å) and sheet-like conformations (sheet contact greater than 0.7 and L_c within 1-2 nm) without exhibiting a preferred structure or stable state(s) in water. From these four plots, we conclude that SVS-1 is intrinsically disordered in water. This is consistent with both experimental data and the design strategy, *i.e.* SVS-1 was designed to remain disordered and inactive in aqueous solution [38]. In fact, most linear AMPs are not structured in solution, and the induction of secondary structure on membrane surfaces is known to enhance amphipathicity, which plays a key role in the antimicrobial function of these peptides [168]. This also means that the peptide could be collapsed before interacting with the bilayer. However, the fact that a stable β-sheet conformation is observed, only on SVS-1 interaction with pCG POPS and not otherwise, reinforces the role of pCG POPS in stabilizing β-sheet conformations in SVS-1 peptide.

These results, albeit expected, raise a series of important questions, (a) what drives the folding of pCG SVS-1 on pCG POPS bilayers, (b) what is the role of dipoles, both in the peptide and the membrane (c) why does the peptide not fold on pCG POPC and POPSnd (POPS without dipoles) bilayers, and finally, (d) how do the side chains influence the folding process. To answer these questions, we turned to energetic contributions.

Figure 3.17a represents distinct energetic contributions between the CNO beads and the peptide backbone beads (BB) (red curves), phosphate-BB (green curves), GL1-BB (brown), GL2-BB (cyan) and between backbone beads themselves

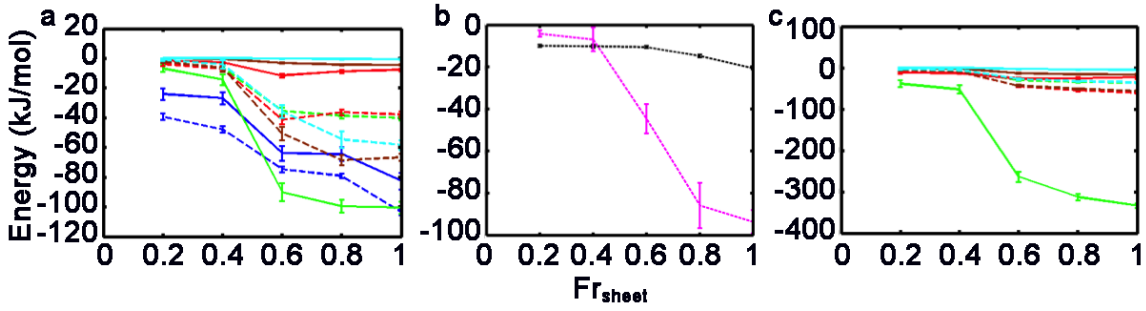

Figure 3.17: LJ pairwise (dashed lines) and Coulombic energies (solid lines) as a function of Fr_{sheet} for (a) PO4-BB (green), CNO-BB(red) and BB-BB (blue), GL2-BB (cyan), GL1-BB (brown); (b) hydrophobic side chain self interaction (black) and hydrophobic side chain-alkyl (magenta); (c) PO4-SC_{C+} (green) and CNO-SC_{C+} (red), GL2-SC_{C+} (cyan), GL1-SC_{C+} (brown). Data from pCG POPS bilayer system.

(blue curves). All five interactions display a swift decrease in energy from the unfolded state (Fr_{sheet} around 0.2) to the folded state (Fr_{sheet}>0.6), thus denoting a cooperative transition in folding. Cooperativity in BB interaction is expected and consistent with our previous study [140], however, the interaction of BB with PO4 and CNO beads also display similar trends. This is because, sheet formation in SVS-1 is not just driven by dipolar contacts within the sheet, but also stabilized by interactions between the bilayer headgroups and the peptide. This result stresses on the relevance of the "polarity profile" of bilayers, or the gradient in electrical polarity due to chemical heterogeneities at membrane interfaces. It has been speculated by White's group, among others, that the chemical heterogeneities of the interface will provide possibilities for non-covalent, stabilizing interactions with pep-

tides [116, 169]. Both GL1-SC_{C+} (brown) and GL2-SC_{C+} (cyan) interactions seem to be the least significant, with LJ interactions (dashed brown and cyan curves) a little more pronounced than Coulombic interactions. This is largely due to the positioning of the peptide in the bilayer, which is below the PO4 layer as evident from Figure 3.12.

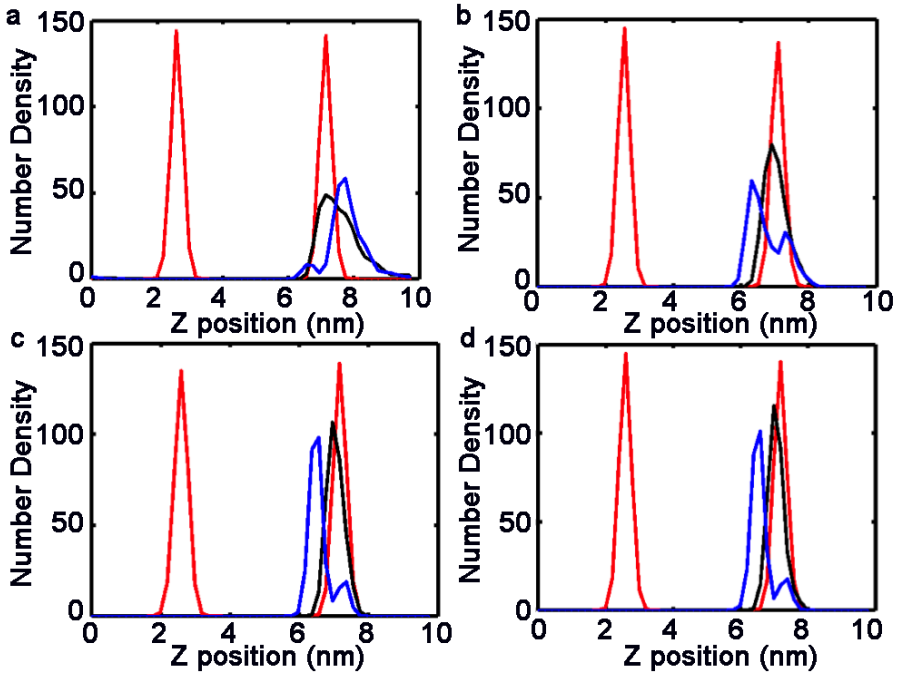

Figure 3.18: Number density distribution of PO4 (red curves), lysine side chain (SC_{C+}) (black curves) and valine side chain beads (blue curves) over a time period of (a) 0-25 ns, (b) 25-50 ns, (c) 50-75 ns and (d) 75-100 ns. Side chain distributions are scaled by a factor of 5 for easy comparison.

Figure 3.17b represents pairwise energies of valine-valine beads (black dashed curve) and valine-lipid alkyl tails (magenta dashed curve). Both these terms show clear cooperative trends of lower energy for the folded state. However, a sharper transition between the folded and unfolded states is observed in the case of valine-

alkyl interactions. To understand the interplay between the lysine (SC_{C+})-phosphate and valine-alkyl interactions, we looked at density distributions of lysine and valine side chains of a representative run (black and blue curves in Figure 3.18, respectively) at different time periods. Density distributions of phosphates on both leaflets (red curves in Figure 3.18) are shown in red, to denote the bilayer boundaries. Figure 3.18 shows the distribution from (a) 0-25 ns, (b) 25-50 ns, (c) 50-75 ns and (d) 75-100 ns. As can be seen from these plots, lysine insertion into the phosphate region is the first crucial step (black curve in Figure 3.18a). With time, the valine side chains flip towards the interior of the bilayer. By 75 ns, almost all the valine side chain beads are completely buried in the hydrophobic region (Figure 3.18c). The results reinforce the importance of amphiphilicity in membrane-induced folding of AMPs.

Figure 3.17c represents distinct energetic contributions between the bilayer and charged lysine side chain beads (SC_{C+}), along the reaction coordinate Fr_{sheet}. Green curves correspond to interaction between phosphate beads and SC_{C+}, red curves correspond to interaction between CNO beads and SC_{C+}, brown curves correspond to interaction between GL1 beads and SC_{C+} and cyan curves correspond to interaction between GL2 beads and SC_{C+}. All solid lines are Coulombic contributions and dashed lines, LJ interactions. Phosphate-SC_{C+} Coulombic interaction (green solid curve) displays a sharp transition from the unfolded state (Fr_{sheet} around 0.2) to the folded state (Fr_{sheet}>0.6). A similar transition of much lower magnitude is observed in the case of CNO-SC_{C+} interaction. Again, both GL1-SC_{C+} (brown) and GL2-SC_{C+} (cyan) interactions seem to be the least significant,

with LJ interactions (dashed brown and cyan curves) a little more pronounced than Coulombic interactions, due to the location of the peptide. Thus, phosphates play a larger role in interaction with cationic side chains. This result can be reconciled with Figure 3.11 and 3.18, where the lysines are seen to drive the peptide towards the bilayer. Positioning of lysine residues to interact with lipid phosphates is a property of many cationic AMPs like CM15, a lysine enriched cecropin-melittin hybrid [170].

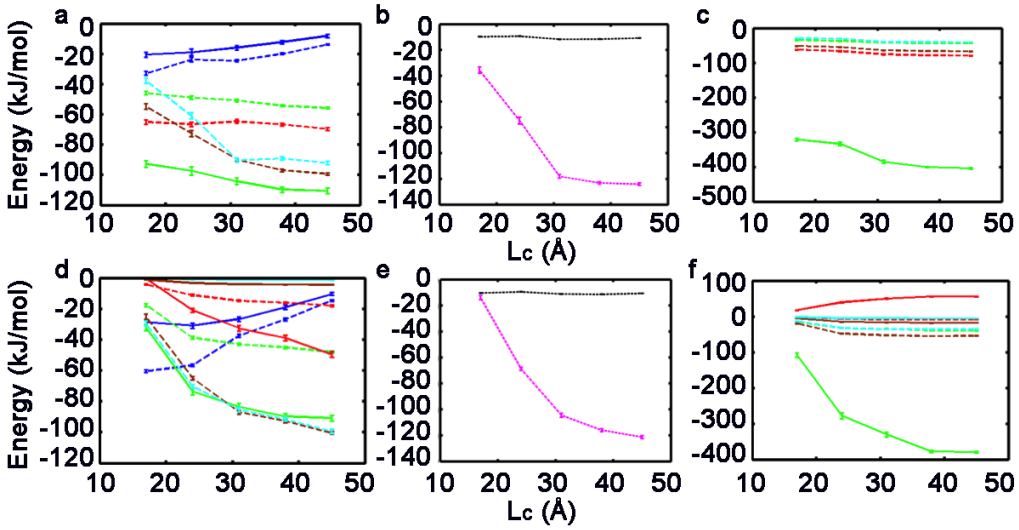

Figure 3.19: LJ pairwise (dashed lines) and Coulombic energies (solid lines) as a function of L_c for (a and d) PO4-BB (green), CNO-BB(red) and BB-BB (blue), GL2-BB (cyan), GL1-BB (brown); (b and e) hydrophobic side chain self interaction (black) and hydrophobic side chain-alkyl (magenta); (c and f) PO4-SC_{C+} (green) and CNO-SC_{C+} (red), GL2-SC_{C+} (cyan), GL1-SC_{C+} (brown). Data for POPS bilayer without dipole particles represented on top (a, b, and c), and pCG POPC bilayer-SVS-1 system below (d, e and f).

SVS-1 does not fold with pCG POPC and POPSnd bilayers, energetic contributions with respect to L_c, of one representative trajectory (brown curves) is

depicted in Figure 3.19. Figures 3.19a-c correspond to POPSnd and Figure 3.19d-f to pCG POPC. Figure 3.19a and 3.19d represent energetic contributions between the head group beads (CNO for POPSnd and NC3 for POPC) and the peptide backbone beads (BB) (red curves), phosphate-BB (green curves), GL1-BB (brown), GL2-BB(cyan) and between backbone beads themselves (blue curves); Figure 3.19b and 3.19e represent pairwise energies of valine-valine beads (black dashed curve) and valine-lipid alkyl tails (magenta dashed curve); and Figure 3.19c and 3.19f, energetic contributions between CNO/NC3 beads and the lysine side chain beads (SC_{C+}) (red curves), phosphate-SC_{C+}(green curves), GL1-SC_{C+} (brown), and GL2-SC_{C+} (cyan). Comparing Figure 3.19 with Figure 3.17, the trend of every curve in Figure 3.17 is reversed in Figure 3.19, except for the blue curves or BB-BB pair interaction. That is, every evaluated pairwise interaction between the peptide and the bilayer in Figure 3.19 favors the unfolded state (L_c>40Å), whereas the same interaction pairs in Figure 3.17, favor the folded state (Fr_{sheet}>0.6). The decrease in BB-BB interaction energy (blue curves) with decrease in L_c is an obvious and expected trend; lower the end-to-end distance, more compact the peptide, higher the intra-peptide interaction and lower the energies.

On comparing Figures 3.19a and 3.19d with Figure 3.17a, we can see that PO4-BB (green curves) interaction energy is lowest in the POPSnd system. This is due to a lack of serine dipoles in the head group region, as dipoles might electrostatically compete with PO4. We can also see that NC3 interacts more strongly with BB beads (red curves in Figure 3.19d), in comparison to CNO in pCG POPS and POPSnd (red curves in Figure 3.17a and Figure 3.19a, respectively), due to its point charge of

+1. Therefore, backbone beads interact more strongly with (a) POPSnd, due to the lack of an electrostatic gradient in the head group region, and hence increased PO4-BB interaction, and (b) pCG POPC, due to higher NC3-BB interaction, along with PO4-BB interaction. Both PO4-BB and NC3/CNO-BB energies in Figure 3.19a and 3.19d (red and green curves), are the lowest for extended peptide conformations on the bilayer surface (L_c>40$\mathring{A}$). This could be because, in both these systems, the dipole or electrostatic interactions within POPSnd bilayer and within pCG POPC bilayer are lower than within pCG POPS. In the case of pCG POPS, the added dipoles facilitate stronger lipid-lipid interactions, which leads to cluster formation (see Figure 3.9). Therefore, in pCG POPS systems, a balance between intra-peptide backbone interaction and peptide backbone-bilayer interaction is achieved. On the other hand, in both pCG POPS and POPSnd systems, the peptide backbone-bilayer interaction is higher, leading to decreased intra-peptide interactions. This suggests that there is a subtle balance between these two competing interactions (intra-peptide and peptide-lipid), which a model must be able to capture, in order to be used to study membrane-induced peptide folding.

From Figure 3.19b, 3.19e and 3.17b, we see that the valine-valine pairwise energies (black dashed curve) are lowest for folded conformations in the pCG POPS system (by -15kJ/mol in Figure 3.17b). However, the valine-alkyl energies (magenta dashed lines) are lower in the case of pCG-POPC (Figure 3.19b) and POPSnd (Figure 3.19b) by about the same amount of -15kJ/mol. Therefore, the net hydrophobic interaction of SVS-1 (intra-peptide and peptide-alkyl tail) does not bias the folded sheet-like state or the unfolded-extended state.

There are two main distinctions between Figures 3.19c, 3.19f and 3.17c. First, the interaction energy between lysine side chains and phosphate beads (green curves) is lowest (around -410kJ/mol) in the POPSnd system (Figures 3.19c), which could be attributed to an absence of electrostatic gradient in the head group region. It is also worthwhile to note that the lowest energy is when the peptide is extended (L_c>40Å). Second, the electrostatic repulsive energy between lysine side chains and choline (NC3) beads of pCG POPC (red curve in Figure 3.19f) destabilizes the membrane-bound state (+80kJ/mol). This repulsion between the head groups of pCG POPC and lysine residues could explain the time-lag in peptide-bilayer interactions seen in Figure 3.15b. However, the longer side chains of lysine residues and its charge distribution on the peptide, facilitates binding to even pCG POPC membranes. In our study, only one peptide is present in the system (Lipid:Peptide is 240:1). With higher concentration of the peptide, repulsive interaction between the peptide side chains (lysines) and pCG POPC is likely to be more pronounced. Binding of cationic β-hairpin AMPs to zwitterionic lipid membranes have been previously observed in protegrin-1(PG-1) known to interact with both zwitterionic and anionic lipids [171, 172]. CMP, the cysteine deleted analog of tachyplesin, is known to bind weakly to zwitterionic POPC vesicles, but remain unfolded [173]. CMP, like SVS-1, folds in the presence of anionic lipids, and is disordered in water. Cationic peptides like TAT [174–177], poly-arginine sequences [178, 179], and penetratin [175, 180] are also known to bind to DOPC and DPPC lipid membranes. Atomistic free energy studies with OPLS forcefield predicts lysine and arginine residues to have favorable interfacial free energies of partition with DOPC bilayers [181]. It is also

important to remember that the SVS-1 peptide used in this study is mapped to our minimalistic CG model, where we have only one type of hydrophobic and charged residue. Therefore, valine and lysine residues in our simulation study essentially represent a hydrophobic and charged residue prototype and not the properties of the residue themselves.

Finally, the trend in Coulombic interaction of GL1 and GL2, both with lysines and phosphates in (a) pCG POPC is minimal and almost non existent (brown and cyan solid curves in Figure 3.19d and 3.19f), and (b) absent in POPSnd. Although the LJ interactions of GL1 and GL2 show a decrease in energy values with increase in L_c, similar to most other peptide-lipid interactions(brown and cyan dashed curves in Figure 3.19d and 3.19f), this is largely because of the location of the peptide within the bilayer.

3.5 Conclusion

We have explored the role of lipid head group dipoles in structural and dynamical properties of an anionic (POPS) and zwitterionic (POPC) bilayer. We have done this by introducing polarization into polar coarse-grained lipid head group. The model has roots in the MARTINI force field and has been built to be compatible with our recently developed protein model that captures *de novo* folding of secondary and supersecondary protein structures [140]. Our model is slightly more expensive in computational cost. In simulations of the benchmark system with 240 POPC lipids and 7757 CG water molecules, our model is slowed down approximately

by a factor of two in comparison with the MARTINI system, which mostly arises from the shorter time step in our model. Several interactions involving polarizable CG beads have been re-parametrized. It should also be noted that, we have not tested all the bead types of the MARTINI force field, and our lipid model is not transferable to the other lipid types, because it is intended to be used specifically with our peptide model to study membrane-induced peptide folding.

The physical properties of the POPS and POPC bilayers which formed spontaneously from a random configuration, exhibit reasonable descriptions of lipid behavior. To examine the performance of our model, we explored structural, dynamic and electrostatic properties, such as the cross-bilayer density profile, area per lipid, bilayer thickness, mean squared displacements, line tension, dipole potential, dielectric profile, head group orientation and formation of lipid clusters. Comparison of these properties with experiments and/or all-atom simulations shows good agreement. Our model also captures the right trend in membrane interface electrical potential, which the MARTINI model fails to capture.

The model predicts formation of lipid clusters in PS bilayers in agreement to all-atom simulations, but in contrast to the the MARTINI model. In particular, we have shown that dipole interactions are crucial in stabilizing lipid cluster formation in PS bilayers by mimicking the hydrogen bonding network present in the head group region of atomistic PS bilayers. The presence of PS lipid cluster formation causes a distinction in area per lipid between POPC and POPS bilayer in our model. That is, the presence of head group dipoles in POPS results in a condensation effect by the alignment of headgroup dipoles, which manifests as a decrease in area per

lipid. In addition, the model indicates, in agreement with all-atom data, that the serine group lies at the same vertical position of the phosphate group. This is in contrast to the MARTINI model where the serine is found above the phosphate position. Also, more subtle changes to head groups, on interaction with monovalent ions are observed. With the addition of 1M NaCl, area per lipid of both POPS and POPC bilayers decreased due to an electrostatic condensation effect, and the average number of ion bridges formed between lipids increased. We are currently working on parameterizing ions and charged interactions based on size to charge ratio. In this model, all ions are considered as hydrated ions, with decrease in ion radius, there is also a change in the size of its hydration shell, thus by making this distinction we will be able to distinguish different types of monovalent ions.

We studied POPS mediated folding of anticancer peptide SVS-1 to explore the effects of lipid head group interactions in membrane-induced peptide folding. With pCG, we were able to observe membrane mediated folding of SVS-1 into β-hairpin with anionic bilayers, in agreement with experimental observations. The driving forces involved in folding include PO4-lysine interaction, valine-alkyl interaction, intra-peptide interaction and CNO-peptide interaction. PO4-lysine interaction contributes in attracting the peptide to the anionic bilayer, while valine-alkyl interaction and intra-peptide interaction play a role in stabilizing the β-turn conformation. We do not observe SVS-1 folding with pCG POPC, POPSnd, or in water, where it is intrinsically disordered. This is in agreement with experimental studies [38].

One of the reasons we observe SVS-1 folding in pCG POPS bilayers, and not pCG POPC or POPSnd is because, a subtle balance between intra-peptide

interaction (BB-BB) and peptide-lipid bilayer (BB-PO4 and BB-CNO) interaction is achieved only with pCG POPS. In the case of pCG POPC and POPSnd, the peptide-lipid interactions are more stronger (BB-PO4 in POPSnd and, BB-PO4 along with BB-NC3 in pCG POPC), thus decreasing intra-peptide interactions (BB-BB). The presence of added dipole particles in the CNO or serine head group region in pCG POPS, leads to higher lipid-lipid interaction, which is also the primary reason for head-group mediated lipid clusters observed in these bilayers. This causes lower lipid-peptide interactions and subsequently, higher intra-peptide interactions. Whereas, both in the case of POPSnd and pCG POPC, there is less (if any) dipole-dipole interaction between lipids in a bilayer, which leads to increased peptide-lipid interaction and hence decreased intra-peptide interaction. This is also the reason clusters are not formed with MARTINI force field or in pCG POPC bilayers. The role played by the ester groups (GL1 and GL2) in all three systems (pCG POPS, pCG POPC, POPSnd) is minimal for SVS-1 peptide. There is also a lag in peptide-bilayer interaction for pCG POPC system, due to electrostatic repulsion between lysine residues and positively charged choline beads. In conclusion, our results also suggest that there is an intricate balance between intra-peptide, peptide-lipid and lipid-lipid dipole interactions, which our CG model captures.

Chapter 4: Influence of Monovalent Cation Size on Nanodomain Formation in Anionic-Zwitterionic Mixed Bilayers

4.1 Overview

This chapter is based on the author's publication: Influence of Monovalent Cation Size on Nanodomain Formation in Anionic-Zwitterionic Mixed Bilayers. Sai J. Ganesan, Hongcheng Xu* and Silvina Matysiak. Journal of Physical Chemistry B, 2016. (* co-author)*

Phosphatidylserine (PS) and phosphatidylcholine (PC) are two of the major anionic and zwitterionic phospholipids in mammalian cell membranes. Ion-PS interaction is hypothesized to play a crucial role in a range of biological events including membrane fusion, lipid phase modulation, membrane protein insertion and translocation. In this study, we characterize using coarse-grained simulations, lipid nanodomain formation in PC/PS mixed bilayers. We investigate the effect of monovalent cation sizes in modulating lipid-ion binding modes and lipid demixing. Our simulations suggest that certain lipid-ion binding modes lead to growth of ion-mediated PS lipid clusters. The existing literature reveals the polymorphism in

binding and partitioning patterns in monovalent cations (Na^+, K^+ and Li^+) with anionic lipids. This chapter provides a microscopic view on the ion size-dependent PS lipid packing pattern as observed experimentally. A coupled relationship between lipid curvature and asymmetry is observed in highly demixed PC/PS mixed bilayers.

4.2 Introduction

Cellular membranes are not homogeneous in nature and are composed of a multitude of lipids and proteins. Some of the interactions between lipids are more favorable than others. These interactions give rise to many interesting patterns with distinct physical and biological properties, producing regions of order and disorder in cellular membranes [182]. Some regions on the bilayer are thicker, while other regions are thinner. There are also regions that are more or less crowded than others. Different cells have membranes with unique lipid compositions. The structure of these membranes is constantly regulated [182]. There is significant evidence that suggests cellular membranes are composed of different fluid-fluid phase-separated lipid microdomains, which play a role in protein diffusion and functions [183,184]. Questions regarding membrane organization [185, 186], remodeling, and microdomain formation [187], are still a subject of discussion and interest in the field.

Lipid phase regulation by cholesterol is well studied both experimentally and computationally. Cholesterol is known to associate with saturated lipids to form liquid-ordered (L_o) domains and induce domain formation in lipid mixtures [134,

188–190]. The nature of phase separation in cholesterol-containing ternary mixtures is attributed to a tail-induced ordering effect [191]. However, the formation of domains induced by metal ions is much less explored.

The role of metal ion (M^+) binding to biological membranes is of interest as it affects structure, dynamics, and stability of lipids which in turn affect folding, binding and insertion of proteins. Ion interaction with phospholipids is driven mainly by Coulombic forces near the headgroup region and is therefore more pronounced for anionic lipids [192]. Both the structure and behavior of membranes are dependent on ion type and strength. Among monovalent metal ions of biological significance (such as K^+, Na^+ and Li^+), K^+ and Na^+ are known to produce only minor changes in bilayer structure, stability and chain packing [44]. In sharp contrast to this, even at low concentrations, Li^+ is known to influence the lipid state of phosphatidylserine (PS) by increasing its melting temperature, thus inducing the transition from a liquid-disordered state to a gel state [44, 45, 47]. Li^+, similar to divalent cations Mg^{2+} and Ca^{2+}, is known to form dehydrated ion-PS complexes [48]. An infrared study by Hauser's group suggests that Li^+ binds to the phosphate and carboxylate groups of DMPS lipid (1,2-dimyristoyl-*sn*-glycero-3-phospho-L-serine), resulting in both lipid headgroup dehydration and ordered packing; while Ca^{2+} binds deeper into the phosphate and ester region [47]. The similarity between Li^+ and Ca^{2+}, and their distinction from other monovalent ions has been hypothesized to be a result of binding modes [193]. From the interpretation of deuterium NMR studies, divalent cations Ca^{2+} and Mg^{2+} were hypothesized to be more deeply buried in POPS (1-palmitoyl-2-oleoyl-*sn*-glycero-3-phospho-L-serine) membranes than monovalent ions K^+ and

Na^+, whereas Li^+ was hypothesized to be an intermediate between the two [193]. A recent study using SANS, SAXS and molecular dynamics (MD) simulations with CHARMM and GROMOS force fields from Tieleman's group found Na^+ ions to interact most strongly with the carboxylic oxygen of the serine group, followed by the phosphate oxygen, with very minimal interaction to ester groups in POPS bilayers [125]. However, there exists some discrepancy in Na^+-PS and K^+-PS interactions based on MD force fields. For example, a study using GROMOS force field and mixed bilayers of POPC (1-palmitoyl-2-oleoyl-*sn*-glycero-3-phosphocholine) and POPS lipids found both K^+ and Na^+ to interact with carbonyl ester groups of POPS lipids, with an increased affinity for Na^+ [50]. Another study using DMPS lipids and GROMOS87 force field found Na^+ to bind to serine carboxyl and phosphate groups as opposed to ester carbonyl groups [51]. Another study using AMBER forcefield for DOPC lipids [52] and a set of specialized parameters for Na^+ and K^+ [53], found the ions to interact preferentially with the phosphate region [54]. These discrepancies are well known in the community, and is one of the aims of the open science collaboration project, the NMRlipids project [194]. Although there exists a difference in ion-lipid binding modes for different monovalent ions of varying sizes, but the question remains how ion binding modes affect structural, mechanical and dynamic properties of lipid membranes.

Atomistic polarizable lipid forcefileds are also being developed to better characterize electrostatic interactions. From simulations with aqueous ions in polarizable forcefields, the polarization increases the surface affinity of halide anions [195, 196]. Also, the aqueous ion simulations with polarizable forcefields capture the thermody-

namics of ion solvation differently from nonpolarizable forcefields [197]. The conventional forcefields without polarization fix the atomic partial charges, which means the parameters must be used in a similar environment as they were parameterized. Therefore, nonpolarizable parameters suitable for bulk water may not be transferable for other environments. In contrast, polarizable forcefields are more transferable as they capture the induced polarization in the molecule [198]. The role of polarization has been shown to be critical in ion channel studies [199–201], and atomistic polarizable forcefields also improve DPPC bilayer and monolayer properties [202].

A lipid bilayer exhibits a highly heterogeneous environment, which makes microscopic experimental studies of lipid-ion interactions challenging. On the other hand, molecular simulations can provide a mechanistic view of macroscopic experimental observables. There are multiple coarse-grained (CG) models that have shed light on membrane molecular processes including cholesterol- or tail-induced phase separation in lipid mixtures [1,135–139,190]. To our knowledge most CG simulations on lipid domain formation in mixtures are due to tail ordering, and there are also other studies on the effect of pH on lipid charge, shape and interactions [203, 204]. Previous studies have observed an intrinsic tendency for POPC/POPS lipid mixtures to demix in its fluid state [205,206]. A Monte-Carlo (MC) simulation based on a two dimensional triangular binary lipid lattice model, with a non-electrostatic excess mixing energy was used to show the formation of PC-PS domains as a function of mixing energy [207]. This MC study did not have ions or electrostatic interactions in the system. Our study is one of the first to characterize domain formation in lipid mixtures, driven by headgroup interactions with explicit solvent and ions.

Interactions of cations with membranes are relevant due to the prevalence of ions in a biological environment. Phosphatidylserine (PS) and phosphatidylcholine (PC) are among the major anionic and zwitterionic phospholipids of neural tissues [208]. Therefore, understanding the size effect of monovalent cations in modulating structural and dynamic properties of PC-PS mixtures could provide valuable information regarding many biological processes.

In this chapter, we adopted the Water Explicit Polarizable Membrane Model (WEPMEM) [209] as described in Chapter 3 to characterize the effect of monovalent ion size on 1:1 POPC-POPS lipid mixtures. WEPMEM has roots in the MARTINI force field, and is combined with Yesylevskyy's polarizable water model [90]. In WEPMEM, structural polarization is added to certain polar groups in order to capture potential head group dipole interactions in lipid bilayers (See Figure 3.1). In each polar CG bead, a flexible dipole is used to characterize the underlying changes in dipole orientation present in the lipid head group region. The dipole is made flexible by adding angular constraints between bonds of oppositely charged dummy or dipolar particles, which are attached to the center of mass site. Dipolar particles interact with other beads through electrostatic interactions or the Coulombic potential, which allows our model to exhibit induced polarizability. We currently have modeled parameters for POPC and POPS. All beads in WEPMEM have the same size of 4.7Å (1.0σ), and the ions are modeled as hydrated ions. With the decrease in ion size, the number of hydrated water molecules near ions change as well [210]. From literature, the radius the first hydration shell for Li^+ is 3.1Å, for Na^+ is 3.5Å and for K^+ 3.7Å [210]. Therefore, we can model different monovalent

cation types by decreasing the size of the CG ion bead. With this study, we aim to predict the behavior of adding salt, with monovalent cations of different sizes, on 1:1 POPC/POPS mixed lipid bilayers. We also investigate if there is a particular ion size range at which the ion-mediated, headgroup-driven lipid demixing exhibits phase coarsening. This study, to our knowledge is the first CG MD study to describe ion-mediated, lipid headgroup-driven nanodomain formation in POPC-POPS lipid mixtures.

4.3 Methods

4.3.1 System Setup and Analysis

Bilayer systems are built with our new model WEPMEM, which was described in the Methods section in Chapter 3. To study the effect of M^+ (monovalent cation) sizes, bilayers with a total of 240 POPC and POPS lipids with a ratio of 1:1 were constructed. The initial bilayer is symmetric, with equal number and composition of lipids randomly distributed on each leaflet. Four distinct M^+ sizes were explored in this study, starting from 1.0σ, which is the size of all beads used in the model, to 0.9σ, 0.8σ and 0.7σ. All ions in WEPMEM were modeled as hydrated ions. With the decrease in monovalent cation size from K^+ to Li^+, there is a corresponding decrease in the hydration shell radius [210]. Consequently, we can model the decrease in the monovalent cation hydration shell radius by decreasing the size of CG cation beads in our model. All ions were placed in the solvent at time 0ns. A salt concentration of 0.4M in the aqueous environment was used consistently throughout this study

Table 4.1: Details of system setup.

Box size at t=0ns	Lipids	Water	M^+	X^-
18nm x 18nm x 11nm	960	15088	950	470
9nm x 9nm x 11nm	240	4127	240	120

unless stated otherwise. Simulation data for 500ns in NPT ensemble was collected and the last 100ns data was analyzed unless stated otherwise. A corresponding amount of anions (X^-) with the size of 1.0σ was consistently used throughout the study. To evaluate the effect of ion concentration, 0M (only counterions) and 0.2M concentrations was used with monovalent cation (M^+) size 0.8σ. Although the concentration of 0.4M is very high and not comparable to physiological conditions, we are interested in understanding changes in ion binding modes, which should not be affected by the concentration used in the study. Details on system size, number of positive and negative ions, water, and lipid molecules are listed in Table 4.1.

To account for finite size effects, we simulated a randomly constructed 960-lipid symmetric bilayer with 1:1 ratio of POPC and POPS lipids, with all the ions in solvent at time 0ns. Two different ion sizes, 1.0σ and 0.8σ were explored for this system. $1\mu s$ simulation data was collected in NPT ensemble. To account for time scale effects, we simulated a phase-separated 960-lipid symmetric bilayer with 1:1 ratio of POPC and POPS lipids. All ions are in solvent at time 0ns. Four different cation sizes, 1.0σ, 0.9σ, 0.8σ and 0.7σ were explored with this pre-phase separated bilayer system. 1-$2\mu s$ simulation data was collected in the NPT ensemble after 100ns

of NPT equilibration by position restraining the lipids. For details on simulation and force field parameters, please refer to the Methods section in Chapter 3.

To characterize ion-mediated anionic lipid clusters, we used two different clustering methods. The first method is based on ion-lipid interaction cutoff distances. Neighboring anionic lipids that are connected via a cation (ION), within either a cutoff distance between (a) phosphate bead (PO4)-ION of 5.5Å or (b) negative dummy particle of serine bead (CNM)-ION of 2.0Å, were classified as a cluster. These cutoff distances are obtained from PO4-ION and CNM-ION RDF (radial distribution function) peaks for 0.8σ M^+. The number of lipids in the largest cluster formed in each frame is used to quantify the growth of cluster over time. Connected-components labeling analysis was performed using `NetworkX` 1.11 module in `Python` 2.7 to classify all connected lipids as clusters [152]. The second clustering method is based on lipid adjacency in the bilayer 2D Voronoi diagram. We firstly mapped the positions of all the lipids (including zwitterionic and anionic lipids) to a Voronoi diagram. If one or more anionic lipids are fully surrounded by other anionic lipids, then the surrounded lipid and all the neighboring lipids are defined as connected. Once the connections in all anionic lipids were defined, we then used the connected-components labeling analysis, as described above to classify the connected anionic lipids as clusters.

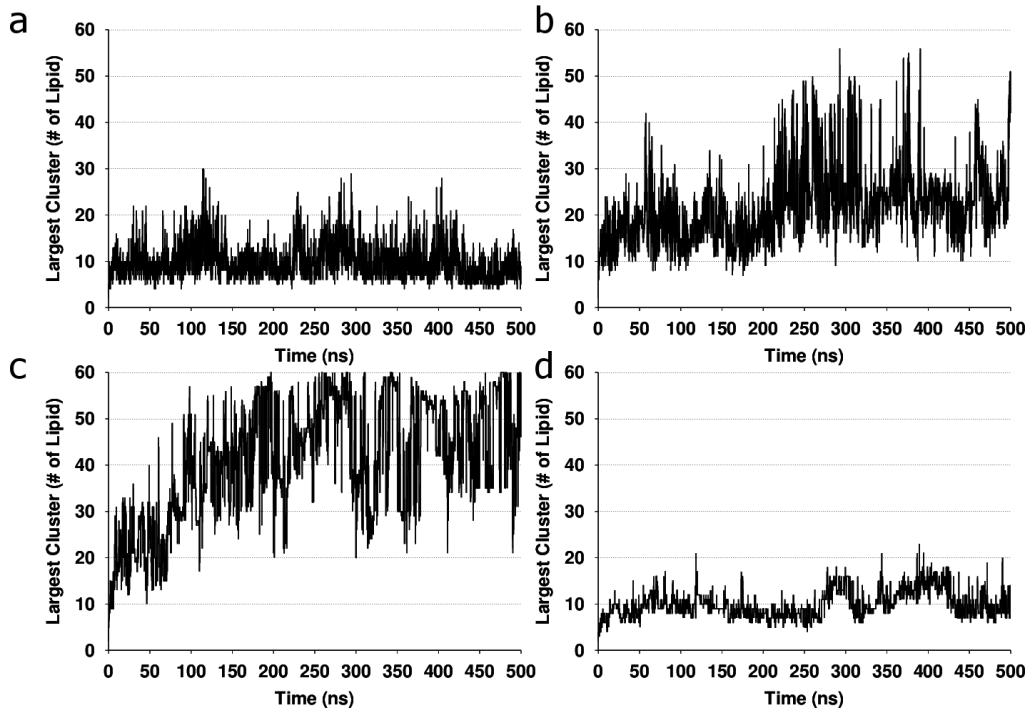

Figure 4.1: Effect of 0.4M M^+ ion size on 240 lipid 1:1 POPC/POPS lipid bilayer. (a-d) Cluster time evolution of POPS lipid clusters with 1.0σ, 0.9σ, 0.8σ and 0.7σ ions respectively. Data obtained from the clustering method based on ion-lipid interaction cutoff distances.

4.4 Results and Discussions

4.4.1 Effect of Monovalent Ion Size on PC-PS Mixtures

4.4.1.1 Lipid Cluster Formation

Figure 4.1 shows the time evolutions of the largest POPS cluster size for systems with 1.0σ, 0.9σ, 0.8σ and 0.7σ M^+ ions respectively, using the clustering method based on ion-lipid cutoff distances. When we compare Figures 4.1b and

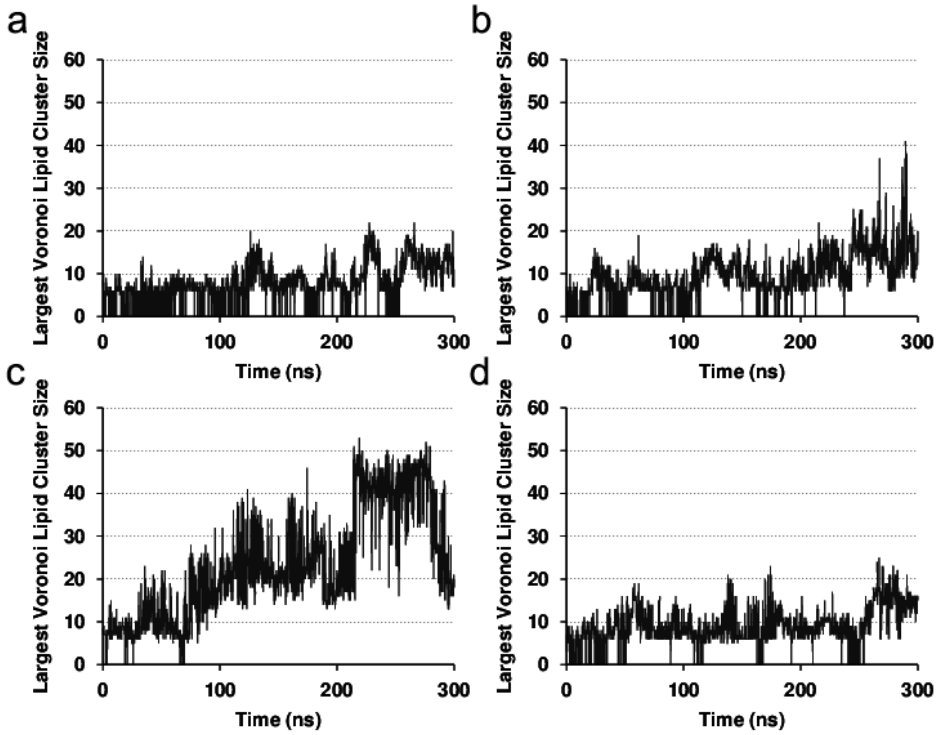

Figure 4.2: Effect of 0.4M M^+ ion size on 240 lipid 1:1 POPC/POPS lipid bilayer. (a-d) Cluster time evolution of POPS lipid clusters with 1.0σ, 0.9σ, 0.8σ and 0.7σ cations respectively. Data obtained from clustering method based on bilayer 2D Voronoi diagrams.

4.1c to other subfigures (Figures 4.1a and 4.1d), an increase in POPS largest POPS cluster size is observed for systems with both 0.9σ M^+ ions and 0.8σ M^+ ions, which suggests the growth of anionic lipid clusters with both ion sizes. On the other hand, the sizes of the largest POPS cluster with 1.0σ M^+ and 0.7σ M^+ ions do not grow significantly with time (see Figures 4.1a and 4.1d). By comparing these cluster size time evolutions for different systems, it is clear that with ion sizes 0.9σ and 0.8σ (Figures 4.1b and 4.1c), the lipid cluster sizes are larger than those with ion size

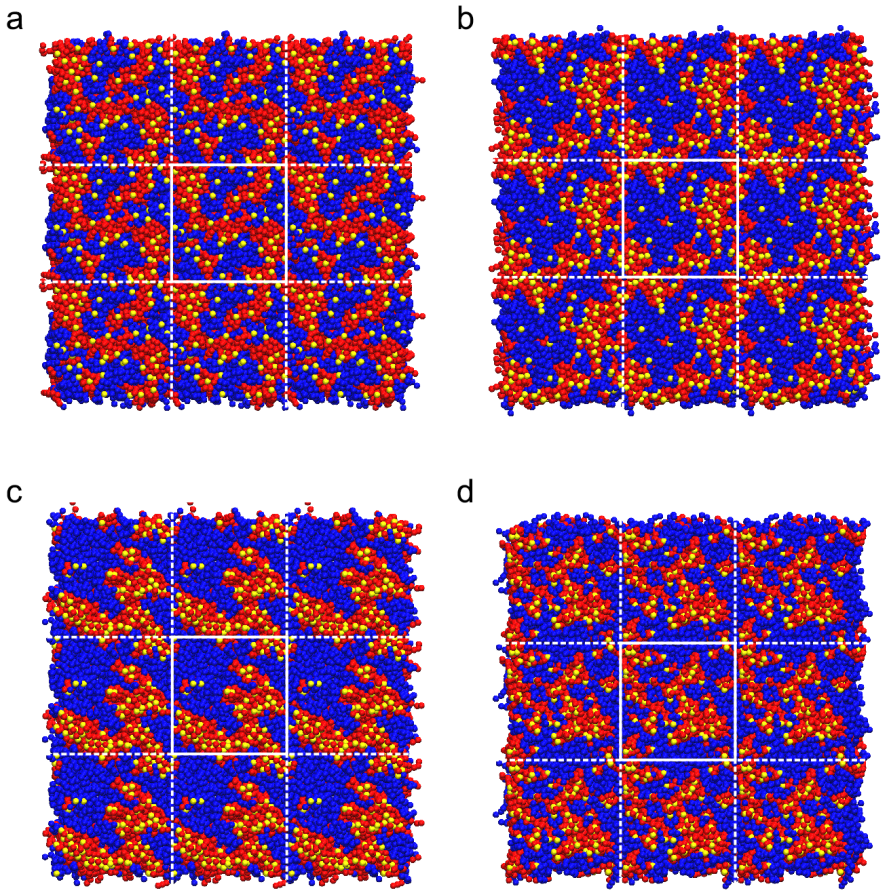

Figure 4.3: Effect of 0.4M M^+ ion size on 240 lipid 1:1 POPC/POPS lipid bilayer. (a-d) Representative snapshots (with eight additional replicas) of the most populated cluster for bilayer 1.0σ (9 lipids) , 0.9σ (22 lipids), 0.8σ (56 lipids) and 0.7σ (8 lipids) ions respectively. Blue lipids represent POPC and red, POPS. Ions within 5.5Å of POPS and POPC phosphate groups and 2.0Å of POPS serine groups are shown in yellow. Periodic boundaries in the simulation box are shown in white lines. The middle box with white solid lines is the primary cell in the simulation box.

1.0σ and 0.7σ, which stays under 20 lipids for most of the time. In Figures 4.1b and 4.1c, there are more fluctuations in the largest cluster size, in comparison to

Figures 4.1a and 4.1d. This is because, when larger ion-lipid clusters are observed, the diffusion of ions on the bilayer contribute to frequent clusters breaking and re-forming due to realignment of ion-lipid interactions. Similar trends in cluster sizes are observed when we characterize cluster sizes using the clustering method based on bilayer 2D Voronoi diagrams (Figure 4.2). Since the total number of POPS lipids in each leaflet is 60, almost all POPS lipids are bound via cations by 200ns in the system with 0.8σ M^+. The effect of cation size in lipid demixing is more obvious by comparing representative snapshots of the most populated cluster for these four distinct systems (see Figure 4.3). The blue and red beads represented in Figure 4.3 are POPC and POPS lipids, respectively. M^+ ions within 5.5 Å of phosphate groups and 2.0 Å of serine groups are represented in yellow. This coloring scheme is consistent throughout the article. Visually, Figures 4.3a (1.0σ M^+) and 4.3d (0.7σ M^+) show much smaller ion-mediated clusters of POPS, in comparison to Figures 4.3b (0.9σ M^+) and 4.3c (0.8σ M^+), with the largest POPS clusters seen with 0.8σ M^+ ions. The representative snapshot of the system with 1.0σ M^+ ions shows the most populated cluster size of 9 lipids, with 0.9σ M^+ ions, 22 lipids, with 0.8σ M^+ ions, 56 lipids and with 0.7σ M^+ ions, 8 lipids.

To characterize the role of 0.8σ M^+ ion concentration on lipid domain formation, we simulated 240 lipid bilayer systems with 0M (with counterions present) and 0.2M ions. Figure 4.4 compares the histogram of lipid clusters and time evolution of the largest PS cluster for 0.4M (Figures 4.4a and 4.4d), 0.2M (Figures 4.4b and 4.4e) and 0M (Figures 4.4c and 4.4f). With the increase in ion concentration, there is a corresponding increase in cluster growth (Figures 4.4f to 4.4d). In systems with

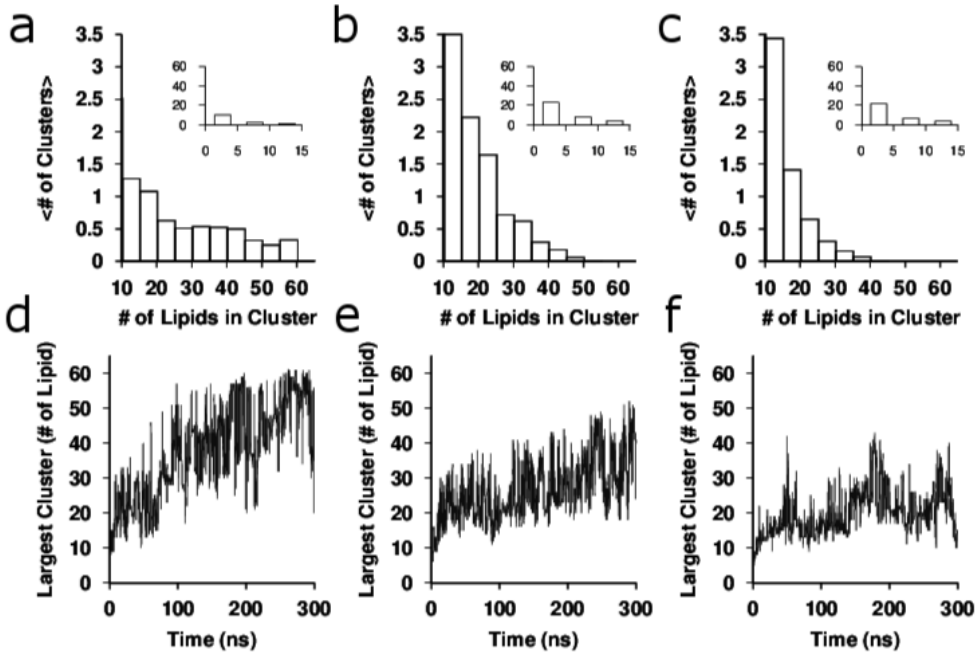

Figure 4.4: Effect of 0.8σ M^+ ion concentration on 240 lipid 1:1 POPC/POPS lipid bilayer. (a-c) Distribution of POPS lipid cluster size at ion concentrations of 0.4M, 0.2M and 0M (with counter-ions) respectively. (d-f) Cluster time evolution at ion concentrations of 0.4M, 0.2M and 0M (with counter-ions) systems respectively. Data obtained from clustering method based on ion-lipid cutoff distances.

0M and 0.2M 0.8σ M^+, all cations present in the system are bound to lipids. Figures 4.5a-c represent snapshots of the most populated ion-POPS cluster size, which is 20 lipid cluster of 0M (Figure 4.5a), 23 lipid cluster for 0.2M (Figure 4.5b) and 56 lipid cluster for 0.4M(Figure 4.5c). Therefore, there is a concentration effect observed at 0.8σ M^+, and the observed changes in physicochemical properties of the lipid bilayer is dependent on the ion concentration. To summarize, stronger lipid demixing is observed as the cation concentration is increased.

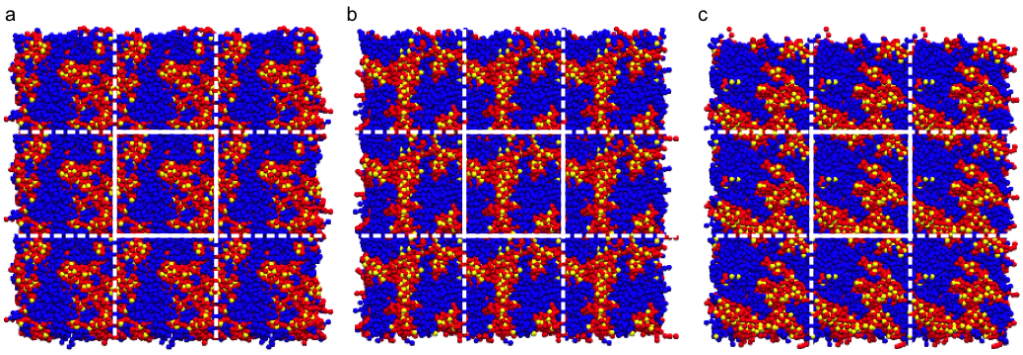

Figure 4.5: Effect of 0.8σ M^+ ion concentration on 240 lipid 1:1 POPC/POPS lipid bilayer. (a-c) Representative snapshot of lipid bilayer with 0.0M(with counter-ions), 0.2M and 0.4M respectively. Blue lipids represent POPC and red, POPS. Periodic boundaries in the simulation box are shown in white lines. The middle box with white solid lines is the primary cell in the simulation box.

Ion-lipid coordination in general is known to be correlated with ion-induced lipid dehydration [211]. More specifically, ions that are known to induce domain formation in PS mixtures, like calcium, exhibit a more significant dehydration effect displacing water bound to lipids [49, 124, 212, 213]. To see if we observe a similar water displacement effect, we evaluated water hydration curves for POPC and POPS lipids in all four systems (Figure 4.6). The water hydration curves are obtained by integrating the RDF between the lipid phosphate group and water beads. The displacement effect for POPS induced by ions is more significant than that for POPC in all four systems. This suggests that more ions bind to anionic POPS lipids and lead to the displacement of water molecules. The difference in water hydration curves between POPC and POPS is the most significant for bilayers with

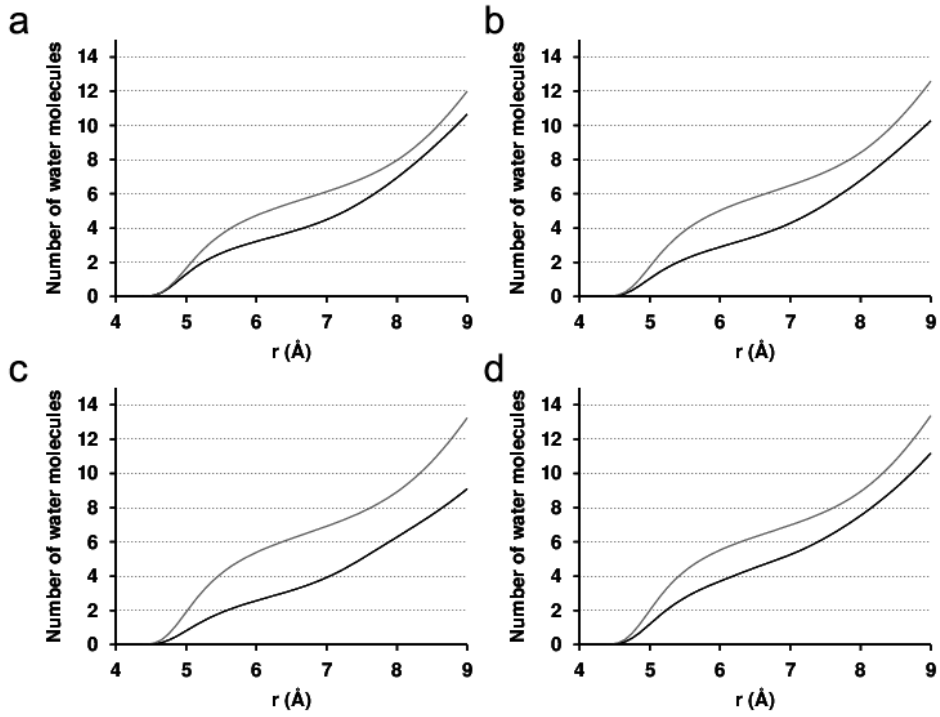

Figure 4.6: Effect of 0.4M M^+ ion size on 240 lipid 1:1 POPC/POPS lipid bilayer. (a-d) Water displacement curves for POPC (gray) and POPS (black), for systems with 1.0σ, 0.9σ, 0.8σ and 0.7σ cations respectively.

0.8σ M^+ ions (see Figure 4.6c). That is, there are both (a) less number of water molecules around POPS lipids and (b) greater difference in water displacement between POPC and POPS lipids with 0.8σ M^+ ion size. Li^+, like Ca^{2+}, is also known to form dehydrated cation-PS complexes [44, 45, 47, 48]. Therefore, we can hypothesize that small monovalent cations, like Li^+ ions, could lead to dehydrated PS domain formation in PC-PS mixtures.

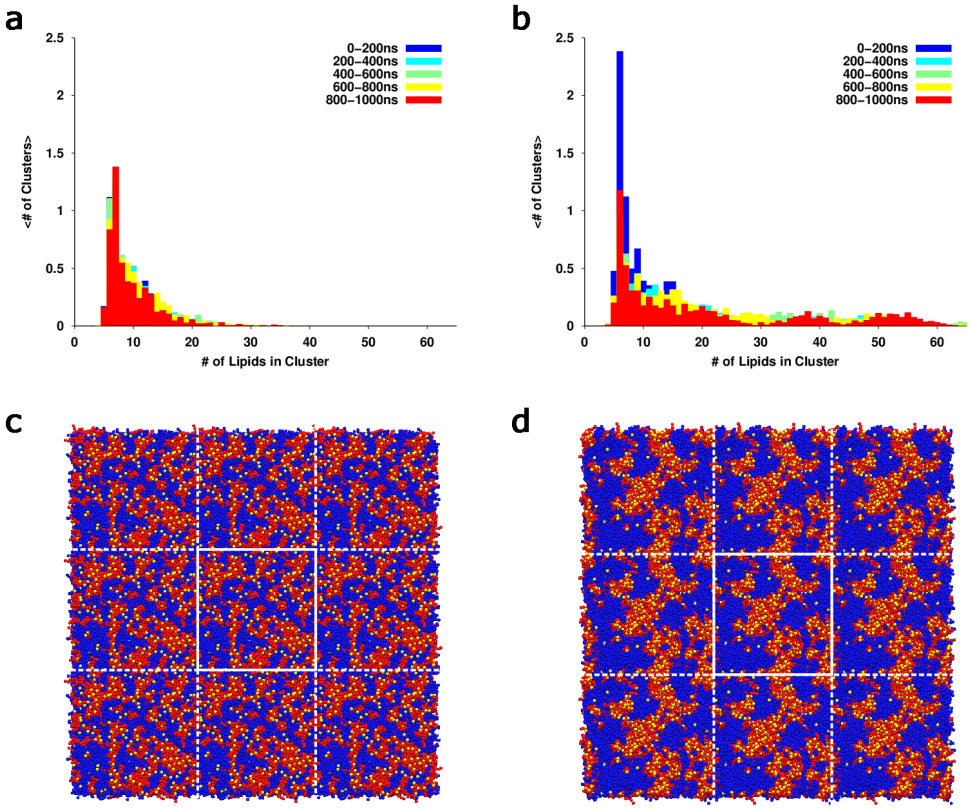

Figure 4.7: (a-b) Effect of 0.4M M^+ ion size on 960 lipid 1:1 POPC/POPS lipid bilayer. POPS cluster size distributions at different time intervals for system with (a) 1.0σ and (b) 0.8σ ions. Data obtained from clustering method based on bilayer 2D Voronoi diagrams. (c-d) Representative snapshots (with eight additional replicas) of a bilayer with 1.0σ (c) and 0.8σ (d) ions. Blue lipids represent POPC and red, POPS. Ions within 5.5Å of POPS and POPC phosphate groups and 2.0Å of POPS serine groups are shown in yellow. Periodic boundaries in the simulation box are shown in white lines. The middle box with white solid lines is the primary cell in the simulation box.

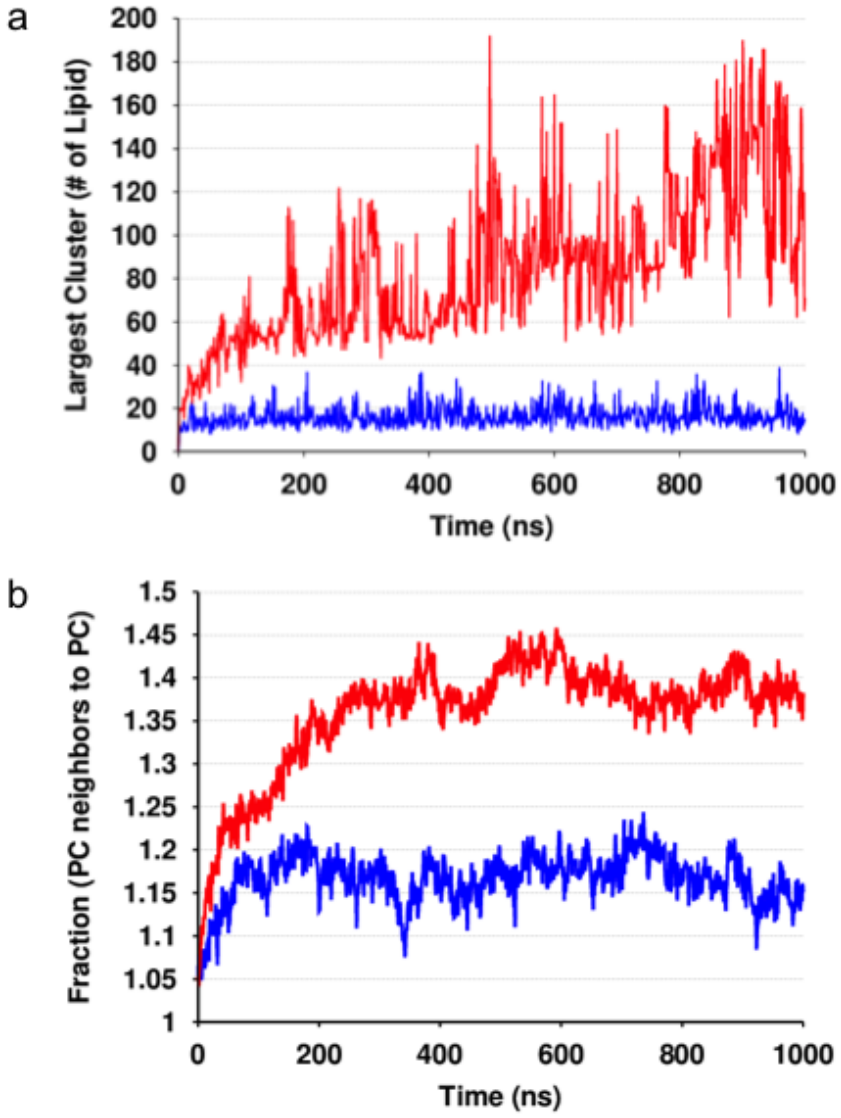

Figure 4.8: Effect of 0.4M M^+ ion size on 960 lipid 1:1 POPC/POPS lipid bilayer. (a) Cluster time evolution of POPS lipid clusters with 1.0σ M^+ (blue curve) and 0.8σ M^+ (red curve) cations respectively. Data obtained from clustering method based on ion-lipid cutoff distances. (b) Time evolution of adjacency ratio between PS and PC around PS lipids with 1.0σ (blue curve) and 0.8σ M^+ ions (red curve).

4.4.1.2 Lipid Nanodomain Formation at 0.8σ M^+

In Figure 4.1, the maximum POPS cluster size of 60 lipids (60 POPS lipids per leaflet in a 240 lipid 1:1 POPC/POPS system) is reached within the first 200-250ns, which suggests a possible finite size effect. To fully explore length- and time scale effects we used a 960-lipid bilayer with (a) 0.8σ M^+ ions, to explore growth of lipid clusters and (b) 1.0σ M^+ ions as control. The simulation time is $1\mu s$ and an ion concentration consistent with our prior simulations is used. Figures 4.7a and 4.7b show the distributions of POPS cluster sizes at different time intervals for systems with 1.0σ and 0.8σ M^+ ions respectively, using the clustering method based on bilayer 2D Voronoi diagrams. The cluster size distributions at multiple time intervals overlap for the system with 1.0σ M^+ ions (see Figure 4.7a). On the other hand, in the system with 0.8σ M^+ ions (Figure 4.7b), there is a shift in cluster size distribution towards larger clusters over time. These results can be reconciled with the largest ion-mediated cluster size time evolution in Figure 4.8a with the ion-distance cutoff method. The size of the largest POPS Voronoi cluster with 1.0σ M^+ ions remains around 10-30 lipids (blue curve) throughout the trajectory, whereas for the system with 0.8σ M^+, the largest cluster grows from 20 to about 150 lipids (red curve). By $1\mu s$, around 100 lipids are part of the growing cluster, which is the scale of a nanodomain due to its size. It is worth mentioning that the largest 1.0σ M^+ ion-mediated POPS cluster size with both 240- and 960-lipid bilayer is around 10-30 lipids, therefore the absence of lipid cluster growth with 1.0σ M^+ is not due to a finite size effect. We also measured the PS-PS lipid

adjacency ratio, which is the fraction of POPS Voronoi neighbors to POPS lipids (Figure 4.8b) [185] . The higher the ratio, the more PS lipids are adjacent to other PS lipids. The PS-PS lipid neighboring fraction values are normalized to the composition of PS lipid in the leaflet to highlight the relative enrichment/depletion of PS-PS neighbors. Randomly distributed lipids are expected to have a neighboring fraction value of 1.0. The system with 0.8σ M^+ (red curve) ions has a higher fraction of PS neighbors (around 1.4 times increased adjacency fraction) than that with 1.0σ M^+ (blue curve) (around 1.2 times increased adjacency fraction), which is indicative of a more pronounced PS lipid clustering. Therefore, although ion-mediated PS lipid clusters are observed in both cases, the system with 0.8σ M^+ ions (a) induces more PS lipid aggregation and (b) induces PS clusters that grow with time (red curve in Figure 4.8a). Representative snapshots of the most populated ion-POPS cluster, with 1.0σ M^+ (16 lipids) and 0.8σ M^+ (74 lipids) are depicted in Figures 4.7c-d, respectively. In both 0.8σ M^+ systems, the clusters at distinct times are larger than half the size of the box, thus suggesting still the presence finite size effects.

To account for any time scale effects, we simulated a phase-separated PC-PS system with 1.0σ M^+, 0.9σ M^+, 0.8σ M^+, and 0.7σ M^+ ions, all in water at time t=0ns. Figure 4.9 depicts the POPS lipid adjacency fraction of systems with 1.0σ M^+, 0.9σ M^+, 0.8σ M^+, and 0.7σ M^+ ions respectively. Since the system is pre-assembled as a phase-separated bilayer at time 0ns, the PS-PS adjacency fraction value is as high as 1.8. However, for both systems with 0.7σ M^+ (Figures 4.9d) and 1.0σ M^+ ions (Figure 4.9a), the average fraction value decreases to around 1.2 within $2\mu s$ and 1 μs respectively. This is in agreement with the PS neighboring

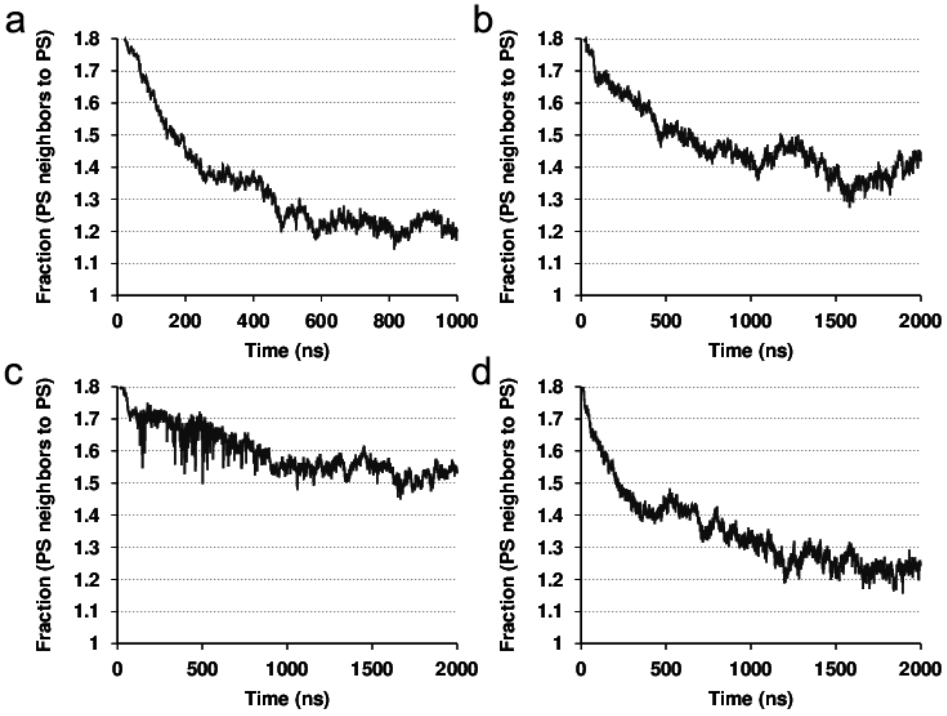

Figure 4.9: Effect of 0.4M M^+ ion size on 960 lipid 1:1 POPC/POPS phase-separated lipid bilayer. Time evolution of adjacency ratio between PS and PC around PS lipids with (a) 1.0σ M^+, (b) 0.9σ M^+, (c) 0.8σ M^+ and (d) 0.7σ M^+ ions.

fraction value observed in the bilayer with the 1.0σ M^+, starting from a random lipid distribution. For systems with both 0.9σ M^+ (Figure 4.9b) and 0.8σ M^+ ions (Figure 4.9c), the drop in PS neighboring fraction value is slower, achieving a value around 1.4 and 1.5, respectively by the end of $2\mu s$, suggesting a more PS-aggregated system. This is also in agreement with the results obtained starting from a random distribution of lipids. Figure 4.10 represents the Voronoi cluster size distributions for the above four systems at different time intervals. The POPS cluster size distribution shifts from larger cluster sizes to smaller ones, with largest

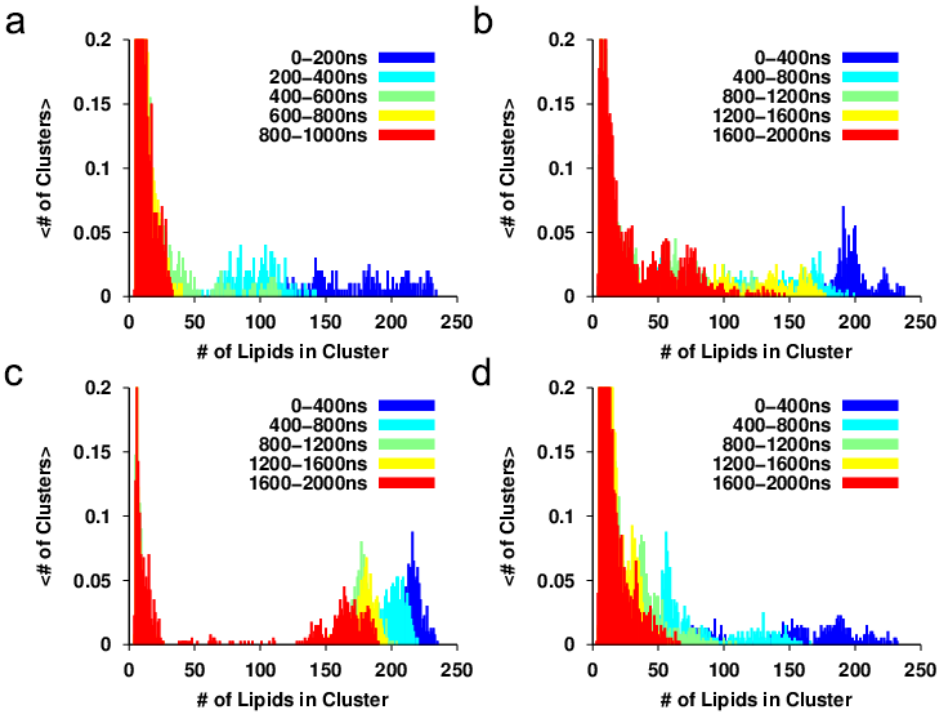

Figure 4.10: Effect of 0.4M M^+ ion size on phase-separated 960 lipid 1:1 POPC/POPS lipid bilayer. (a-d) Cluster size distribution of POPS lipids at different time periods for systems with ion sizes of 1.0σ , 0.9σ , 0.8σ and 0.7σ respectively. Data obtained from clustering method based on bilayer 2D Voronoi diagrams.

cluster sizes seen in system with 0.8σ M^+ ions after $2\mu s$ (Figure 4.10c). Figure 4.10 represents the time evolution of the largest Voronoi lipid cluster size. From Figure 4.11, it is evident that for bilayer systems with 0.9 M^+ and 0.8 M^+ ions (Figures 4.11b and 4.11c), the process is slower than that of 1.0 M^+ and 0.7 M^+ ions (Figures 4.11a and 4.11d).

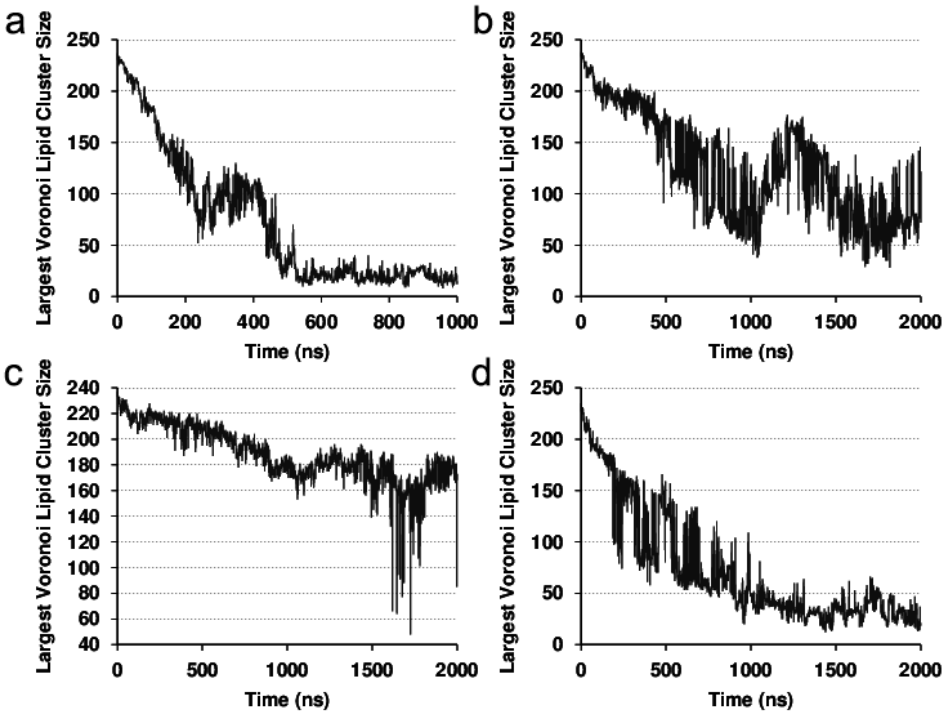

Figure 4.11: Effect of 0.4M M^+ ion size on phase-separated 960 lipid 1:1 POPC/POPS lipid bilayer. (a-d) Time evolution of largest cluster size of POPS lipids for systems with cation sizes of 1.0σ, 0.9σ, 0.8σ and 0.7σ respectively. Data obtained from clustering method based on ion-lipid cutoff distances.

4.4.2 Effect of Monovalent Ion Size on Bilayer Properties

There is a clear distinction between the effects of 1.0σ M^+ and 0.8σ M^+ ions on nanodomain formation in PC/PS mixtures. The above results raise the following question, how does the ion-mediated lipid domain formation affect bilayer properties? To address this question, we investigated a number of physical properties of the two systems with 0.8σ M^+ and 1.0σ M^+ ions. Figure 4.12 represents lateral

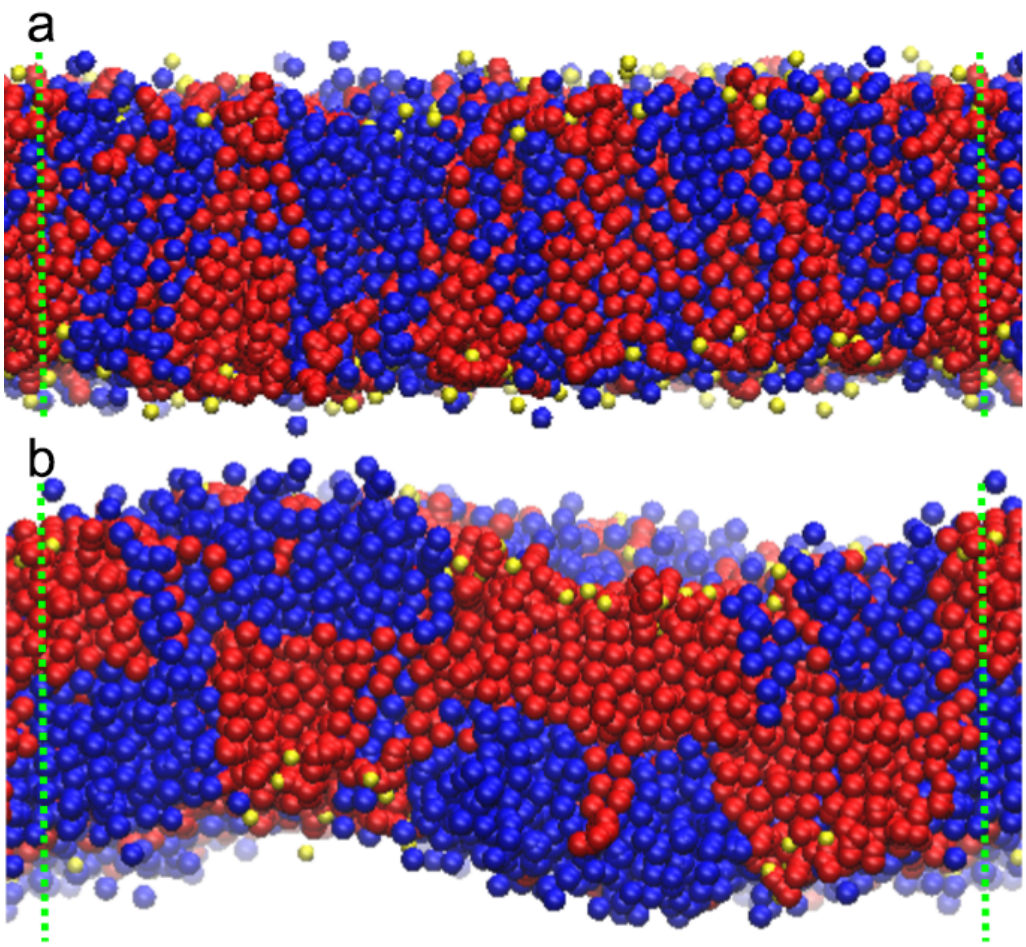

Figure 4.12: Effect of 0.4M M^+ ion size on 960 lipid 1:1 POPC/POPS lipid bilayer. (a-b) Representative lateral snapshot of lipid bilayers with 1.0σ and 0.8σ ions respectively at $1\mu s$. Blue lipids represent POPC red, POPS. Ions within 5.5 Å of POPS and POPC phosphate groups and 2.0 Å of POPS serine groups are shown in yellow. The simulation box is denoted by dotted green lines.

snapshots of the 960-lipid bilayer, at $1\mu s$ with 1.0σ M^+ (Figure 4.12a) and 0.8σ M^+ (Figure 4.12b) ions. We can visually distinguish three features from these images, (a) *bilayer curvature*: bilayer with 0.8σ M^+ cation-mediated POPS nanodomains

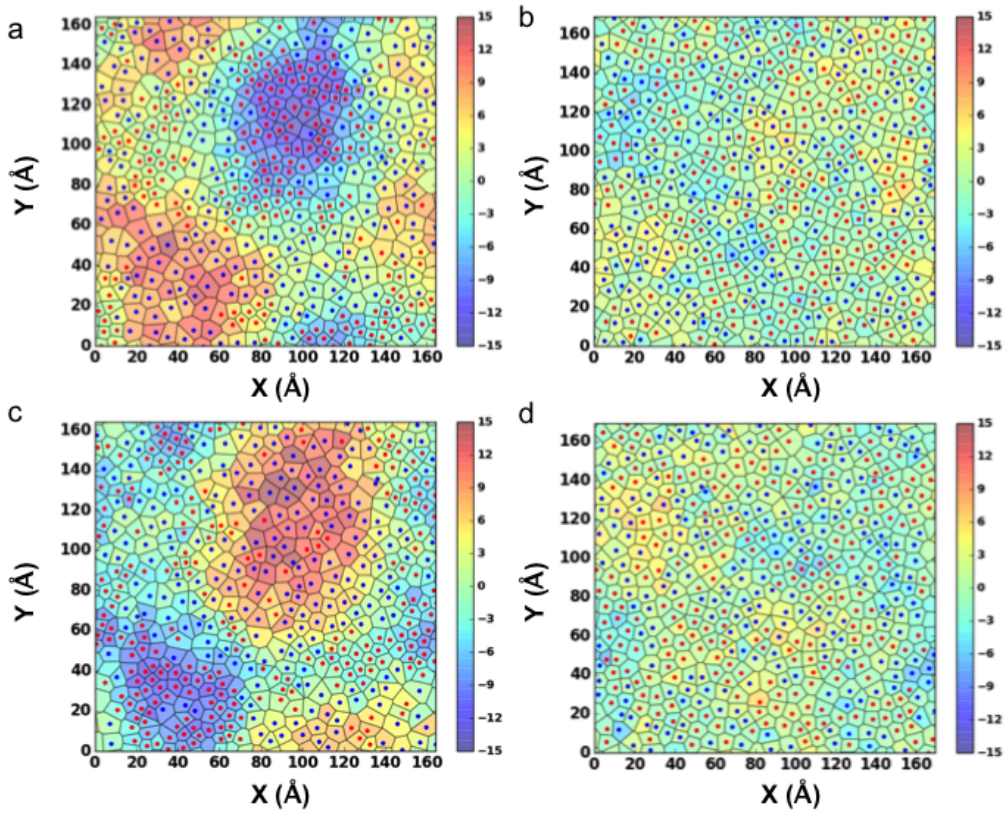

Figure 4.13: Effect of 0.4M 0.8σ and 1.0σ M^+ ion size on 960 lipid 1:1 POPC/POPS lipid bilayer. (a and c) Voronoi diagram of upper and lower lipid leaflets with 0.8σ M^+ ions. (c-d) Voronoi diagram of upper and lower lipid leaflets with 1.0σ M^+ ions. Each cell represents a lipid, the centroid of the cell is colored red for POPS and blue for POPC. The color bar denotes vertical distance in of z position of the respective lipid PO4 to the center of mass of leaflet PO4 in Å.

(Figure 4.12b) has a significant curvature, which is visually absent in the system with 1.0σ M^+ (Figure 4.12a) ions. It is also interesting to note that POPS domains (red lipids) in Figure 4.12b tend to have negative curvature, while POPC domains are more likely to have positive curvature; (b) *bilayer asymmetry*: Figure 4.12b

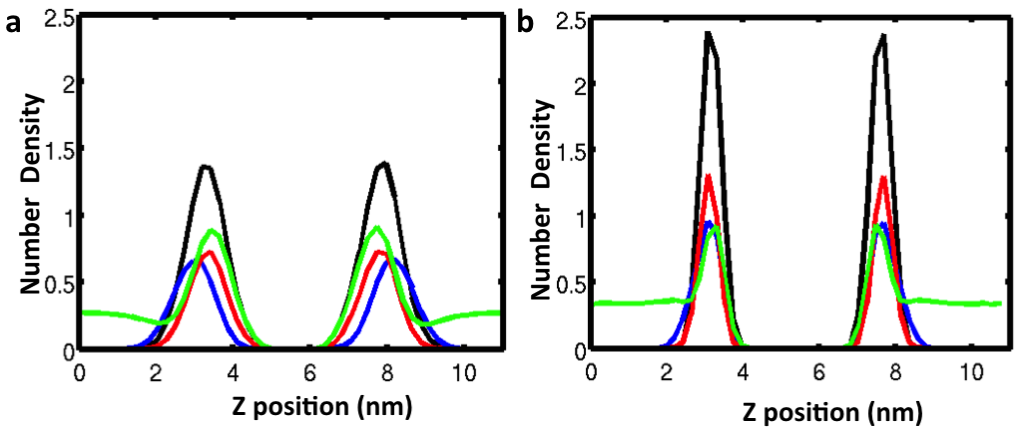

Figure 4.14: Effect of 0.4M M^+ ion size on 960 lipid 1:1 POPC/POPS lipid bilayer. (a) Density distribution of different groups with (a) 0.8σ M^+ and (b) 1.0σ M^+ ions. Colors: phosphate beads in black, M^+ in green, serine in red, and choline in blue.

shows compositional asymmetry between red POPS lipid domains and blue POPC lipid domains, and this preference is not prominent in the system with 1σ M^+ ion (Figure 4.12a); (c) *Ion distribution*: cations are found to have a preference for POPS (red lipids) over POPC (blue lipids) in Figure 4.12b, which is not prominent in Figure 4.12a. There are on average 587.6 ions in the PS region, in the last 500ns in comparison to 153.8 ions in the PC region for the system with 0.8σ M^+ ion. On the other hand, there are 349.8 ions in the PS region and 261.0 in PC for 1.0σ M^+ respectively. Figure 4.13 represents a more quantitative picture of the relationship between lipid compositional asymmetry and bilayer curvature in systems with 0.8σ M^+ ions (top and bottom leaflets in Figures 4.13a and 4.13c respectively) and 1.0σ M^+ ions (top and bottom leaflets in Figures 4.13b and 4.13d respectively). Each Voronoi cell in Figure 4.13 represents a lipid. The centroid of the cell is red if it is

occupied by POPS lipids and blue if it is occupied by POPC lipids. To measure the bilayer curvature, we defined the average z position (or height) of phosphate groups (PO4) for each leaflet. Then we calculated δz for each phosphate bead relative to the average position of phosphate beads in the same leaflet. The δz value in Å is represented in the color bar. Positive δz values (warm colors) denote outward projections of each lipid from the bilayer, and negative values (cool colors) denote inward projection. From Figures 4.13a and 4.13c, it is clear that regions with negative δz values or curvature are usually occupied by POPS lipids (blue Voronoi cells with red centroids), and positive curvature, by POPC lipids (warm colored Voronoi cells with blue centroids). The planar distributions of POPC and POPS lipids on both leaflets are also intriguing. The regions occupied by POPS lipids in the top leaflet (60-120 Å in x and 100-140 Å in y) are occupied by mostly POPC lipids in the bottom leaflet. To the contrary, for the system with 1.0σ M^+ ions, there is neither a significant change in curvature nor a corresponding effect on compositional asymmetry. We then calculated Pearson correlation coefficients for lipids in one leaflet with lipids in the other lipids for both systems. In the system with 0.8σ M^+ ions, POPS lipid distributions on the upper and lower leaflets are negatively correlated (r=-0.4555 $\pm$ 0.0735), which suggests that PS domains on the bilayer adopt an asymmetric distribution across the leaflets. However, for the system with 1.0σ M^+ ions, POPS lipids on either leaflets are not significantly correlated (r=-0.06186 $\pm$ 0.19198). The above results can also be reconciled with the density distributions of different lipid headgroups for systems with 0.8σ M^+ ions (Figure 4.14a) and 1.0σ M^+ ions (Figure 4.14b). The broader peaks of the phosphate group distribution with

0.8σ M^+ ions (black curve in Figure 4.14a) is indicative of bilayer curvature, whereas high and sharp peaks of the phosphate group distribution with 1.0σ M^+ ions (black curve in Figure 4.14b) is typical for bilayers with no curvature. The vertical shift from the distribution of red (serine or CNO) and blue peaks (choline or NC3) in Figure 4.14a, which is absent in Figure 4.14b, suggests negative curvature for POPS domains. The serine peaks are shifted towards the center of the bilayer (located at 5-6nm in x axis), and choline peaks are shifted towards the water-bilayer interface. This distinction is not observed in the system with 1.0σ M^+ ions in Figure 4.14b. The position of monovalent cations (green curves) in Figure 4.14a is also shifted to the center of the bilayer and partially overlaps with the serine group distribution. This suggests that more 0.8σ M^+ ions preferentially partition into POPS regions over POPC regions.

Figure 4.15 quantifies area per lipid of POPC and POPS lipids in systems with 0.8σ M^+ (Figures 4.15a and 4.15c) and 1.0σ M^+ (Figures 4.15b and 4.15) ions. Each Voronoi cell in Figure 4.15 represents a lipid. The centroid of the cell is red if it is occupied by a POPS lipid and blue, if it is occupied by a POPC lipid; and the color on the grid is a measure of the area of the Voronoi cell or the lipid. From Figures 4.15a and 4.15c, the regions with POPS lipids are more condensed with lower area per lipid (APL) than regions with POPC lipids. This distinction is absent in the system with 1.0σ M^+ ions or Figures 4.15b and 4.15d. The cations exhibit higher affinity to negatively-charged POPS lipids. On binding to the lipid, the cations decrease the electrostatic repulsion of negatively-charged PS headgroups, causing a decrease of the APL in the PS domain. The low APL induced

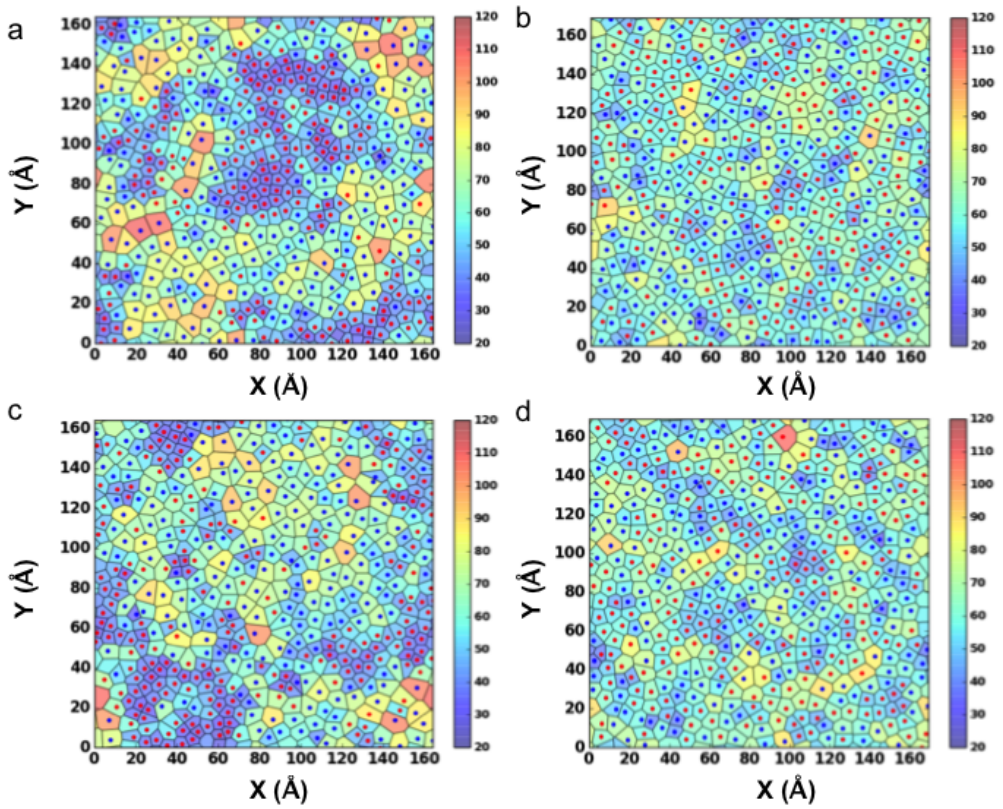

Figure 4.15: Effect of 0.4M 0.8σ and 1.0σ M^+ on 960 lipid 1:1 POPC/POPS lipid bilayer. (a and c) Voronoi diagram of upper and lower lipid leaflets with 0.8σ M^+ ions. (b and d) Voronoi diagram of upper and lower lipid leaflets with 1.0σ M^+ ions. Each cell represents a lipid, the centroid of the cell is colored red for POPS and blue for POPC. The color bar denotes area per lipid or area per each Voronoi cell in $Å^2$.

by ion condensation effects, in the POPS region, leads to a spontaneous negative curvature. Since this effect is not present in POPC regions, the POPC regions are forced to adopt a positive curvature to stabilize the bilayer structure (see Figure 4.13c). Cationic antimicrobial peptides are also known to induce negative curvature in anionic membranes due to a similar electrostatic effect [214]. Figure 4.16 shows a typical ion-PS complex with 0.8σ M^+ ions, the headgroups are more condensed and

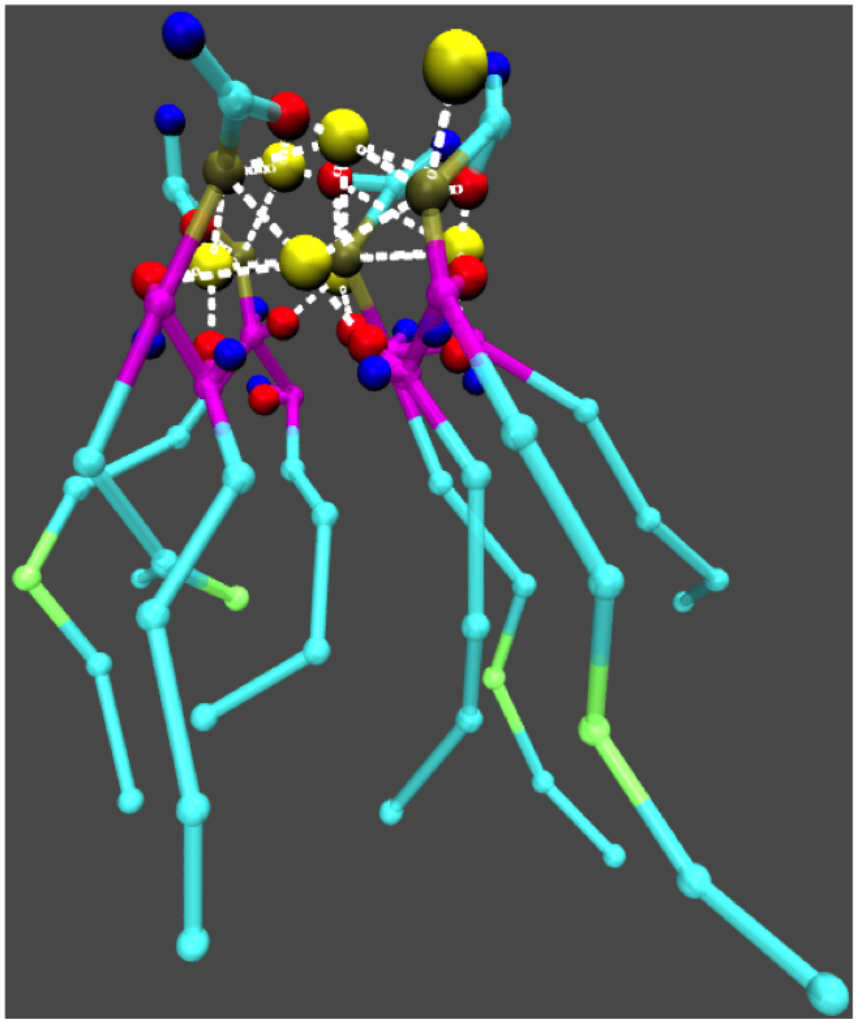

Figure 4.16: A typical ion-lipid complex with 4 POPS lipids. Colors: ions in yellow, alkyl tails in cyan, ester groups in magenta, phosphate in tan, positive and negative serine dummies in blue and red respectively. All electrostatic interactions between positive and negative particles, less than 5 Å are highlighted in white.

the tails are more tilted from the normal direction in the bilayer. The ion-POPS complex adopts a cone-like shape, with larger area occupied by tails and smaller area by lipid headgroups, hence facilitating the negative curvature in POPS regions. Figure 4.17 is a schematic image illustrating the necessity of adopting opposite

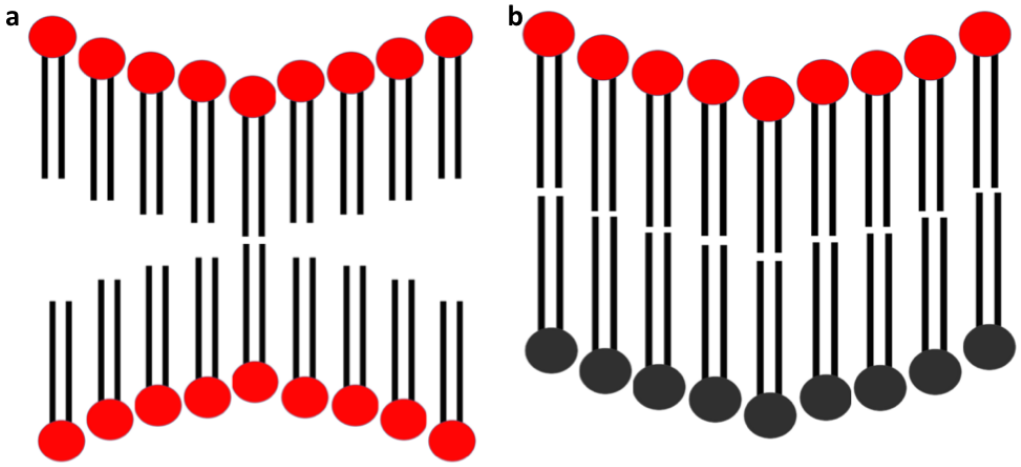

Figure 4.17: Schematic lipid bilayer cartoon with lipids of the same tail length organized as two leaflets. (a) Both leaflets with negative curvature and (b) upper leaflet with negative curvature and lower leaflet with positive curvature. Lipids with red headgroups represent POPS and black, POPC.

curvature on both leaflets. Compositional symmetry with POPS regions exhibiting negative curvature on both leaflets is not possible as it leads to the formation of voids in the bilayer center (Figure 4.17a).

The correlation between lipid compositional asymmetry and bilayer curvature has been observed in MD simulation studies using ternary mixtures of saturated lipids, unsaturated lipids, and cholesterol [190, 215]. However, this paper is the first study to capture properties typical to phase separation processes, driven by ion-lipid headgroup interactions. Recent studies on POPC bilayers show that changes in curvature and lateral pressure profiles induced by membrane potential [216] can be explained by flexoelectricity [217]. Therefore, we hypothesize that monovalent cations of certain sizes have the ability to induce changes in bilayer electric potential

that contributes to the curvature in cellular membranes.

The difference in the APL between the PS and PC regions is critical for bilayer curvature and lipid compositional asymmetry. The average APL for systems with different ion sizes is correlated with cluster growth and domain formation (Figures 4.1 and 4.3). The area per lipid decreases from systems with 1.0σ M^+ (60.51 ± 0.04Å ^{2}) to 0.9σ M^+ (58.89 ± 0.05Å ^{2}) to 0.8σ M^+ (57.57 ± 0.05Å ^{2}) and then increases for 0.7σ M^+ (59.17 ± 0.05Å ^{2}) ions, consistent with the increase in the largest ion-mediated clusters size from 1.0σ M^+ to 0.8σ M^+ and the drop at 0.7σ M^+ ions. Therefore, we conclude that the ion condensation effect, as implied by the decrease in APL, leads to an increase in cluster growth and domain formation. An MD study on the effect of monovalent cations on DPPS, shows comparable trend of decrease in APL along with the decrease in ion size, from Na^+ (54.00 ± 0.01Å ^{2}), to Li^+ (51.0 ± 0.06Å ^{2}) [218]. The same study also suggests that the presence of Li^+ increases the ion-mediated lipid-lipid interactions while reducing the direct interactions between lipids.

There is clearly a range of monovalent ion size that induces the growth of ion-mediated POPS clusters. These clusters have a characteristic decrease in the APL indicating a condensation effect. However, the question remains why only M^+ ions with sizes 0.8σ and 0.9σ exhibit lipid domain formation, and what is special about the M^+ ion size range which is capable of inducing domain formation. To answer this question, we investigated the lipid pairwise interaction energies and ion coordination number near lipid headgroups. Figures 4.18a and 4.18b represent the number of ions around phosphate (PO4) and serine (CNO) groups of POPS lipids in

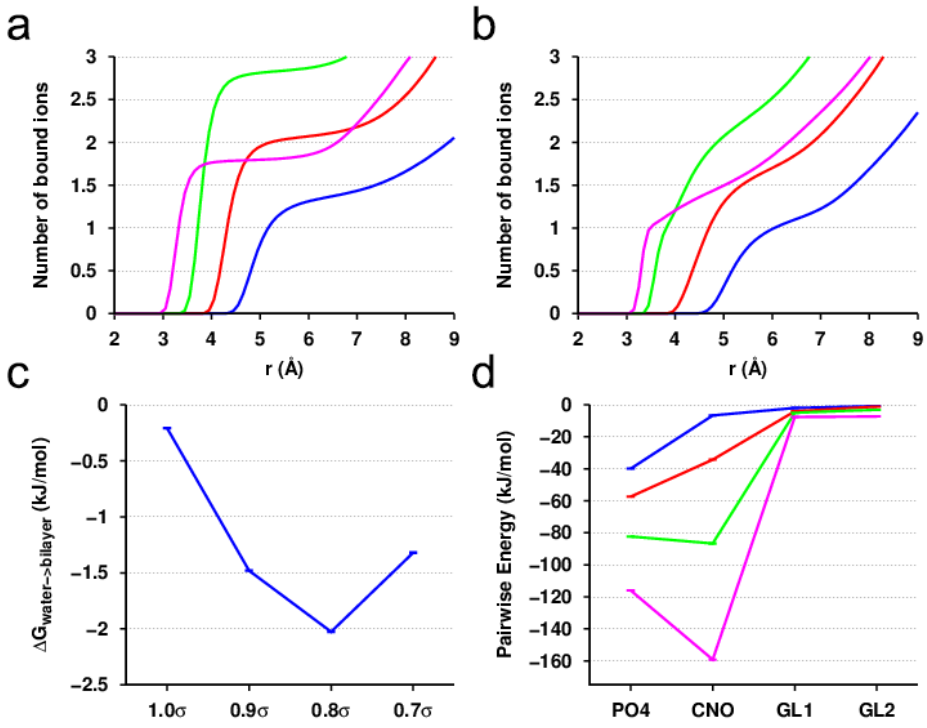

Figure 4.18: Effect of 0.4M ions on 240 lipid 1:1 POPC/POPS lipid bilayer. Number of bound ions with different sizes near (a) phosphate and (b) serine of POPS lipids. (c) Free energy of partition from water to bilayer for different ion radii. (d) Total pairwise energy of ion-POPS lipid headgroups, including serine (CNO), phosphate (PO4) and the two esters (GL1 and GL2). (a-b, d) Colors: 0.7σ M^+ in magenta, 0.8σ M^+ in green, 0.9σ M^+ in red and 1.0σ M^+ in blue.

different systems. Figures 4.18a and 4.18b show that 0.7σ M^+ ions are located closer to POPS phosphate and serine groups (magenta curves), while the total number of 0.8σ M^+ ions is higher near these groups (green curves). Consequently, there is a higher probability of finding a 0.8σ M^+ ion near either of the two POPS headgroups in comparison to any other ion. At 0.8σ M^+, the ions favorably interact with both

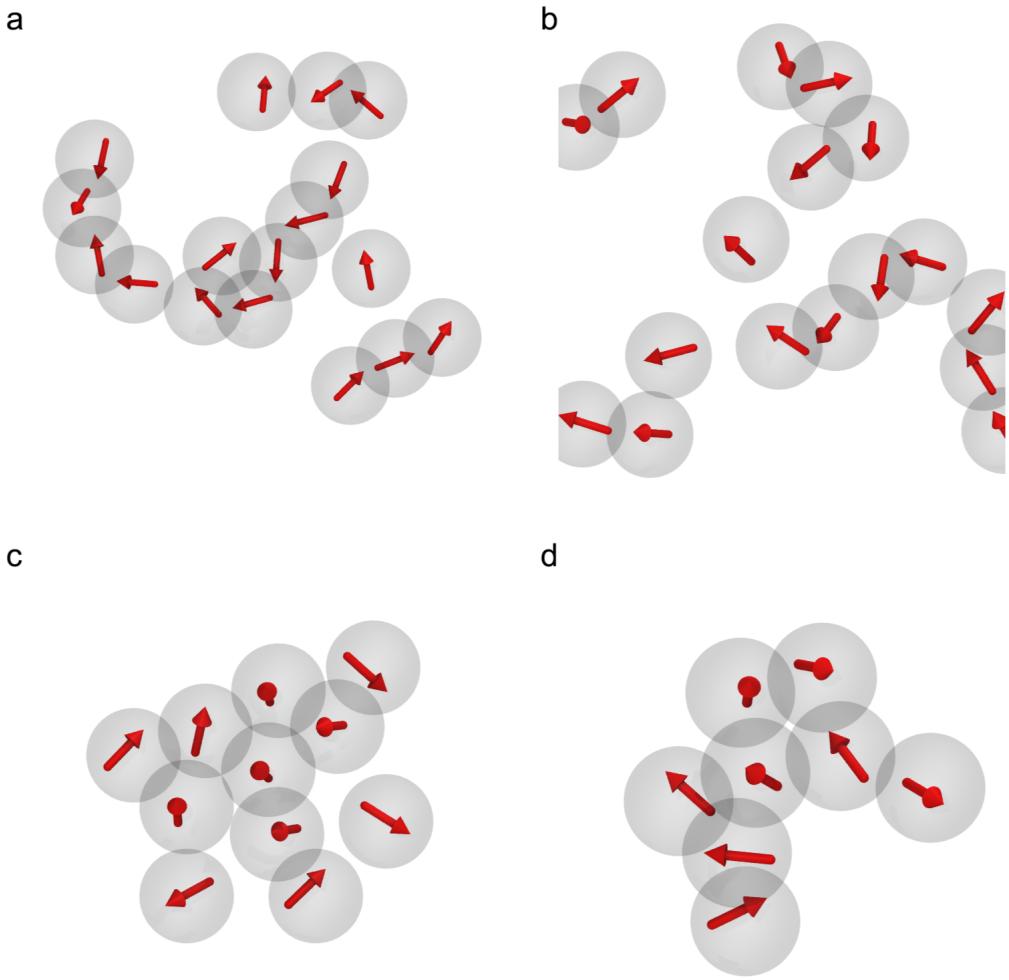

Figure 4.19: Dipole orientations of polarizable serine POPS headgroups (red vectors) observed in systems with ion size (a) 1.0σ M^+, (b) 0.9σ M^+, (c) 0.8σ M^+, and (d), 0.7σ M^+. Each transparent gray sphere represents the serine bead from the POPS lipid.

phosphate and serine groups, allowing for more combinations of ions bridging lipids to form larger clusters. On comparing the red and magenta curves in Figures 4.18a and 4.18b, there are more 0.9σ M^+ ions near phosphate groups of POPS (red curves) than 0.7σ M^+ ions, but the trend is reversed for ions near the serine group of POPS.

Figure 4.18c is a plot of the partition free energy ($\Delta G_{partition}$) from water to bilayer for ions with different sizes (for a description of the method see refer to ref [209]). It is clear from this plot that the $\Delta G_{partition}$ is the lowest for 0.8σ M^+ ions, which means more ions are able to partition into the bilayer. This is consistent with Figures 4.18a and 4.18b, in which more 0.8σ M^+ ions are found near phosphate and serine groups of POPS lipids (green curves). $\Delta G_{partition}$ for 1.0σ M^+ ions is the highest, and it is also consistent with Figures 4.18a and 4.18b (blue curves). 1.0σ M^+ ions are the furthest from lipids and occupy the fewest sites near POPS. Figure 4.18d shows the pairwise energies between cations with different sizes and headgroups. As expected, with the decrease in ion radius, the interaction energies decrease from 1.0σ M^+ (blue curve) to 0.7σ M^+(magenta curve). It is interesting to note that the ion-phosphate and ion-serine interactions dominate over ion-ester interactions. This suggests that in our model, the cations are not buried into the ester region, which is consistent with some all-atom simulation studies on monovalent ions like Na^+ and K^+ [51,125], but inconsistent with some other all-atom studies [50]. There is also a difference in the ratio of contribution from ion-phosphate interaction and ion-serine interaction. For 1.0σ M^+ (blue curve) and 0.9σ M^+ (red curve), the ion-phosphate interaction dominates, for 0.8σ M^+ (green curve), the contributions from phosphate and serine interactions are almost equal, and for 0.7σ M^+ (magenta curve), the ion-serine interaction dominates. Domain formation is not observed with 1.0σ M^+ because less ions partition into the bilayer and interact less strongly with lipid headgroups. Although $\Delta G_{partition}$ of 0.9σ and 0.7σ M^+ ions are almost the same, there are larger clusters formed with 0.9σ M^+ ions than with 0.7σ M^+ ions.

This is because of different binding modes in these two systems. For 0.9σ M^+ ions, ion-phosphate interaction dominates, whereas for 0.7σ M^+ ion-serine interaction dominates. This suggests that the dominance of ion-phosphate binding is crucial in inducing ion-mediated cluster growth and hence domain formation in anionic-zwitterionic mixtures. This result is also consistent with Figures 4.18a and 4.18b, where more 0.9σ M^+ ions (red curves) are near phosphate groups and more 0.7σ M^+ ions (magenta curve) are near serine groups. For 0.8σ M^+ ions, the $\Delta G_{partition}$ is the lowest and contributions from both ion-phosphate and ion-serine are almost equal. Therefore, there are sufficient ions to bridge multiple lipids through both ion-phosphate and ion-serine interactions. The above observations can be reconciled with Figure 4.19, the dipole alignments between neighboring serine beads of POPS lipids are depicted in a typical POPS cluster with M^+ ion sizes of 1.0σ, 0.9σ, 0.8σ, and 0.7σ respectively. Ion binding modes can also be correlated with serine dipole-dipole alignments. For example, the serine dipole-dipole alignment, as indicated by the red arrows, is more significant in Figures 4.19a and 4.19b, since both 1.0σ M^+ and 0.9σ M^+ ions prefer to bind to phosphate groups, thus the serine groups are free to interact and align with one another through dipole-dipole interactions, inducing linear PS lipid aggregates. On the contrary, in systems with both 0.8σ M^+ and 0.7σ M^+ ions, the ions bind to both phosphate and serine groups, and limit the dipole-dipole alignments between the serine beads. The ions also induce a globular aggregate of PS lipids (Figures 4.19c and 4.19d) since the ion-lipid binding is unbiased in all directions. The transition from linear dipole-dipole alignments to globular lipid aggregates is evident from the increasing fraction of PS-PS neighbors

(Figure 4.8b), as linear dipole-dipole alignment of PS lipids usually induce a lower PS-PS adjacency fraction value compared to the globular aggregates of POPS lipids.

To summarize, there are two contributing factors in driving monovalent cation-mediated domain formation in zwitterionic-anionic mixtures, they are (a) $\Delta G_{partition}$: the lower the partition free energy, the more ions partition into the bilayer and participate in lipid cluster growth; (b) binding modes: ion-phosphate interaction is more crucial than ion-serine interaction in cation-PS complex formation. The trend displayed by the monovalent cations with different sizes is consistent with the trend in properties observed for K^+, Na^+, and Li^+. Studies on monovalent cation interactions with PS bilayers indicate that ions like Na^+ and NH_4^+ have weak interactions with PS, while Li^+, Ca^{2+} or Mg^{2+} tend to have higher affinities [48]. NMR studies on monovalent $(Na^+, K^+, Li^+$)and divalent ion (Ca^{2+}, Mg^{2+}) ion binding to 5:1 POPC: POPS mixtures suggest that divalent ions, along with Li^+ are more deeply buried into the membrane in comparison to Na^+ and K^+ [193]. Infrared studies on DMPS bilayers with Li^+ and Ca^{2+} suggest both ions preferentially interact with phosphate and carboxylate groups of serine resulting in lipid aggregation [47]. Consequently, it is reasonable to claim the monovalent CG ion 0.8σ M^+ shares comparable binding mode and characteristics with Li^+.

4.5 Conclusion

Significant changes in ion-lipid interaction are observed depending on the CG cation sizes. The cation size effect on bilayers from our CG simulations is similar

to the bilayer property changes under the effect of K^+, to Na^+ and Li^+. The 0.8σ M^+ ion exhibits comparable binding modes and characteristics of Li^+. With 0.8σ M^+ ions and 1:1 POPC/POPS lipid bilayer, we observed formation of PC and ion-PS domains. Ion-PS domains have negative curvature and lower area per lipid due to ion condensation effects. PC domains are more liquid-like with higher area per lipid. The difference in structural properties of the two domains results in lipid compositional asymmetry. POPS lipid lateral distributions in one leaflet are negatively correlated with their distributions in the other leaflet. With 1.0σ cation sizes or low concentrations of 0.8σ M^+ cations, small local clustering is observed in the simulation. Since the physiological concentrations of cations in cells are relatively low, we estimate that only small nanodomains may be induced by the interactions between anionic lipids and cations at the inner leaflet of cell membranes, but not large lipid demixing is expected to occur.

Significant lipid domain formation is observed with 0.8σ M^+ ions because more cations partition into the bilayer and preferentially bind to both serine and phosphate groups in POPS lipids, which leads to cluster growth. For 0.9σ M^+ ions, ion-phosphate interaction dominates and for 0.7σ M^+ ions, ion-serine interaction dominates, which results in more ion-POPS clusters with 0.9σ over 0.7σ M^+ ions. This suggests that ion-phosphate interaction is more relevant than ion-serine interaction in driving ion-mediated lipid domain formation in anionic-zwitterionic lipid mixtures. The binding modes, reduction in APL, and water displacement effects induced by 0.8σ M^+ ions suggest that the simulated CG cation behaves similarly to Li^+, which has been found experimentally to induce headgroup dehydration and

ordered lipid packing [45]. Therefore, it is reasonable to hypothesize that Li^+ can induce the formation of distinct ion-rich POPS domains and POPC domains at an appropriate concentration in anionic-zwitterionic lipid mixtures. Our studies also suggest that some monovalent cations can significantly influence lipid structural and dynamic properties and play a crucial role in biological functions. We currently are working on understanding ion-lipid interactions in bilayers of varying composition and mixtures.

Chapter 4: Thesis Summary

4.1 Summary

The overall objective of this work was to utilize computational simulations and molecular models to investigate the role of electrostatics in a) polysaccharide hydrogel network formation, b) anticancer peptide SVS-1 folding on lipid bilayer, and c) cation-induced phospholipid nanodomain formation.

In Chapter 2, a coarse-grained polysaccharide model was developed to investigate the pH-dependent hydrogel network self-assembly from structural, mechanical, and thermodynamic perspectives. The CG model was the first to capture the self-assembly dynamics and quantify the elastic modulus of the chitosan hydrogel under different pH in a simulation. The hydrogel network was found to percolate at a higher rate with increased concentration and pH. Also, the structure factor analysis indicated the presence of long-range order in chitosan hydrogel network with high pH. The underlying molecular mechanism for the increased mechanical strength and long-range order was further illustrated by polymer crosslinking analysis. The crosslinking analysis showed that a strongly crosslinked hydrogel network tend to have more parallel crosslinkings between chitosan polymer chains, as opposed to perpendicular crosslinkings. Therefore, parallel crosslinkings between chitosan polymer

chains gave rise to more contacts between polysaccharide backbones, and increased the mechanical strength and long-range order in the network. We utilized the potential of mean force analysis to identify three typical crosslinking conformations in chitosan polymer network, a stable parallel crosslink, perpendicular crosslink, and on-pathway parallel crosslink. The transitions among these crosslinking patterns gave rise to structural and mechanical properties changes in different pH conditions.

In Chapter 3, we described the coarse-grained water-explicit polarizable protein (WEPPRO) and membrane (WEPMEM) model and their application in anticancer peptide SVS-1 folding on membrane surface. The WEPMEM model captures well the area per lipid and density distribution of POPC and POPS membrane bilayers. Also, this model mimics the dielectric constant of the interfacial region in PS membrane as in the atomistic model, which is suitable to study peptide folding on membrane surfaces. With the WEPMEM model, we observed a lipid headgroup clustering induced by dipole-dipole interactions. The network of lipid headgroup interactions resembles the hydrogen bonding network in atomistic simulations of POPS bilayer. We combined both WEPMEM and WEPPRO models, and examined POPS membrane-mediated folding of anticancer peptide SVS-1. The peptide folds into a β-hairpin conformation in agreement with experiments. Interactions including phosphate-lysine, valine-alkyl, intra-peptide, and serine/phosphate-peptide are the main driving forces for the folding. The binding of peptide to the bilayer was mostly driven by the electrostatic interactions between phosphate and lysine. The stabilization of peptide on the membrane surface was achieved by valine-alkyl and intra-peptide interactions. The subtle balance between intra-peptide interac-

tions and peptide-lipid interactions is the key to the β-hairpin formation in POPS membrane, and any alternation from such balance leads to an inhibition to folding.

In Chapter 4, we described the application of WEPMEM model in cation-induced lipid nanodomain formation. We have investigated the role of monovalent cation sizes in modulating lipid-ion binding modes and lipid demixing. The anionic lipid nanodomain formation was only induced by a window of monovalent cation sizes. When the cation size was either too large or too small, the growth of anionic lipid nanodomain in the simulations was impeded. The driving force for the anionic lipid aggregation was the electrostatic interactions between cations and phosphate/serine groups in lipid headgroups. When the cation size was large, not enough cations partitioned into the lipid headgroup region on the membrane surface. When the cation size was too small, they over-bound with the serine groups in anionic lipids and inhibits the lipid cluster growth. With the appropriate ion size, the ions bridged the interactions between lipids, and the interactions were balanced between phosphate and serine groups. In addition, membrane structural changes such as spontaneous curvature and inter-leaflet asymmetry were observed along with the formation of lipid nanodomains.

In summary, this thesis examined the effects of electrostatic interactions in biomolecular self-assembly processes in three study cases, (a) cation-induced lipid nanodomain formation, (b) membrane-induced anticancer peptide folding, and (c) pH-dependent polysaccharide hydrogel network formation. In all three cases, electrostatic interaction played a critical role in the self-assembly process. For the formation of anionic lipid nanodomains on a membrane surface, the lipids are bridged

by cations through the electrostatic interactions between ions and lipid headgroups. Moreover, the size of cations not only dictates the partitioning into a membrane, through electrostatic interactions, but also balances their electrostatic interactions between lipid phosphate and serine groups. Taken together, it leads to a window of cation sizes that induces the most aggregation of the lipids, and this explains why only Li^+ among all the monovalent cations induces significant melting temperature change in mixed anionic lipid bilayer [44–47] and the formation of dehydrated ion-lipid complexes [48]. There is also a subtle balance between peptide-lipid and intra-peptide interactions in the binding and folding of anticancer peptide SVS-1 on a membrane surface. The formation of headgroup-mediated lipid clusters lowers the interactions between lipids and peptides so that intra-peptide interactions dominate, and leads to SVS-1 hairpin conformation. On the other hand, if there is a lack of electrostatic interactions between lipid headgroups, there is an increase on lipid-peptide interactions and thus the disruption of the formation of peptide hairpin structure was observed. Although, instead of promoting self-assembly processes, the presence of electrostatic interactions in chitosan hydrogel network formation hinders the polymer self-assembly. For chitosan polymers under low pH, the repulsive electrostatic interactions between the protonated polyelectrolytes lead to the solvation of chitosan in an aqueous environment, whereas in high pH conditions, the chitosan polymers self-assemble into the network structure with long-range order and high mechanical strength. We hope that with the water-explicit coarse-grained models developed here for lipids, peptides, and polymer, this work could provide an insight for the study of molecular interactions in many biomolecular systems in the future.

4.2 Future Work

Peptide Model. We plan to study what is the role of lipid composition in shaping a peptide aggregation landscape, and which conditions promote or impede a peptide aggregation process (such as surface tension, lipid composition, and lipid-to-peptide ratio). Peptide aggregation on membrane surfaces is another self-assembly process that is relevant to many misfolding diseases, such as Parkinson's, Huntington's and Alzheimer's. The aberrant aggregation of peptides on membrane surfaces is considered to be the pathological agent for the diseases [219, 220]. However, whether the toxic species in the disease is the monomer or the oligomer of $A\beta$ peptides is unclear [221]. Also, the molecular mechanism of peptide aggregation in membraneous surfaces remains to be investigated. Recent studies show that the β-fibrils formed on cellular membrane surfaces damage the integrity of membrane, and the formation of fibrils is dependent on lipid composition [219, 222, 223]. The aggregation of $A\beta$ peptides to form fibrils has been found to depend on membrane curvature and peptide concentrations [224–230]. Charged lipids have been shown to induce β-strand structure for the amyloid beta peptides [221]. Also, the binding of amyloid peptides was also enhanced by lipid phase separation in lipid mixtures [228]. Previously, Caflisch group studied the peptide aggregation process on the surface of coarse-grained (CG) lipid vesicles [231]. They have shown that peptide fibrils damage the structure of membrane and promote leakage [232]. However, Caflisch model is a simplistic model and can not be used to study the relationship between sequence and peptide aggregation, lipid compositions, and hydrogen bonding for-

mation on the aggregation process. Shea et al. have also investigated the effect of surface attraction between a surface and amyloid-like sequences on the aggregation process [233]. In both Caflisch and Shea models, a dihedral potential was applied to force the beta-sheet structure in the peptide [233, 234], therefore factors which experimentally have been observed to impact the aggregation propensities cannot be studied. There are also atomistic simulations on how membrane lipid composition affects the conformational preference and peptide insertion using only a single peptide or preformed fibrils [235–238].

Lipid Model. We plan to investigate the temperature-dependent change of cholesterol absorption rate and how it is related to structural and dynamical changes in lipid nanodomains. Cholesterol is an essential structural component of cellular membranes and plays an important role in modulating many biological functions of cellular membranes [239, 240]. The intestinal absorption of cholesterol has been regarded as a risk factor of coronary heart disease [241]. It is critical for healthy cells to maintain cholesterol homeostasis within and outside the plasma membrane. Cholesterol transfers through lipid membranes also plays a key role in the homeostasis regulation process. The affinity of cholesterol to saturated lipid membrane has been well studied in the past [10, 242–244]. However, little attention has been given to unsaturated lipids that are actually abundant in lipid membranes. Experimental techniques have been employed to study membrane-dependent cholesterol absorption rate on POPC and POPS membranes, and has found an anomalous state of cholesterol transport in PS vesicles but not in PC vesicles. It was reported that the PS membrane cholesterol absorption rate dropped drastically at around

48C°. Since we were able to characterize membrane properties close to experimental observables [209] with our WEPMEM model, we plan to study with this model the relation of the temperature-dependent cholesterol absorption rate to lipid nanodomain formations. The anionic lipid nanodomains in the simulation affects many structural properties of a lipid membrane, such as lipid order, area per lipid, and membrane curvature. It is reasonable to believe that these membrane properties have an effect on lipid-cholesterol interactions.

Chitosan Model. We plan to explore the change of mechanical properties under the effect of pH and salt concentration. In experiments, the ionic concentration is known to affect the viscosity and stiffness of chitosan chains [245]. In addition, it has also been observed that salt concentration also affects structural and dynamical properties of chitosan films formed by electrodeposition [26]. To understand the molecular mechanism of the above-mentioned salt effects on chitosan network formation, we plan to utilize our developed chitosan model and perform a series of simulations with different salt concentrations to see how molecular interactions and structural patterns change.

Bibliography

[1] Siewert J. Marrink, H. Jelger Risselada, Serge Yefimov, D. Peter Tieleman, and Alex H. De Vries. The MARTINI force field: Coarse grained model for biomolecular simulations. *J. Phys. Chem. B*, 111(27):7812–7824, 2007.

[2] John A. Allen, Robyn A. Halverson-Tamboli, and Mark M. Rasenick. Lipid raft microdomains and neurotransmitter signalling. *Nat. Rev. Neurosci.*, 8(2):128–140, 2007.

[3] Linda J. Pike. The challenge of lipid rafts. *J. Lipid Res.*, 50(Supplement):S323–S328, 2009.

[4] Brian A. Tsui-Pierchala, Mario Encinas, Jeffrey Milbrandt, and Eugene M. Johnson. Lipid rafts in neuronal signaling and function. *Trends Neurosci.*, 25(8):412–417, aug 2002.

[5] Andrey S. Shaw. Lipid rafts: Now you see them, now you don't. *Nat. Immunol.*, 7(11):1139–1142, 2006.

[6] Sean Munro. Lipid Rafts: Elusive or Illusive? *Cell*, 115(4):377–388, nov 2003.

[7] Kai Simons and Derek Toomre. Lipid Raft and Signal Transduction. *Nat. Rev. Mol. Cell Biol.*, 1(October):31–39, 2000.

[8] Daniel Lingwood and Kai Simons. Lipid rafts as a membrane-organizing principle. *Science*, 327(5961):46–50, 2010.

[9] Kai Simons and Winchil L.C. Vaz. Model Systems, Lipid Rafts, and Cell Membranes. *Annu. Rev. Biophys. Biomol. Struct.*, 33(1):269–295, 2004.

[10] K Jacobson, O G Mouritsen, and G W Anderson. Lipid rafts: at a crossroad between cell biology and physics. *Nature Cell Biol.*, 9(1):7–14, 2007.

[11] Kai Simons and Mathias J. Gerl. Revitalizing membrane rafts: New tools and insights. *Nat. Rev. Mol. Cell Biol.*, 11(10):688–699, 2010.

[12] A. M. Al-Sabagh, R. E. Morsi, M. Z. Elsabee, H. F. Naguib, and Y. M. Moustafa. Petroleum oil dispersion efficiency and stability using eco-friendly chitosan-based surfactant and nanoparticles. *J. Dispers. Sci. Technol.*, 33(11):1661–1666, 2012.

[13] Haiyue Gong, Yiming Li, Mutai Bao, Dong Lv, and Zhining Wang. Petroleum hydrocarbon degrading bacteria associated with chitosan as effective particle-stabilizers for oil emulsification. *RSC Adv.*, 5(47):37640–37647, 2015.

[14] Jinshu Mao, Liguo Zhao, Kang De Yao, Qingxin Shang, Guanghui Yang, and Yilin Cao. Study of novel chitosan-gelatin artificial skin in vitro. *J. Biomed. Mater. Res. - Part A*, 64(2):301–308, 2003.

[15] Chiung Chi Peng, Ming Hua Yang, Wen Ta Chiu, Chun Hung Chiu, Chi Shen Yang, Yi Wen Chen, Kuan Chou Chen, and Robert Y. Peng. Composite nano-titanium oxide-chitosan artificial skin exhibits strong wound-healing effect - An approach with anti-inflammatory and bactericidal kinetics. *Macromol. Biosci.*, 8(4):316–327, 2008.

[16] Xiaolong Luo, Dean Larios Berlin, Jordan Betz, Gregory F. Payne, William E. Bentley, and Gary W. Rubloff. In situ generation of pH gradients in microfluidic devices for biofabrication of freestanding, semi-permeable chitosan membranes. *Lab Chip*, 10(1):59–65, 2010.

[17] Siewert J. Marrink, Alex H. de Vries, and Alan E. Mark. Coarse grained model for semiquantitative lipid simulations. *J. Phys. Chem. B*, 108(2):750–760, January 2004.

[18] Valentina Tozzini, Joanna Trylska, Chia En Chang, and J. Andrew McCammon. Flap opening dynamics in HIV-1 protease explored with a coarse-grained model. *J. Struct. Biol.*, 157(3):606–615, 2007.

[19] Mario Orsi, David Y. Haubertin, Wendy E. Sanderson, and Jonathan W. Essex. A quantitative coarse-grain model for lipid bilayers. *J. Phys. Chem. B*, 112(3):802–815, 2008.

[20] Paulo F Almeida, Alexey S Ladokhin, and Stephen H White. Hydrogen-bond energetics drive helix formation in membrane interfaces. *Biochim. Biophys. Acta, Biomembr.*, 1818(2):178–182, 2012.

[21] Hyunmin Yi, Li Qun Wu, William E. Bentley, Reza Ghodssi, Gary W. Rubloff, James N. Culver, and Gregory F. Payne. Biofabrication with chitosan. *Biomacromolecules*, 6(6):2881–2894, 2005.

[22] Sang-Dong Jang, Joo-Hyung Kim, Cai Zhijiang, and Jaehwan Kim. The effect of chitosan concentration on the electrical property of chitosan-blended cellulose electroactive paper. *Smart Mater. Struct.*, 18(1):015003, 2009.

[23] Xiaolong Luo, Angela T Lewandowski, Hyunmin Yi, Gregory F Payne, Reza Ghodssi, William E Bentley, and Gary W Rubloff. Programmable assembly of a metabolic pathway enzyme in a pre-packaged reusable bioMEMS device. *Lab on a chip*, 8(3):420–30, 2008.

[24] S T Koev, P H Dykstra, X Luo, G W Rubloff, W E Bentley, G F Payne, and R Ghodssi. Chitosan: an integrative biomaterial for lab-on-a-chip devices. *Lab on a chip*, 10(22):3026–3042, 2010.

[25] Li Qun Wu, Anand P. Gadre, Hyunmin Yi, Mark J. Kastantin, Gary W. Rubloff, William E. Bentley, Gregory F. Payne, and Reza Ghodssi. Voltage-dependent assembly of the polysaccharide chitosan onto an electrode surface. *Langmuir*, 18(22):8620–8625, 2002.

[26] Yi Liu, Boce Zhang, Kelsey M Gray, Yi Cheng, Eunkyoung Kim, Gary W Rubloff, William E Bentley, Qin Wang, and Gregory F Payne. Electrodeposition of a weak polyelectrolyte hydrogel: remarkable effects of salt on kinetics, structure and properties. *Soft Matter*, 9(9):2703–2710, 2013.

[27] Sagar A Pandit, Eric Jakobsson, and H L Scott. Simulation of the early stages of nano-domain formation in mixed bilayers of sphingomyelin, cholesterol, and dioleylphosphatidylcholine. *Biophys. J.*, 87(5):3312–3322, 2004.

[28] Wonpil Im and Charles L Brooks. Interfacial folding and membrane insertion of designed peptides studied by molecular dynamics simulations. *Proc. Natl. Acad. Sci. U. S. A.*, 102(19):6771–6776, 2005.

[29] Eduardo F. Franca, Roberto D. Lins, Luiz C G Freitas, and T. P. Straatsma. Characterization of chitin and chitosan molecular structure in aqueous solution. *J. Chem. Theory Comput.*, 4(12):2141–2149, 2008.

[30] Eduardo F. Franca, Luiz C G Freitas, and Roberto D. Lins. Chitosan molecular structure as a function of N-acetylation. *Biopolymers*, 95(7):448–460, 2011.

[31] Brian H. Morrow, Gregory F. Payne, and Jana Shen. pH-responsive self-assembly of polysaccharide through a rugged energy landscape. *J. Am. Chem. Soc.*, 137(40):13024–13030, 2015.

[32] Steven W. Benner and Carol K. Hall. Development of a Coarse-Grained Model of Chitosan for Predicting Solution Behavior. *J. Phys. Chem. B*, 120(29):7253–7264, 2016.

[33] Steven W. Benner and Carol K. Hall. Effect of monomer sequence and degree of acetylation on the self-assembly and porosity of chitosan networks in solution. *Macromolecules*, 49(14):5281–5290, 2016.

[34] Stephen H. White, Alexey S. Ladokhin, Sajith Jayasinghe, and Kalina Hristova. How membranes shape protein structure. *J. Biol. Chem.*, 276(35):32395–32398, 2001.

[35] Jack Kyte and Russell F. Doolittle. A simple method for displaying the hydropathic character of a protein. *J. Mol. Biol.*, 157(1):105–132, 1982.

[36] Alexey S Ladokhin and Stephen H White. Folding of amphipathic alpha helices on membranes: energetics of helix formation by melittin. *J. Mol. Biol.*, 285(4):1363–1369, 1999.

[37] W C Wimley, K Hristova, A S Ladokhin, L Silvestro, P H Axelsen, and S H White. Folding of beta-sheet membrane proteins: a hydrophobic hexapeptide model. *J. Mol. Biol.*, 277(5):1091–1110, 1998.

[38] Chomdao Sinthuvanich, Ana Salomé Veiga, Kshitij Gupta, Diana Gaspar, Robert Blumenthal, and Joel P. Schneider. Anticancer β-hairpin peptides: Membrane-induced folding triggers activity. *J. Am. Chem. Soc.*, 134(14):6210–6217, 2012.

[39] Ewan M Tytler, GM Anantharamaiah, Donald E Walker, Vinod K Mishra, MN Palgunachari, and Jere P Segrest. Molecular basis for prokaryotic specificity of magainin-induced lysis. *Biochemistry*, 34(13):4393–4401, 1995.

[40] Katsumi Matsuzaki, Kenichi Sugishita, Nobutaka Fujii, and Koichiro Miyajima. Molecular basis for membrane selectivity of an antimicrobial peptide, magainin 2. *Biochemistry*, 34(10):3423–3429, 1995.

[41] Matthew Kirkham and Robert G. Parton. Clathrin-independent endocytosis: New insights into caveolae and non-caveolar lipid raft carriers. *Biochim. Biophys. Acta - Mol. Cell Res.*, 1745(3):273–286, 2005.

[42] D. A. Brown and E. London. Structure and origin of ordered lipid domains in biological membranes. *J. Membr. Biol.*, 164(2):103–114, 1998.

[43] Maria Sovago, George W.H. Wurpel, Marc Smits, Michiel Müller, and Mischa Bonn. Calcium-induced phospholipid ordering depends on surface pressure. *J. Am. Chem. Soc.*, 129(36):11079–11084, 2007.

[44] Helmut Hauser and G. Graham Shipley. Interactions of Monovalent Cations with Phosphatidylserine Bilayer Membranes. *Biochemistry*, 22(9):2171–2178, 1983.

[45] H. Hauser and G. G. Shipley. Crystallization of phosphatidylserine bilayers induced by lithium. *J. Biol. Chem.*, 256(22):11377–11380, 1981.

[46] H. L. Casal, H. H. Mantsch, F. Paltauf, and H. Hauser. Infrared and 31P-NMR studies of the effect of Li^+ and Ca^{2+} on phosphatidylserines. *Biochim. Biophys. Acta, Lipids Lipid Metab.*, 919(3):275–286, 1987.

[47] HL Casal, HH Mantsch, and H Hauser. Infrared studies of fully hydrated saturated phosphatidylserine bilayers. effect of lithium and calcium. *Biochemistry*, 26(14):4408–4416, 1987.

[48] Jairajh Mattai, Helmut Hauser, Rudy A Demel, and G Graham Shipley. Interactions of metal ions with phosphatidylserine bilayer membranes: effect of hydrocarbon chain unsaturation. *Biochemistry*, 28(5):2322–2330, 1989.

[49] M. Roux and M. Bloom. Calcium binding by phosphatidylserine headgroups. Deuterium NMR study. *Biophys. J.*, 60(1):38–44, 1991.

[50] Piotr Jurkiewicz, Lukasz Cwiklik, Alžběta Vojtíšková, Pavel Jungwirth, and Martin Hof. Structure, dynamics, and hydration of POPC/POPS bilayers suspended in NaCl, KCl, and CsCl solutions. *Biochim. Biophys. Acta, Biomembr.*, 1818(3):609–616, 2012.

[51] Anton A Polyansky, Pavel E Volynsky, Dmitry E Nolde, Alexander S Arseniev, and Roman G Efremov. Role of lipid charge in organization of water/lipid bilayer interface: insights via computer simulations. *J. Phys. Chem. B*, 109(31):15052–15059, 2005.

[52] Shirley WI Siu, Robert Vácha, Pavel Jungwirth, and Rainer A Böckmann. Biomolecular simulations of membranes: physical properties from different force fields. *J. Chem. Phys.*, 128(12):125103, 2008.

[53] Liem X Dang, Gregory K Schenter, Vassiliki-Alexandra Glezakou, and John L Fulton. Molecular simulation analysis and x-ray absorption measurement of ca^{2+}, k^{+} and cl^{-} ions in solution. *J. Phys. Chem. B*, 110(47):23644–23654, 2006.

[54] Robert Vácha, Shirley WI Siu, Michal Petrov, Rainer A Böckmann, Justyna Barucha-Kraszewska, Piotr Jurkiewicz, Martin Hof, Max L Berkowitz, and Pavel Jungwirth. Effects of alkali cations and halide anions on the dopc lipid membrane. *J. Phys. Chem. A*, 113(26):7235–7243, 2009.

[55] Felippe J Pavinatto, Luciano Caseli, and Osvaldo N Oliveira. Chitosan in nanostructured thin films. *Biomacromolecules*, 11(8):1897–908, 2010.

[56] Sunil A. Agnihotri, Nadagouda N. Mallikarjuna, and Tejraj M. Aminabhavi. Recent advances on chitosan-based micro- and nanoparticles in drug delivery. *J. Controlled Release*, 100(1):5–28, 2004.

[57] Sania Mansouri, Patrick Lavigne, Karin Corsi, Mohamed Benderdour, Eric Beaumont, and Julio C. Fernandes. Chitosan-DNA nanoparticles as non-viral vectors in gene therapy: Strategies to improve transfection efficacy. *Eur. J. Pharm. Biopharm.*, 57:1–8, 2004.

[58] H. Ueno, T. Mori, and T. Fujinaga. Topical formulations and wound healing applications of chitosan. *Adv. Drug Delivery Rev.*, 52(2):105–115, 2001.

[59] J K Suh and H W Matthew. Application of chitosan-based polysaccharide biomaterials in cartilage tissue engineering: a review. *Biomaterials*, 21(24):2589–2598, 2000.

[60] V. Coma, A. Martial-Gros, S. Garreau, A. Copinet, F. Salin, and A. Deschamps. Edible antimicrobial films based on chitosan matrix. *J. Food Sci.*, 67(3):1162–1169, 2002.

[61] Majeti N.V Ravi Kumar. A review of chitin and chitosan applications. *React. Funct. Polym.*, 46(1):1–27, 2000.

[62] Sundararajan V. Madihally and Howard W T Matthew. Porous chitosan scaffolds for tissue engineering. *Biomaterials*, 20(November 1998):1133–1142, 1999.

[63] Alberto Di Martino, Michael Sittinger, and Makarand V. Risbud. Chitosan: A versatile biopolymer for orthopaedic tissue-engineering. *Biomaterials*, 26(30):5983–5990, 2005.

[64] Dana L Nettles, Steven H Elder, and Jerome a Gilbert. Potential use of chitosan as a cell scaffold material for cartilage tissue engineering. *Tissue Eng.*, 8(6):1009–1016, 2002.

[65] Jianbiao Ma, Hongjun Wang, Binglin He, and Jiatong Chen. A preliminary in vitro study on the fabrication and tissue engineering applications of a novel chitosan bilayer material as a scaffold of human neofetal dermal fibroblasts. *Biomaterials*, 22(4):331–336, 2001.

[66] Marguerite Rinaudo. Chitin and chitosan: Properties and applications. *Prog. Polym. Sci.*, 31(7):603–632, 2006.

[67] Gregory F. Payne and Srinivasa R. Raghavan. Chitosan: a soft interconnect for hierarchical assembly of nano-scale components. *Soft Matter*, 3(5):521, 2007.

[68] Joel Brugnerotto, Jacques Desbrières, George Roberts, and Marguerite Rinaudo. Characterization of chitosan by steric exclusion chromatography. *Polymer*, 42(25):9921–9927, 2001.

[69] Christophe Schatz, Christophe Viton, Thierry Delair, Christian Pichot, and Alain Domard. Typical physicochemical behaviors of chitosan in aqueous solution. *Biomacromolecules*, 4(3):641–648, 2003.

[70] Guillaume Lamarque, Jean Michel Lucas, Christophe Viton, and Alain Domard. Physicochemical behavior of homogeneous series of acetylated chitosans in aqueous solution: Role of various structural parameters. *Biomacromolecules*, 6(1):131–142, 2005.

[71] J Brugnerotto, J Desbrieres, L Heux, K Mazeau, and M Rinaudo. Overview on structural characterization of chitosan molecules in relation with their behavior in solution. *Macromol. Symp.*, 168:1–20, 2001.

[72] Kozo Ogawa, Toshifumi Yui, and Kenji Okuyama. Three D structures of chitosan. *Int. J. Biol. Macromol.*, 34(1-2):1–8, 2004.

[73] K. Okuyama, K. Noguchi, M. Kanenari, T. Egawa, K. Osawa, and K. Ogawa. Structural diversity of chitosan and its complexes. *Carbohydr. Polym.*, 41(3):237–248, 2000.

[74] Amornrat Lertworasirikul, Shingo Yokoyama, Keiichi Noguchi, Kozo Ogawa, and Kenji Okuyama. Molecular and crystal structures of chitosan/HI type I salt determined by X-ray fiber diffraction. *Carbohydr. Res.*, 339(4):825–833, 2004.

[75] Toshifumi Yui, Kiyohisa Imada, Kenji Okuyama, Yutaka Obata, Katsumi Suzuki, and Kozo Ogawa. Molecular and crystal structure of the anhydrous form of chitosan. *Macromolecules*, 27(26):7601–7605, 1994.

[76] Kenji Okuyama, Keiichi Noguchi, Takashi Miyazawa, Toshifumi Yui, and Kozo Ogawa. Molecular and Crystal Structure of Hydrated Chitosan. *Macromolecules*, 30(19):5849–5855, 1997.

[77] M. Ray, K. Pal, A. Anis, and a. K. Banthia. Development and characterization of chitosan-based polymeric hydrogel membranes. *Des. Monomers Polym.*, 13(3):193–206, 2010.

[78] Tooru Kitagawa and Kazuyuki Yabuki. Physical properties of silk fibroin/chitosan blend films. *J. Appl. Polym. Sci.*, 80(7):928–934, 2001.

[79] M. N. Khalid, F. Agnely, N. Yagoubi, J. L. Grossiord, and G. Couarraze. Water state characterization, swelling behavior, thermal and mechanical properties of chitosan based networks. *Eur. J. Pharm. Sci.*, 15(5):425–432, 2002.

[80] A. Martinez-Ruvalcaba, E. Chornet, and D. Rodrigue. Viscoelastic properties of dispersed chitosan/xanthan hydrogels. *Carbohydr. Polym.*, 67(4):586–595, 2007.

[81] Karim Mazeau, Serge Pérez, and Marguerite Rinaudo. Predicted Influence of N-Acetyl Group Content on the Conformational Extension of Chitin and Chitosan Chains. *J. Carbohydr. Chem.*, 19(9):1269–1284, 2000.

[82] X L Luo, S Buckhout-White, W E Bentley, and G W Rubloff. Biofabrication of chitosan-silver composite SERS substrates enabling quantification of adenine by a spectroscopic shift. *Biofabrication*, 3(3):034108, 2011.

[83] Richard A Cunha, Thereza A Soares, Victor H Rusu, Frederico J S Pontes, Eduardo F Franca, and Roberto D Lins. *The Molecular Structure and Conformational Dynamics of Chitosan Polymers : An Integrated Perspective from Experiments and Computational Simulations*. 2012.

[84] Yingzhe Liu, Christophe Chipot, Xueguang Shao, and Wensheng Cai. Free-energy landscape of the helical wrapping of a carbon nanotube by a polysaccharide. *J. Phys. Chem. C*, 115(5):1851–1856, 2011.

[85] Cesar A. López, Andrzej J. Rzepiela, Alex H. de Vries, Lubbert Dijkhuizen, Philippe H. Hünenberger, and Siewert J. Marrink. Martini coarse-grained force field: Extension to carbohydrates. *J. Chem. Theory Comput.*, 5(12):3195–3210, 2009.

[86] Goundla Srinivas, Xiaolin Cheng, and Jeremy C. Smith. A solvent-free coarse grain model for crystalline and amorphous cellulose fibrils. *J. Chem. Theory Comput.*, 7(8):2539–2548, 2011.

[87] Antti Pekka Hynninen, James F. Matthews, Gregg T. Beckham, Michael F. Crowley, and Mark R. Nimlos. Coarse-grain model for glucose, cellobiose, and cellotetraose in water. *J. Chem. Theory Comput.*, 7(7):2137–2150, 2011.

[88] Berk Hess, Carsen Kutzner, David Van Der Spoel, and Erik Lindahl. Gromacs 4: Algorithms for highly efficient, load-balanced, and scalable molecular simulation. *J. Chem. Theory Comput.*, 4(3):435–447, 2008.

[89] Steve Plimpton. Fast parallel algorithms for short-range molecular dynamics. *J. Comput. Phys.*, 117:1–19, 1995.

[90] Semen O Yesylevskyy, Lars V Schäfer, Durba Sengupta, and Siewert J Marrink. Polarizable water model for the coarse-grained MARTINI force field. *PLoS Comput. Biol.*, 6(6):e1000810, June 2010.

[91] Laercio Pol-Fachin, Victor H. Rusu, Hugo Verli, and Roberto D. Lins. GROMOS 53A6GLYC, an improved GROMOS force field for hexopyranose-based carbohydrates. *J. Chem. Theory Comput.*, 2012.

[92] R. W. Hockney, S. P. Goel, and J. W. Eastwood. Quiet high-resolution computer models of a plasma. *J. Comput. Phys.*, 14(2):148–158, 1974.

[93] H J C Berendsen, J P M Postma, W F van Gunsteren, a DiNola, and J R Haak. Molecular dynamics with coupling to an external bath. *J. Chem. Phys.*, 81(March 2014):3684–3690, 1984.

[94] René Sperb, Ilario G. Tironi, Ilario G. Tironi, Ren\'e Sperb, Paul E. Smith, Paul E. Smith, Wilfred F. Van Gunsteren, and Wilfred F. Van Gunsteren. A generalized reaction field method for molecular dynamics simulations. *J. Chem. Phys.*, 102(13):5451–5459, 1995.

[95] Shuichi Nosé. A unified formulation of the constant temperature molecular dynamics methods. *J. Chem. Phys.*, 81(1):511–519, 1984.

[96] William Hoover. Canonical dynamics: Equilibrium phase-space distributions. *Phys. Rev. A*, 31(3):1695–1697, 1985.

[97] M. Parrinello and A. Rahman. Polymorphic transitions in single crystals: A new molecular dynamics method. *J. Appl. Phys.*, 52:7182–7190, 1981.

[98] Tom Darden, Darrin York, and Lee Pedersen. Particle mesh Ewald: An N log(N) method for Ewald sums in large systems. *J. Chem. Phys.*, 98(12):10089–10092, 1993.

[99] Ulrich Essmann, Lalith Perera, Max L Berkowitz, Tom Darden, Hsing Lee, and Lee G Pedersen. A smooth particle mesh Ewald method. *J. Chem. Phys.*, 103(1995):8577–8593, 1995.

[100] Berk Hess, Henk Bekker, Herman JC Berendsen, and Johannes G. E. M. Fraaije. LINCS: a linear constraint solver for molecular simulations. *J. Comput. Chem.*, 18(12):1463–1472, 1997.

[101] William C Swope. A computer simulation method for the calculation of equilibrium constants for the formation of physical clusters of molecules: Application to small water clusters. *J. Chem. Phys.*, 76(1):637, 1982.

[102] R. W. Hockney and J. W. Eastwood. *Computer Simulation Using Particles*, volume 25. CRC Press, 1983.

[103] Jean Paul Ryckaert, Giovanni Ciccotti, and Herman J C Berendsen. Numerical integration of the cartesian equations of motion of a system with constraints: molecular dynamics of n-alkanes. *J. Comput. Phys.*, 23(3):327–341, 1977.

[104] Hans C. Andersen. Rattle: A "velocity" version of the shake algorithm for molecular dynamics calculations. *J. Comput. Phys.*, 52(1):24–34, 1983.

[105] Thomas F. Willems, Chris H. Rycroft, Michaeel Kazi, Juan C. Meza, and MacIej Haranczyk. Algorithms and tools for high-throughput geometry-based analysis of crystalline porous materials. *Microporous Mesoporous Mater.*, 149(1):134–141, 2012.

[106] Mohammed Aider. Chitosan application for active bio-based films production and potential in the food industry: Review. *LWT – Food Sci. Technol.*, 43(6):837–842, 2010.

[107] A. Borzacchiello, L. Ambrosio, P. A. Netti, L. Nicolais, C. Peniche, A. Gallardo, and J. San Roman. Chitosan-based hydrogels: Synthesis and characterization. *J. Mater. Sci. Mater. Med.*, 12(10-12):861–864, 2001.

[108] Yi Hong, Haiqing Song, Yihong Gong, Zhengwei Mao, Changyou Gao, and Jiacong Shen. Covalently crosslinked chitosan hydrogel: Properties of in vitro degradation and chondrocyte encapsulation. *Acta Biomater.*, 3(1):23–31, 2007.

[109] Mi Seon Shin, Seon Jeong Kim, Sang Jun Park, Yong Hee Lee, and Sun I. Kim. Synthesis and characteristics of the interpenetrating polymer network hydrogel composed of chitosan and polyallylamine. *J. Appl. Polym. Sci.*, 86(2):498–503, 2002.

[110] K D Yao, W G Liu, Z Lin, and X H Qiu. In situ atomic force microscopy measurement of the dynamic variation in the elastic modulus of swollen chitosan/gelatin hybrid polymer network gels in media of different pH. *Polym. Int.*, 48(9):794–798, 1999.

[111] A Chenite, C Chaput, D Wang, C Combes, M.D Buschmann, C.D Hoemann, J.C Leroux, B.L Atkinson, F Binette, and A Selmani. Novel injectable neutral solutions of chitosan form biodegradable gels in situ. *Biomaterials*, 21(21):2155–2161, 2000.

[112] Peter A Leventis and Sergio Grinstein. The distribution and function of phosphatidylserine in cellular membranes. *Annu. Rev. Biophys.*, 39:407–27, January 2010.

[113] Jens Schamberger and Ronald J Clarke. Hydrophobic ion hydration and the magnitude of the dipole potential. *Biophys. J.*, 82(6):3081–3088, 2002.

[114] V. M. Aguilella and S. M. Bezrukov. Alamethicin channel conductance modified by lipid charge. *Eur. Biophys. J.*, 30(4):233–241, 2001.

[115] Stephen H. White, Alexey S. Ladokhin, Sajith Jayasinghe, and Kalina Hristova. How membranes shape protein structure. *J. Biol. Chem.*, 276(35):32395–32398, 2001.

[116] William C Wimley and Stephen H White. Experimentally determined hydrophobicity scale for proteins at membrane interfaces. *Nat. Struct. Mol. Biol.*, 3(10):842–848, 1996.

[117] Edit Matyus, Christian Kandt, and D Peter Tieleman. Computer simulation of antimicrobial peptides. *Curr. Med. Chem.*, 14(26):2789–2798, 2007.

[118] Dejun Lin and Alan Grossfield. Thermodynamics of antimicrobial lipopeptide binding to membranes: origins of affinity and selectivity. *Biophys. J.*, 107(8):1862–1872, 2014.

[119] Dorit Avrahami and Yechiel Shai. Conjugation of a magainin analogue with lipophilic acids controls hydrophobicity, solution assembly, and cell selectivity. *Biochemistry*, 41(7):2254–2263, 2002.

[120] E Gazit, I R Miller, P C Biggin, M S Sansom, and Y Shai. Structure and orientation of the mammalian antibacterial peptide cecropin P1 within phospholipid membranes. *J. Mol. Biol.*, 258(5):860–870, 1996.

[121] P. J Hoogerbrugge and J. M. V. A Koelman. Simulating microscopic hydrodynamic phenomena with dissipative particle dynamics. *Europhys. Lett.*, 19(3):155–160, 2007.

[122] Rustam Z Khaliullin and Thomas D Kühne. Microscopic properties of liquid water from combined ab initio molecular dynamics and energy decomposition studies. *Phys. Chem. Chem. Phys.*, 15(38):15746–66, 2013.

[123] Wei Zhao, Tomasz Róg, Andrey A Gurtovenko, Ilpo Vattulainen, and Mikko Karttunen. Atomic-scale structure and electrostatics of anionic palmitoyloleoylphosphatidylglycerol lipid bilayers with Na^+ counterions. *Biophys. J.*, 92(4):1114–24, February 2007.

[124] Alberto Martín-Molina, César Rodríguez-Beas, and Jordi Faraudo. Effect of calcium and magnesium on phosphatidylserine membranes: experiments and all-atomic simulations. *Biophys. J.*, 102(9):2095–103, May 2012.

[125] Jianjun Pan, Xiaolin Cheng, Luca Monticelli, Frederick A Heberle, Norbert Kučerka, D Peter Tieleman, and John Katsaras. The molecular structure of a phosphatidylserine bilayer determined by scattering and molecular dynamics simulations. *Soft Matter*, 10(21):3716–25, June 2014.

[126] Jonathan N Sachs, Hirsh Nanda, Horia I Petrache, and Thomas B Woolf. Changes in phosphatidylcholine headgroup tilt and water order induced by monovalent salts: molecular dynamics simulations. *Biophys. J.*, 86(6):3772–82, June 2004.

[127] Sagar A Pandit and Max L Berkowitz. Molecular dynamics simulation of dipalmitoylphosphatidylserine bilayer with Na^+ counterions. *Biophys. J.*, 82(4):1818–27, April 2002.

[128] John M. Boettcher, Rebecca L. Davis-Harrison, Mary C. Clay, Andrew J. Nieuwkoop, Y. Zenmei Ohkubo, Emad Tajkhorshid, James H. Morrissey, and Chad M. Rienstra. Atomic view of calcium-induced clustering of phosphatidylserine in mixed lipid bilayers. *Biochemistry*, 50(12):2264–2273, 2011.

[129] Parag Mukhopadhyay, Luca Monticelli, and D Peter Tieleman. Molecular dynamics simulation of a palmitoyl-oleoyl phosphatidylserine bilayer with Na^+ counterions and NaCl. *Biophys. J.*, 86(3):1601–1609, 2004.

[130] Sun-Joo Lee, Yuhua Song, and Nathan A Baker. Molecular dynamics simulations of asymmetric NaCl and KCl solutions separated by phosphatidylcholine bilayers: potential drops and structural changes induced by strong Na^+-lipid interactions and finite size effects. *Biophys. J.*, 94(9):3565–3576, 2008.

[131] Manuela Menke, Volker Gerke, and Claudia Steinem. Phosphatidylserine membrane domain clustering induced by annexin A2/S100A10 heterotetramer. *Biochemistry*, 44(46):15296–15303, 2005.

[132] Maddalena Venturoli, Maria Maddalena Sperotto, Marieke Kranenburg, and Berend Smit. Mesoscopic models of biological membranes. *Phys. Rep.*, 437(1-2):1–54, 2006.

[133] Qaiser Waheed, Richard Tjörnhammar, and Olle Edholm. Phase transitions in coarse-grained lipid bilayers containing cholesterol by molecular dynamics simulations. *Biophys. J.*, 103(10):2125–2133, 2012.

[134] H Jelger Risselada and Siewert J Marrink. The molecular face of lipid rafts in model membranes. *Proc. Natl. Acad. Sci. U. S. A.*, 105(45):17367–17372, 2008.

[135] Mark J. Stevens. Coarse-grained simulations of lipid bilayers. *J. Chem. Phys.*, 121(23):11942–11948, 2004.

[136] Zun-Jing Wang and Markus Deserno. Systematic implicit solvent coarse-graining of bilayer membranes: lipid and phase transferability of the force field. *New J. Phys.*, 12(9):095004, 2010.

[137] Emily M Curtis and Carol K Hall. Molecular dynamics simulations of dppc bilayers using "lime", a new coarse-grained model. *J. Phys. Chem. B*, 117(17):5019–5030, 2013.

[138] Carlos F. Lopez, Steven O. Nielsen, Goundla Srinivas, William F. DeGrado, and Michael L. Klein. Probing membrane insertion activity of antimicrobial polymers via coarse-grain molecular dynamics. *J. Chem. Theory Comput.*, 2(3):649–655, 2006.

[139] L Monticelli, S K Kandasamy, X Periole, R G Larson, D P Tieleman, and S J Marrink. The MARTINI coarse grained force field: extension to proteins. *J. Chem. Theory Comput.*, 4:819–834, 2008.

[140] Sai J. Ganesan and S. Matysiak. Role of backbone dipole interactions in the formation of secondary and supersecondary structures of proteins. *J. Chem. Theory Comput.*, 10(6):2569–2576, 2014.

[141] Pavel A. Golubkov and Pengyu Ren. Generalized coarse-grained model based on point multipole and Gay-Berne potentials. *J. Chem. Phys.*, 125(6), 2006.

[142] Pavel A Golubkov, Johnny C Wu, and Pengyu Ren. A transferable coarse-grained model for hydrogen-bonding liquids. *Phys. Chem. Chem. Phys.*, 10(15):2050–2057, 2008.

[143] Johnny Wu, Xia Zhen, Hujun Shen, Guohui Li, and Pengyu Ren. Gay-Berne and electrostatic multipole based coarse-grain potential in implicit solvent. *J. Chem. Phys.*, 135(15), 2011.

[144] Diana Gaspar, Ana Salomé Veiga, Chomdao Sinthuvanich, Joel P. Schneider, and Miguel A R B Castanho. Anticancer peptide SVS-1: Efficacy precedes membrane neutralization. *Biochemistry*, 51(32):6263–6265, 2012.

[145] Kshitij Gupta, Hyunbum Jang, Kevin Harlen, Anu Puri, Ruth Nussinov, Joel P. Schneider, and Robert Blumenthal. Mechanism of membrane permeation induced by synthetic β-hairpin peptides. *Biophys. J.*, 105(9):2093–2103, 2013.

[146] Bernard R. Brooks, Robert E. Bruccoleri, Barry D. Olafson, David J. States, S. Swaminathan, and Martin Karplus. CHARMM: A program for macromolecular energy, minimization, and dynamics calculations. *J. Comput. Chem.*, 4(2):187–217, 1983.

[147] Giovanni Bellesia, Andrew Iain Jewett, and Joan Emma Shea. Sequence periodicity and secondary structure propensity in model proteins. *Protein Sci.*, 19(1):141–154, 2010.

[148] William Humphrey, Andrew Dalke, and Klaus Schulten. VMD: Visual molecular dynamics. *J. Mol. Graphics*, 14(1):33–38, 1996.

[149] Chris Oostenbrink, Alessandra Villa, Lan Mark, and Wilfred Van Gunsteren. A biomolecular force field based on the free enthalpy of hydration and solvation: The GROMOS force-field parameter sets 53A5 and 53A6. *J. Comput. Chem.*, 25:1656–1676, 2004.

[150] Ryogo Kubo, Mario Yokota, and Sadao Nakajima. Statistical-mechanical theory of irreversible processes. II. Response to thermal disturbance. *J. Phys. Soc. Jpn.*, 12(11):1203–1211, 1957.

[151] Frank Y Jiang, Yann Bouret, and James T Kindt. Molecular dynamics simulations of the lipid bilayer edge. *Biophys. J.*, 87(1):182–192, 2004.

[152] Aric A. Hagberg, Daniel A. Schult, and Pieter J. Swart. Exploring network structure, dynamics, and function using NetworkX. In *Proceedings of the 7th Python in Science Conference (SciPy2008)*, pages 11–15, Pasadena, CA USA, August 2008.

[153] Alenka Luzar and David Chandler. Hydrogen-bond kinetics in liquid water. *Nature*, 379(6560):55–57, 1996.

[154] Andrey A. Gurtovenko and Ilpo Vattulainen. Membrane potential and electrostatics of phospholipid bilayers with asymmetric transmembrane distribution of anionic lipids. *J. Phys. Chem. B*, 112(15):4629–4634, 2008.

[155] G Cevc, A Watts, and D Marsh. Titration of the phase transition of phosphatidylserine bilayer membranes. Effects of pH, surface electrostatics, ion binding, and head-group hydration. *Biochemistry*, 20(17):4955–4965, 1981.

[156] Norbert Kučerka, Mu Ping Nieh, and John Katsaras. Fluid phase lipid areas and bilayer thicknesses of commonly used phosphatidylcholines as a function of temperature. *Biochim. Biophys. Acta, Biomembr.*, 1808(11):2761–2771, 2011.

[157] Norbert Kučerka, Yufeng Liu, Nanjun Chu, Horia I. Petrache, Stephanie Tristram-Nagle, and John F. Nagle. Structure of fully hydrated fluid phase DMPC and DLPC lipid bilayers using X-ray scattering from oriented multilamellar arrays and from unilamellar vesicles. *Biophys. J.*, 88(4):2626–2637, 2005.

[158] B König, U Dietrich, and G Klose. Hydration and structural properties of mixed lipid/surfactant model membranes. *Langmuir*, 13(3):525–532, 1997.

[159] J M Smaby, M M Momsen, H L Brockman, and R E Brown. Phosphatidylcholine acyl unsaturation modulates the decrease in interfacial elasticity induced by cholesterol. *Biophys. J.*, 73(3):1492–1505, 1997.

[160] Jussi Aittoniemi, Perttu S Niemelä, Marja T Hyvönen, Mikko Karttunen, and Ilpo Vattulainen. Insight into the putative specific interactions between cholesterol, sphingomyelin, and palmitoyl-oleoyl phosphatidylcholine. *Biophys. J.*, 92(4):1125–1137, 2007.

[161] Rainer A Böckmann, Agnieszka Hac, Thomas Heimburg, and Helmut Grubmüller. Effect of sodium chloride on a lipid bilayer. *Biophys. J.*, 85(3):1647–1655, 2003.

[162] Richard M Venable, Yun Luo, Klaus Gawrisch, Benoît Roux, and Richard W Pastor. Simulations of anionic lipid membranes: Development of interaction-specific ion parameters and validation using nmr data. *J. Phys. Chem. B*, 117(35):10183–10192, 2013.

[163] Ji-Xin Cheng, Sophie Pautot, David A Weitz, and X Sunney Xie. Ordering of water molecules between phospholipid bilayers visualized by coherent anti-stokes raman scattering microscopy. *Proc. Natl. Acad. Sci. U. S. A.*, 100(17):9826–9830, 2003.

[164] S J Slater, C Ho, F J Taddeo, M B Kelly, and C D Stubbs. Contribution of hydrogen bonding to lipid-lipid interactions in membranes and the role of lipid order: effects of cholesterol, increased phospholipid unsaturation, and ethanol. *Biochemistry*, 32(14):3714–3721, 1993.

[165] D. V. Zhelev and D. Needham. Tension-stabilized pores in giant vesicles: Determination of pore size and pore line tension. *Biochim. Biophys. Acta, Biomembr.*, 1147(1):89–104, 1993.

[166] Erdem Karatekin, Olivier Sandre, Hicham Guitouni, Nicolas Borghi, Pierre-Henri Puech, and Françoise Brochard-Wyart. Cascades of transient pores in giant vesicles: line tension and transport. *Biophys. J.*, 84(3):1734–1749, 2003.

[167] Satwik Kamtekar, Jarad M Schiffer, Huayu Xiong, Jennifer M Babik, and Michael H Hecht. Protein design by binary patterning of polar and nonpolar amino acids. *Science*, 262(5140):1680–1685, 1993.

[168] Yechiel Shai. Mechanism of the binding, insertion and destabilization of phospholipid bilayer membranes by α-helical antimicrobial and cell non-selective membrane-lytic peptides. *Biochim. Biophys. Acta, Biomembr.*, 1462(1):55–70, 1999.

[169] Stephen H White and William C Wimley. Membrane protein folding and stability: physical principles. *Annu. Rev. Biophys. Biomol. Struct.*, 28(1):319–365, 1999.

[170] Hiromi Sato and Jimmy B Feix. Peptide–membrane interactions and mechanisms of membrane destruction by amphipathic α-helical antimicrobial peptides. *Biochim. Biophys. Acta, Biomembr.*, 1758(9):1245–1256, 2006.

[171] Yuji Ishitsuka, Duy S Pham, Alan J Waring, Robert I Lehrer, and Ka Yee C Lee. Insertion selectivity of antimicrobial peptide protegrin-1 into lipid monolayers: effect of head group electrostatics and tail group packing. *Biochim. Biophys. Acta, Biomembr.*, 1758(9):1450–1460, 2006.

[172] Themis Lazaridis, Yi He, and Lidia Prieto. Membrane interactions and pore formation by the antimicrobial peptide protegrin. *Biophys. J.*, 104(3):633–642, 2013.

[173] Ayyalusamy Ramamoorthy, Sathiah Thennarasu, Anmin Tan, Kiran Gottipati, Sreeja Sreekumar, Deborah L Heyl, Florence YP An, and Charles E Shelburne. Deletion of all cysteines in tachyplesin I abolishes hemolytic activity and retains antimicrobial activity and lipopolysaccharide selective binding. *Biochemistry*, 45(20):6529–6540, 2006.

[174] Henry D Herce and Angel E Garcia. Molecular dynamics simulations suggest a mechanism for translocation of the hiv-1 tat peptide across lipid membranes. *Proc. Natl. Acad. Sci. USA*, 104(52):20805–20810, 2007.

[175] Semen Yesylevskyy, Siewert-Jan Marrink, and Alan E Mark. Alternative mechanisms for the interaction of the cell-penetrating peptides penetratin and the tat peptide with lipid bilayers. *Biophys. J.*, 97(1):40–49, 2009.

[176] Shuhei Kawamoto, Masako Takasu, Takeshi Miyakawa, Ryota Morikawa, Tatsuki Oda, Shiroh Futaki, and Hidemi Nagao. Binding of tat peptides on dopc and dopg lipid bilayer membrane studied by molecular dynamics simulations. *Mol. Simul.*, 38(5):366–368, 2012.

[177] Kiyotaka Akabori, Kun Huang, Bradley W Treece, Michael S Jablin, Brian Maranville, Arthur Woll, John F Nagle, Angel E Garcia, and Stephanie Tristram-Nagle. Hiv-1 tat membrane interactions probed using x-ray and neutron scattering, cd spectroscopy and md simulations. *Biochim. Biophys. Acta, Biomembr.*, 1838(12):3078–3087, 2014.

[178] Zhe Wu, Qiang Cui, and Arun Yethiraj. A new coarse-grained model for water: the importance of electrostatic interactions. *J. Phys. Chem. B*, 114(32):10524–10529, 2010.

[179] H-L Lee, EA Dubikovskaya, H Hwang, AN Semyonov, H Wang, LR Jones, RJ Twieg, WE Moerner, and PA Wender. Single-molecule motions of oligoarginine transporter conjugates on the plasma membrane of chinese hamster ovary cells. *J. Am. Chem. Soc.*, 130(29):9364–9370, 2008.

[180] Zdzislaw Salamon, Göran Lindblom, and Gordon Tollin. Plasmon-waveguide resonance and impedance spectroscopy studies of the interaction between penetratin and supported lipid bilayer membranes. *Biophys. J.*, 84(3):1796–1807, 2003.

[181] Justin L MacCallum, WF Drew Bennett, and D Peter Tieleman. Distribution of amino acids in a lipid bilayer from computer simulations. *Biophys. J.*, 94(9):3393–3404, 2008.

[182] Donald M Engelman. Membranes are more mosaic than fluid. *Nature*, 438(7068):578–580, 2005.

[183] Saame Raza Shaikh, Alfred C Dumaual, Laura J Jenski, and William Stillwell. Lipid phase separation in phospholipid bilayers and monolayers modeling the plasma membrane. *Biochim. Biophys. Acta, Biomembr.*, 1512(2):317–328, 2001.

[184] Elliot L Elson, Eliot Fried, John E Dolbow, and Guy M Genin. Phase separation in biological membranes: integration of theory and experiment. *Annu. Rev. Biophys.*, 39:207, 2010.

[185] Helgi I Ingolfsson, Peter Tieleman, and Siewert Marrink. Lipid organization of the plasma membrane. *Biophys. J.*, 108(2):358a, 2015.

[186] Mary L Kraft. Plasma membrane organization and function: moving past lipid rafts. *Mol. Biol. Cell*, 24(18):2765–2768, 2013.

[187] S Sonnino and A Prinetti. Membrane domains and the "lipid raft" concept. *Curr. Med. Chem.*, 20(1):4–21, 2013.

[188] Erwin London. Insights into lipid raft structure and formation from experiments in model membranes. *Curr. Opin. Struct. Biol.*, 12(4):480–486, 2002.

[189] Jiang Zhao, Jing Wu, Frederick A Heberle, Thalia T Mills, Paul Klawitter, Grace Huang, Greg Costanza, and Gerald W Feigenson. Phase studies of model biomembranes: complex behavior of dspc/dopc/cholesterol. *Biochim. Biophys. Acta, Biomembr.*, 1768(11):2764–2776, 2007.

[190] Jason D. Perlmutter and Jonathan N. Sachs. Interleaflet interaction and asymmetry in phase separated lipid bilayers: molecular dynamics simulations. *J. Am. Chem. Soc.*, 133(17):6563–6577, 2011.

[191] Davit Hakobyan and Andreas Heuer. Phase separation in a lipid/cholesterol system: comparison of coarse-grained and united-atom simulations. *J. Phys. Chem. B*, 117(14):3841–3851, 2013.

[192] Hans Binder and Olaf Zschörnig. The effect of metal cations on the phase behavior and hydration characteristics of phospholipid membranes. *Chem. Phys. Lipids*, 115(1):39–61, 2002.

[193] Michel Roux and Myer Bloom. Calcium, magnesium, lithium, sodium, and potassium distributions in the headgroup region of binary membranes of phosphatidylcholine and phosphatidylserine as seen by deuterium nmr. *Biochemistry*, 29(30):7077–7089, 1990.

[194] The NMRlipids project. accessed Dec 10, 2016.

[195] Lubos Vrbka, Martin Mucha, Babak Minofar, Pavel Jungwirth, Eric C. Brown, and Douglas J. Tobias. Propensity of soft ions for the air/water interface. *Curr. Opin. Colloid Interface Sci.*, 9(1-2):67–73, 2004.

[196] Lalith Perera and Max L. Berkowitz. Many-body effects in molecular dynamics simulations of $Na^+(H_2O)$n and $Cl(H_2O)$n clusters. *J. Chem. Phys.*, 95(3):1954–1963, 1991.

[197] Alan Grossfield, Pengyu Ren, and Jay W. Ponder. Ion solvation thermodynamics from simulation with a polarizable force field. *J. Am. Chem. Soc.*, 125(50):15671–15682, 2003.

[198] Guillaume Lamoureux and Benoît Roux. Absolute hydration free energy scale for alkali and halide ions established from simulations with a polarizable force field. *J. Phys. Chem. B*, 110(7):3308–3322, 2006.

[199] Denis Bucher, Leonardo Guidoni, Patrick Maurer, and Ursula Rothlisberger. Developing improved charge sets for the modeling of the KcsA K^+ channel using QM/MM electrostatic potentials. *J. Chem. Theory Comput.*, 5(8):2173–2179, 2009.

[200] T. W. Allen, O. S. Andersen, and B. Roux. Ion permeation through a narrow channel: using gramicidin to ascertain all-atom molecular dynamics potential of mean force methodology and biomolecular force fields. *Biophys. J.*, 90(10):3447–68, 2006.

[201] Benoît Roux. Non-additivity in cation-peptide interactions. A molecular dynamics and ab initio study of Na^+ in the gramicidin channel. *Chem. Phys. Lett.*, 212(3-4):231–240, 1993.

[202] Janamejaya Chowdhary, Edward Harder, Pedro EM Lopes, Lei Huang, Alexander D MacKerell Jr, and Benoît Roux. A polarizable force field of dipalmitoylphosphatidylcholine based on the classical drude model for molecular dynamics simulations of lipids. *J. Phys. Chem. B*, 117(31):9142–9160, 2013.

[203] Emily M Curtis, Xingqing Xiao, Stavroula Sofou, and Carol K Hall. Phase separation behavior of mixed lipid systems at neutral and low pH: coarse-grained simulations with DMD/LIME. *Langmuir*, 31(3):1086–1094, 2015.

[204] Martin Dahlberg and Arnold Maliniak. Mechanical properties of coarse-grained bilayers formed by cardiolipin and zwitterionic lipids. *J. Chem. Theory Comput.*, 6(5):1638–1649, 2010.

[205] Anne Hinderliter, Paulo FF Almeida, Carl E Creutz, and Rodney L Biltonen. Domain formation in a fluid mixed lipid bilayer modulated through binding of the c2 protein motif. *Biochemistry*, 40(13):4181–4191, 2001.

[206] Anne Hinderliter, Rodney L Biltonen, and Paulo FF Almeida. Lipid modulation of protein-induced membrane domains as a mechanism for controlling signal transduction. *Biochemistry*, 43(22):7102–7110, 2004.

[207] J Huang, J E Swanson, a R Dibble, a K Hinderliter, and G W Feigenson. Nonideal mixing of phosphatidylserine and phosphatidylcholine in the fluid lamellar phase. *Biophys. J.*, 64(2):413–425, 1993.

[208] Hee Yong Kim, Bill X. Huang, and Arthur A. Spector. Phosphatidylserine in the brain: Metabolism and function. *Prog. Lipid Res.*, 56(1):1–18, 2014.

[209] Sai J. Ganesan, Hongcheng Xu, and Silvina Matysiak. Effect of lipid head group interactions on membrane properties and membrane-induced cationic β-hairpin folding. *Phys. Chem. Chem. Phys.*, 2016.

[210] Stefan Obst and Hans Bradaczek. Molecular dynamics study of the structure and dynamics of the hydration shell of alkaline and alkaline-earth metal cations. *J. Phys. Chem.*, 100(39):15677–15687, 1996.

[211] Giner Casares, Juan José, Luis Camacho, Maria Teresa Martín-Romero, and José Javier López Cascales. Effect of Na^+ and Ca^{2+} ions on a lipid Langmuir monolayer: an atomistic description by molecular dynamics simulations. *Chem. Phys. Chem.*, 9(17):2538–2543, 2008.

[212] Cornelia G. Sinn, Markus Antonietti, and Rumiana Dimova. Binding of calcium to phosphatidylcholine-phosphatidylserine membranes. *Colloids Surf., A*, 282-283:410–419, 2006.

[213] Cheng Y Tang, Zishuai Huang, and Heather C Allen. Interfacial water structure and effects of Mg^{2+} and Ca^{2+} binding to the COOH headgroup of a palmitic acid monolayer studied by sum frequency spectroscopy. *J. Phys. Chem. B*, 115(1):34–40, 2010.

[214] Daniel Koller and Karl Lohner. The role of spontaneous lipid curvature in the interaction of interfacially active peptides with membranes. *Biochim. Biophys. Acta, Biomembr.*, 1838(9):2250–2259, 2014.

[215] Heidi Koldsø, David Shorthouse, Jean Hélie, and Mark SP Sansom. Lipid clustering correlates with membrane curvature as revealed by molecular simulations of complex lipid bilayers. *PLoS Comput Biol*, 10(10):e1003911, 2014.

[216] Dennis S. Bruhn, Michael A. Lomholt, and Himanshu Khandelia. Quantifying the relationship between curvature and electric potential in lipid bilayers. *J. Phys. Chem. B*, 120(21):4812–4817, 2016.

[217] Fatemeh Ahmadpoor and Pradeep Sharma. Flexoelectricity in two-dimensional crystalline and biological membranes. *Nanoscale*, 7(40):16555–16570, 2015.

[218] J J López Cascales and J García de la Torre. Effect of lithium and sodium ions on a charged membrane of dipalmitoylphosphatidylserine: a study by molecular dynamics simulation. *Biochim. Biophys. Acta*, 1330(2):145–56, 1997.

[219] John E. Straub and D. Thirumalai. Membrane-protein interactions are key to understanding amyloid formation. *J. Phys. Chem. Lett.*, 5(3):633–635, 2014.

[220] Thomas L. Williams and Louise C. Serpell. Membrane and surface interactions of Alzheimer's Aβ peptide - Insights into the mechanism of cytotoxicity. *FEBS J.*, 278(20):3905–3917, 2011.

[221] Sara M. Butterfield and Hilal A. Lashuel. Amyloidogenic protein-membrane interactions: Mechanistic insight from model systems. *Angew. Chemie - Int. Ed.*, 49(33):5628–5654, 2010.

[222] Ran Friedman. Aggregation of amyloids in a cellular context: modelling and experiment. *Biochem. J.*, 438(3):415–426, 2011.

[223] James A. Hebda and Andrew D. Miranker. The Interplay of Catalysis and Toxicity by Amyloid Intermediates on Lipid Bilayers: Insights from Type II Diabetes. *Annu. Rev. Biophys.*, 38(1):125–152, 2009.

[224] Kirsten Dahse, Megan Garvey, Michael Kovermann, Alexander Vogel, Jochen Balbach, Marcus Fändrich, and Alfred Fahr. DHPC Strongly Affects the Structure and Oligomerization Propensity of Alzheimer's Aβ(1-40) Peptide. *J. Mol. Biol.*, 403(4):643–659, 2010.

[225] Lars Tjernberg, Waltteri Hosia, Niklas Bark, Johan Thyberg, and Jan Johansson. Charge attraction and β propensity are necessary for amyloid fibril formation from tetrapeptides. *J. Biol. Chem.*, 277(45):43243–43246, 2002.

[226] Giovanni Bellesia and Joan Emma Shea. What determines the structure and stability of KFFE monomers, dimers, and protofibrils? *Biophys. J.*, 96(3):875–886, 2009.

[227] Yan Lu, Philippe Derreumaux, Zhi Guo, Normand Mousseau, and Guanghong Wei. Thermodynamics and dynamics of amyloid peptide oligomerization are sequence dependent. *Proteins Struct. Funct. Bioinforma.*, 75(4):954–963, 2009.

[228] Michele F M Sciacca, Jeffrey R. Brender, Dong Kuk Lee, and Ayyalusamy Ramamoorthy. Phosphatidylethanolamine enhances amyloid fiber-dependent membrane fragmentation. *Biochemistry*, 51(39):7676–7684, 2012.

[229] Evelyne Terzi, Guenter Hoelzemann, and Joachim Seelig. Alzheimer .beta.-Amyloid Peptide 25-35: Electrostatic Interactions with Phospholipid Membranes. *Biochemistry*, 33(23):7434–7441, 1994.

[230] Hongchun Li, Shuji Ye, Feng Wei, Sulan Ma, and Yi Luo. In situ molecular-level insights into the interfacial structure changes of membrane-associated prion protein fragment [118-135] investigated by sum frequency generation vibrational spectroscopy. *Langmuir*, 28(49):16979–16988, 2012.

[231] Ran Friedman, Riccardo Pellarin, and Amedeo Caflisch. Oluble protofibrils as metastable intermediates in simulations of amyloid fibril degradation induced by lipid vesicles. *J. Phys. Chem. Lett.*, 1(2):471–474, 2010.

[232] Ran Friedman, Riccardo Pellarin, and Amedeo Caflisch. Amyloid Aggregation on Lipid Bilayers and Its Impact on Membrane Permeability. *J. Mol. Biol.*, 387(2):407–415, 2009.

[233] Alex Morriss-Andrews and Joan Emma Shea. Kinetic pathways to peptide aggregation on surfaces: The effects of -sheet propensity and surface attraction. *J. Chem. Phys.*, 136(6), 2012.

[234] Riccardo Pellarin, Philipp Schuetz, Enrico Guarnera, and Amedeo Caflisch. Amyloid fibril polymorphism is under kinetic control. *J. Am. Chem. Soc.*, 132(42):14960–14970, 2010.

[235] Florentina Tofoleanu and Nicolae Viorel Buchete. Molecular interactions of Alzheimer's Aβ protofilaments with lipid membranes. *J. Mol. Biol.*, 421(4-5):572–586, 2012.

[236] Charles H Davis and Max L Berkowitz. Structure of the Amyloid-b(1-42)Monomer Absorbed To Model Phospholipid Bilayers: A Molecular Dynamics Study. *J. Phys. Chem. B*, 113(Md):14480–14486, 2009.

[237] Justin A. Lemkul and David R. Bevan. A comparative molecular dynamics analysis of the amyloid β-peptide in a lipid bilayer. *Arch. Biochem. Biophys.*, 470(1):54–63, 2008.

[238] Xiang Yu and Jie Zheng. Cholesterol promotes the interaction of alzheimer β-amyloid monomer with lipid bilayer. *J. Mol. Biol.*, 421(4-5):561–571, 2012.

[239] Julie Grouleff, Sheeba Jem Irudayam, Katrine K Skeby, and Birgit Schiøtt. The influence of cholesterol on membrane protein structure, function, and dynamics studied by molecular dynamics simulations. *Biochim. Biophys. Acta, Biomembr.*, 1848(9):1783–1795, 2015.

[240] M. Natalia Marangoni, Michael W. Martynowycz, Ivan Kuzmenko, David Braun, Paul E. Polak, Guy Weinberg, Israel Rubinstein, David Gidalevitz, and Douglas L. Feinstein. Membrane cholesterol modulates superwarfarin toxicity. *Biophys. J.*, 110(8):1777–1788, 2016.

[241] S. W. Altmann. Niemann-Pick C1 like 1 protein is critical for intestinal cholesterol absorption. *Science*, 303(5661):1201–1204, 2004.

[242] Sarah L Veatch and Sarah L Keller. Separation of liquid phases in giant vesicles of ternary mixtures of phospholipids and cholesterol. *Biophys. J.*, 85(5):3074–83, 2003.

[243] T Y Wang and J R Silvius. Cholesterol does not induce segregation of liquid-ordered domains in bilayers modeling the inner leaflet of the plasma membrane. *Biophys. J.*, 81(5):2762–2773, 2001.

[244] Richard M Epand, Alex D Bain, Brian G Sayer, Diana Bach, and Ellen Wachtel. Properties of mixtures of cholesterol with phosphatidylcholine or with phosphatidylserine studied by (13)C magic angle spinning nuclear magnetic resonance. *Biophys. J.*, 83(4):2053–2063, 2002.

[245] M. Rinaudo, M. Milas, and P. Le Dung. Characterization of chitosan. Influence of ionic strength and degree of acetylation on chain expansion. *Int. J. Biol. Macromol.*, 15(5):281–285, 1993.